Cryo electron microscopy study on gating mechanism of the lipid-modulated serotonin receptor

Dissertation

Zur Erlangung des Doktorgrades

der Naturwissenschaften

vorgelegt beim Fachbereich 14 - Biochemie, Chemie und Pharmazie

der Johann Wolfgang Goethe – Universität

in Frankfurt am Main

von

Yingyi Zhang

aus Shanghai, China

Frankfurt am Main 2020

(D 30)

Vom Fachbereich 14 - Biochemie, Chemie und Pharmazie der Johann Wolfgang Goethe – Universität als Dissertation angenommen.

Dekan: Prof. Dr. Clemens Glaubitz

1. Gutachter: Jun. Prof. Dr. Inga Hänelt

2. Gutachter: Dr. Misha Kudryashev

Datum der Disputation

Publications:

Y. Zhang*, P. M. Dijkman*, R. Zou, M. Zandl-lang, R. M. Sanchez, L. Eckhardt-Strelau, H. Köfeler, H. Vogel, S. Yuan, M. Kudryashev, Asymmetric opening of the homopentameric 5-HT_{3A} serotonin receptor in lipid bilayers, under peer-review

R. M. Sanchez*, Y. Zhang*, W. Chen, L. Dietrich, M. Kudryashev, Subnanometer-resolution structure determination *in situ* by a hybrid subtomogram averaging - single particle cryoEM – workflow, *Nature Communications*, accepted

P. M. Dijkman, T. Marzluf, Y. Zhang, H. Bujard, M. Kudryashev, Structure of the full-length merozoite surface protein 1 from *Plasmodium falciparum*, submitted

K. E. Leigh, P. P. Navarro, S. Scaramuzza, W. Chen, Y. Zhang, D. Castaño-Díez, M. Kudryashev, Subtomogram averaging from cryo-electron tomograms, *Methods in Cell Biology* 152, 217 (2019)

***** indicates equal authorship

Contents

Zusammenfassung

Auf dem Gebiet der Strukturbiologie versuchen Forscherinnen und Forscher durch die Nutzung mehrerer wissenschaftlicher Disziplinen und die Anwendung verschiedener biophysikalischer Techniken neuartige Strukturen von Biomolekülen unter physiologischen Bedingungen zu lösen und ihre Funktionsweise aus struktureller Sicht zu verstehen. Zu den Techniken, die häufig zur konformationellen Charakterisierung verwendet werden, gehören unter anderem Lichtmikroskopie (LM), Massenspektrometrie (MS), Kernspinresonanzspektroskopie (NMR), paramagnetische Elektronenresonanz (EPR), kryogene Elektronenmikroskopie (Kryo-EM) und Werkzeuge der theoretischen Biologie (Dobson, 2019; Schwede & Peitsch, 2008).

In den letzten zehn Jahren hat sich die Kryo-EM aufgrund von Verbesserungen sowohl bei der Hardware ("maschinenbasiert") als auch bei der Software ("algorithmisch") exponentiell entwickelt. Diese Verbesserungen haben die beste erreichbare Auflösung näher an die atomare Ebene gebracht. Dabei können "Lücken" überbrückt werden, die andere biophysikalischen Techniken nicht abdecken und ermöglicht es schwierigere biologische Fragen zu klären. Die beiden am weitesten verbreiteten Anwendungen der Kryo-EM sind die kryogene Einzelpartikelanalyse (Kryo-SPA) und die kryogene Elektronentomographie (Kryo-ET) in Kombination mit der Subtomogramm-Mittelung (STA). Im Allgemeinen konzentriert sich die Kryo-SPA auf die Lösung von Fragestellungen in einem gut isolierten System mit begrenzter Flexibilität und Heterogenität und liefert feinere Details durch die Lösung einer Rekonstruktion mit viel höherer Auflösung. Mittlerweile erreichen Kryo-ET und STA keine so hohe Auflösungen, ermöglichen aber eine

direkte Untersuchung *in situ*. Wir sind an der Methodenentwicklung interessiert und arbeiten momentan an der Kombination der Vorteile von Kryo-SPA und Kryo-ET in eine Methode. Daher wurde dieses Projekt so konzipiert und aufgebaut, dass die Kryo-EM zur Beantwortung biologischer Fragen eingesetzt werden kann, während gleichzeitig eine Entwicklung von Kryo-EM-Methoden möglich ist.

Der biologische Schwerpunkt unserer Forschung sind pentamerische ligandengesteuerte Ionenkanäle (pLGICs), insbesondere der Serotoninrezeptor Typ-3-Rezeptor ($5HT_3R$), der ebenfalls zur Familie der Cys-loop-Rezeptoren gehört. $5HT_3R$ spielt eine wichtige Rolle bei der schnellen synaptischen Signaltransduktion als Reaktion auf die Bindung von Agonisten und Antagonisten (Jackson & Yakel, 1995). Die Bindung von $5HT_3R$ an seinen nativen Liganden führt zur Öffnung des Kanals an der Transmembrandomäne, so dass Kationen hindurchtreten können. Dies führt zu einer Membrandepolarisation und zur Umwandlung des chemischen Signals in ein elektrisches Signal.

Zu Beginn dieses Projekts war von Hassaine und Kollegen nur eine hochauflösende röntgenkristallographische Struktur des geschlossenen Konformationszustandes des Detergens-solubilisierten Serotoninrezeptors ($5HT_3R$) berichtet worden (Hassaine et al., 2014). Es war unbekannt, wie die Ligandenbindung eine Kanalöffnung verursachen würde. Im Jahr 2018 berichteten Basak und Kollegen über die ersten Kryo-EM-Strukturen des detergenslöslich gemachten Serotoninrezeptors ($5HT_3R$) in seinen ligandenfreien (geschlossenen) und Serotonin-gebundenen Konformationszuständen (Basak, Gicheru, Rao, Sansom, & Chakrapani, 2018; Basak, Gicheru, Samanta, et al., 2018). Die Autoren bezeichneten die Serotonin-gebundene Konformation nicht als "offenen"

Zustand, da in den Molekulardynamik-Simulationen (MD) die freie Ionenpermeation in der Detergens-solubilisierten Serotonin-gebundenen Konformation nicht beobachtet wurde. Eine andere von Polovinkin und Kollegen veröffentlichte Serotonin-gebundene Kryo-EM Struktur von $5HT_3R$, die ebenfalls detergenslöslich vorlag, hatte die gleiche Schwierigkeit (Polovinkin et al., 2018). Eine vernünftige Annahme war, dass $5HT_3R$, der aus seiner nativen Membranumgebung extrahiert und in einem Detergens aufbewahrt wurde, folglich weniger auf Ligandenbindung reagierte. Daher war ein wichtiger Teil meines Projekts die Untersuchung des Einflusses von Lipiden auf die Öffnung und Schließung von $5HT_3R$, sowohl durch Kryo-SPA als auch durch Kryo-ET kombiniert mit STA (Kudryashev et al., 2016). Mit der erstgenannten Methode kann eine hohe Auflösung erreicht werden. Dabei wird das Protein in eine Lipid-Doppelschicht rekonstituiert, so dass das Protein in einem nahezu nativen Zustand untersucht werden kann, sowie eventuelle Lipidmodulation falls vorhanden. Die zweite Methode arbeitet nachweislich direkt mit nativen Vesikeln, die das Membranprotein enthalten. Allerdings ist die Auflösung der STA immer noch primär auf den Bereich von 1-2 Nanometer beschränkt. Diese Auflösung würde nicht ausreichen, um die biologische Frage zu beantworten.

Daher bestand meine Arbeit aus zwei spezifischen Zielen. Ein Ziel meiner Doktorarbeit war die konformationelle Untersuchung von $5HT_3R$ in seiner ligandengebundenen offenen Konformation mit Hilfe der Kryo-Elektronenmikroskopie (Kryo-SPA), um den Mechanismus des Öffnens und Schließens bei Ligandenaktivierung zu verstehen. Mein zweites Ziel bestand darin Kryo-SPA mit Kryo-ET und STA zu kombinieren, um die Auflösungsbegrenzung konventioneller Kryo-ET- und STA-Arbeitsabläufe voranzutreiben.

Am Ende konnten wir drei verschiedene Kryo-EM-Konformationen des membraneingebetteten $5HT_3R$ mittels Kryo-SPA auflösen. Dabei zeigten zwei Strukturen eine ruhende geschlossenen Form, eine C5-symmetrische und eine C1-asymmetrische, während die dritte Struktur eine Serotonin-gebundene offene Form darstellte. Diese drei Strukturen wiesen eine Reihe neuartiger Merkmale in Bezug auf den Übergang des Rezeptors in seinen ionenleitenden Zustand auf. Insbesondere zeigt der Serotonin-gebundene Rezeptor eine asymmetrische Öffnung, von der wir spekulieren, dass sie über einen intermediären asymmetrischen Apo-Zustand erfolgt. Ein detaillierter Vergleich der drei Konformationen und der zuvor publizierten detergenslöslich gemachten Konformationen wird in den Abschnitten Ergebnisse und Diskussion angesprochen, einschließlich der beobachteten wesentlichen strukturellen Unterschiede zwischen 5HT3R-Salipro im geschlossenen Ruhezustand und den früheren Detergens-stabilisierten Strukturen, die mit dem Effekt von stabilisierender Lipideinheiten zusammenhängen könnten - insbesondere eines M4-Helix angrenzenden Cholesterinmoleküls. Infolgedessen nimmt der Rezeptor eine dichter gepackte "gekoppelte" Konformation an, die sich bis zu einem Cluster hochkonservierter Reste an die Schnittstelle der extrazellulären Domäne (ECD) und Transmembran-Domäne (TMD) ausbreitet, welche wichtig für den Mechanismus des Öffnens und Schließens ist.

Diese Ergebnisse liefern den ersten strukturellen Nachweis für eine allosterische Modulation der Öffnung des $5HT_3R$-Kanals durch die Lipidmembranumgebung, eine Beobachtung, die sich auch auf andere pLGICs erstrecken kann. Was die Ursache der festgestellten Asymmetrie im homopentameren 5HT3R ist, bleibt eine unbeantwortete Frage. Zukünftige Studien, die sich an den von unseren Modellen gelieferten strukturellen Details orientieren, werden notwendig sein, um diesen Punkt

zu klären. Zusätzlich zu der Untersuchung von 5HT3R mit Hilfe von Kryo-SPA wird in dieser Arbeit Kryo-ET und STA verwendet, um 5HT3R in nativen Vesikeln zu untersuchen. Zusätzliche Arbeiten zur Entwicklung unserer Methoden, die sich auf die Kombination von Kryo-SPA- und STA-Techniken konzentrieren, sowie vorläufige Ergebnisse zum Tabakmosaikvirus werden ebenfalls detailliert diskutiert.

Die Dissertation beginnt mit einer Einführung in die Kryo-Elektronenmikroskopie (Kapitel 1, Abschnitt 1.1- 1.5), um deren Zweck, wichtige grundlegende Theorien, die Entwicklung moderner Techniken und aktuelle Standardverfahren zu beschreiben. Es folgt eine Einführung in unser biologisches Forschungsziel, die pLGICs und den Serotoninrezeptor Typ-3 (Kapitel 1, Abschnitt 1.6 - 1.7). Kapitel 2 beschreibt die angewandten experimentellen Materialien und Methoden. In Kapitel 3 werden die wichtigsten Ergebnisse meiner Doktorarbeit, einschließlich unserer Erkenntnisse über den Öfnungs- und Schließmechnismus des 5HT3R-Kanals und seine kritische Lipidmodulation, ausführlich beschrieben (Abschnitt 3.1- 3.5). Die Abschnitte 3.6 - 3.7 behandeln die Arbeit an 5HT3R-Mikrovesikeln unter Verwendung von Kryo-ET sowie die Entwicklung einer kombinierten STA-SPA-Methode und ihre Anwendung auf eine Modellprobe, tobacco mosaic virus (TMV). Auf diese Ergebnisse folgt eine Diskussion ihrer Bedeutung im Feldkontext und ein hypothetisches Modell für ein lipidmoduliertes Öffnen und Schließen des Kanals (Kapitel 4). Nach einer kurzen Zusammenfassung (Kapitel 5) werden schließlich Perspektiven und zukünftige Arbeiten beschrieben (Kapitel 6).

Zusammenfassend lässt sich sagen, dass im Laufe dieses Projekts und meiner Doktorarbeit wichtige Erkenntnisse gewonnen und praktische

Fähigkeiten in der Kryo-EM und ihrer Anwendung auf Biomoleküle entwickelt wurden, um die Beziehung zwischen struktureller Konformation und Funktion zu untersuchen. Mit dieser Technik konnten wir bisher nicht berichtete asymmetrische Anordnungen der Untereinheiten des homopentameren 5HT3R um die Porenachse aufdecken. Der asymmetrische offene Zustand wird durch Phospholipide stabilisiert, die an der Grenzfläche zwischen den Untereinheiten an einer Stelle eingefügt werden, die für die Bindung allosterischer pLGIC-Modulatoren gut dokumentiert sind (Taly, Hénin, Changeux, & Cecchini, 2014). Diese Ergebnisse geben nicht nur strukturelle Unterstützung für eine große Menge an funktionellen Daten über die Auswirkungen von Lipiden auf die Funktion dieser Rezeptorfamilie, sondern bieten auch eine strukturelle Anleitung für zukünftige Studien auf diesem Gebiet. Inzwischen haben die kombinierten SPA-STA-Methoden, die im Laufe dieser Arbeit entwickelt wurden, das Potenzial zur Auflösung tomographiebasierter Strukturen mit höherer Auflösung beizutragen. Zukünftige Forscher könnten davon profitieren, wenn diese *in situ*-basierte Strukturstudien durchführen wollen.

Summary

In the field of structural biology, by leveraging multiple scientific disciplines and applying different biophysical techniques, researchers seek to solve novel structures of biomolecules under physiological conditions, and to understand their functionality from a structural point-of-view. Techniques frequently used for conformational characterization include, but are not limited to, light microscopy (LM), mass spectrometry (MS), nuclear magnetic resonance spectroscopy (NMR), electron paramagnetic resonance (EPR), cryogenic electron microscopy (cryo-EM), and computational theoretical biology tools (Dobson, 2019; Schwede and Peitsch, 2008).

Over the last decade, cryo-EM has developed exponentially due to improvements in both hardware ("machine"-based) and software ("algorithm"-based). These improvements have pushed the best achievable resolutions closer to atomic level, bridging "gaps" not covered by other biophysical techniques, and allowing more difficult biological questions to be addressed. The two most widely-used applications of cryo-EM are cryogenic single particle analysis (cryo-SPA) and cryogenic electron tomography (cryo-ET) combined with sub-tomogram averaging (STA). In general, cryo-SPA focuses on solving structures in a well-isolated system with limited flexibility and heterogeneity, providing finer details up to a few angstroms in resolution and allowing observation at protein-protein and protein-ligand interactions. It also has a particular major impact on understanding structures and functions of membrane proteins in their wild-type forms in solution. Meanwhile, cryo-ET and STA achieve lower resolution, but allow structural analysis directly *in situ* at

molecular level. We are interested in method development and work on combining the benefits of both cryo-SPA and cryo-ET together into a single method is on-going. Thus, this project was designed and constructed to apply cryo-EM to answer biological questions, while allowing simultaneous cryo-EM method development.

In my PhD study, the biological research targeting is the gating mechanism of pentameric ligand-gated ion channels (pLGICs), specifically the serotonin receptor type-3 receptor ($5HT_3R$), which also belongs to the Cys-loop receptor family. $5HT_3R$ plays an important role in fast synaptic signal transduction in response to agonist and antagonist binding (Jackson and Yakel, 1995). Binding to its native ligand results in opening of the channel at the transmembrane domain, allowing cations to pass through, resulting in membrane depolarization and conversion of the chemical signal into an electrical one.

At the beginning of this project, only one high-resolution X-ray crystallography structure of the closed conformational state of detergent-solubilized serotonin receptor ($5HT_3R$) had been reported by Hassaine and colleagues (Hassaine et al., 2014). It was unknown how the binding of its native ligand, serotonin (neurotransmitter), would cause channel opening. In 2018, Basak and colleagues firstly reported the cryo-EM structures of detergent-solubilized serotonin receptor ($5HT_3R$) in its ligand-free (closed) and serotonin-bound conformational states (Basak et al., 2018a; Basak et al., 2018b). The authors did not designate the serotonin-bound conformation as an “open” state because free ion permeation wasn’t observed in the detergent-solubilized serotonin-bound conformation in molecular dynamic (MD) simulations. Another published serotonin-bound cryo-EM $5HT_3R$ structure, also detergent-solubilized, by

Polovinkin and colleagues had the same difficulty (Polovinkin et al., 2018). A reasonable assumption was that $5HT_3R$ extracted from its native membrane environment and kept in detergent was consequently less responsive to ligand binding. Therefore an important part of my project was to study lipid-modulation of $5HT_3R$ gating, by both cryo-SPA and cryo-ET combined with STA (Kudryashev et al., 2016). The former method can achieve high resolution, and the protein would be reconstituted into lipid bilayers, so that lipid-modulation, if any, could be addressed by studying the protein in a near-native state. The latter method has been demonstrated to work directly with native vesicles containing the membrane protein. However, the resolution of STA is still primarily limited to the 1-2 nanometer range, and such resolutions would not be sufficient to answer the biological questions.

Therefore, my work consisted of two specific aims. One aim of my PhD study was focused on conformational investigation of $5HT_3R$ in its ligand-bound open conformation, using cryo-electron microscopy (cryo-SPA), in order to understand the gating mechanism upon ligand activation. My second aim became to combine SPA with cryo-ET and STA to push the resolution limitation of conventional cryo-ET and STA workflows with an eventual aim to apply it to $5HT_3R$ study.

As a result, we were able to resolve three different cryo-EM conformations of membrane-embedded $5HT_3R$ using cryo-SPA, two structures in resting closed forms, one C5-symmetric and one C1-asymmetric, and one serotonin-bound open form. These three structures presented a number of novel features related to the transition of the receptor to its ion-conductive state. Specifically, the serotonin-bound receptor shows asymmetric opening, which we speculate to occur via an intermediate

asymmetric Apo state. A detailed comparison of the three conformations and the previously published detergent-solubilized conformations are addressed in the results and discussion sections, including that substantial structural differences observed between $5HT_3R$-Salipro in the resting closed state and the previous detergent-stabilized structures could be related to the effect of stabilising lipid moieties – in particular a cholesterol molecule adjacent to the M4 helix. As a result, the receptor adopts a more tightly packed 'coupled' conformation that extends to a cluster of highly conserved residues at the extracellular-domain (ECD)-transmembrane-domain (TMD) interface important for gating.

These results provide the first structural evidence for allosteric modulation of $5HT_3R$ gating by the lipid membrane environment, an observation that may extend to other pLGICs. What causes the detected asymmetry in the homopentameric $5HT_3R$ remains an unanswered question. Future studies guided by the structural detail provided by our models will be necessary to address this point. In addition to the cryo-SPA work, application of cryo-ET and STA to the study of $5HT_3R$ in native vesicles is described in this thesis. Additional work on our methods development, focused on combining SPA and STA techniques, along with preliminary results on tobacco mosaic virus (TMV) are also detailed and discussed.

The thesis begins with an introduction to cryo-electron microscopy (Chapter 1, Section 1.1– 1.5), in order to describe its purpose, important fundamental theories, modern technique development, and current standard practices. This is followed by an introduction to our biological research target, pLGICs and serotonin receptor type-3 (Chapter 1, Section 1.6 – 1.7). In Chapter 2, the experimental materials and methods applied are described. In Chapter 3, the main results of my PhD work, including

our findings on the gating mechanism of $5HT_3R$ and its critical lipid-modulation, are described in detail (Section 3.1– 3.5). Sections 3.6 – 3.7, cover the work on $5HT_3R$ micro-vesicles using cryo-ET, and the development of a combined STA-SPA method and its application to a model sample, TMV. These results are followed by a discussion of their meaning in the context of the field and a hypothetical model for lipid-modulated channel gating (Chapter 4). Finally, after a brief conclusion (Chapter 5), perspectives and future work are described (Chapter 6).

In summary, during the course of this project and my PhD work, important knowledge was established, and practical skills were developed in cryo-EM and its application to biomolecules to address the relationship between structural conformation and function. We gained critical insights into the activation of $5HT_3R$ and its regulation by native lipids. We revealed previously unreported asymmetric arrangements of the subunits of the homopentameric $5HT_3R$ around the pore axis. The asymmetric open state is stabilized by phospholipids inserted at the interface between subunits, at a site well-documented for the binding of allosteric pLGIC modulators (Taly et al., 2014). These results not only give structural support to a large body of functional data on the effects of lipids on the function of this receptor family, but also provide structural guidance for future studies in this field. Furthermore, the SPA-STA combined methods developed during the course of this work have the potential to help resolve higher resolution tomography-based structures, including the structure of $5HT_3R$ in native-derived vesicles. This is a general method which would benefit researchers seeking to do *in-situ*-based structural studies.

Summary

List of Figures

List of Tables

Abbreviations

1D: one dimensional

2D: two dimensional

3D: three dimensional

5-HT: 5-hydroxytryptamine; serotonin

$5HT_{3A}R$: type-3A serotonin receptor

Ach: acetylcholine

AWI: air-water interface

BPL: brain polar lipid

BS electron: backscattered secondary electron

C_c: chromatic abbreviation

C_s: spherical abbreviation

CCD: charge coupled devices

CMOS: complementary metal oxide semiconductors

Cryo-EM: cryogenic-electron microscopy

Cryo-ET: cryogenic-electron tomography

Cryo-FIB: cryogenic-focused-ion-beam milling

CTF: contrast transfer function

CV: column volumes

DCE: detector conversion efficiency

DED: direct electron detector

DQE: detection quantum efficiency

ECD: extracellular domain

EDXS: energy-dispersive x-ray spectrometry

EELS: electron energy loss spectrometry

ELIC: bacterial Erwinia chrysanthemi pentameric ligand-gated ion channel

EM: electron microscopy

EMDB: electron microscopy data bank

EPR: electron paramagnetic resonance

FEG: field-emission gun

FPS: frame per second (fps)

FSC: Fourier shell correlation

GABA: γ-aminobutyric/ gamma-aminobutyric acid

GABARs: γ-aminobutyric/ gamma-aminobutyric acid receptors

GIS: gas injection system

GluCl: glutamate-gated chloride channel

GlyRs: glycine receptors

GLIC: bacterial Gloeobacter violaceus pentameric ligand-gated ion channel

GPCR: G-protein coupled receptor

ICD: intracellular domain

IMAC: immobilized metal affinity chromatography

LBP: ligand binding pocket

LM: light microscopy

MAPS: monolithic active pixel sensor

MD: molecular dynamic

MS: mass spectrometry

MST: microscale thermophoresis

MTBE: methyl-tert-butyl ether

MTF: modulation transfer function

MW: molecular weight

MWCO: MW cut-off

nAhCRs: nicotinic acetylcholine receptors

NMR: nuclear magnetic resonance spectroscopy

NS: negative staining

PDB: protein data bank

pLGICs: pentameric ligand-gated ion channels

RMSD: root mean square deviation

RMSF: root mean square fluctuation

Salipro: saposin lipoprotein

SEM: scanning electron microscopy

SSNR: spectral signal-to-noise ratio

STA: subtomogram average

TEM: transmission electron microscopy

TM1: transmembrane helix 1

TMD: transmembrane domain

TMV: tobacco mosaic virus

UA: uranyl acetate

UF: uranyl formate

VMD: molecular dynamics visualization program

XRC: x-ray crystallography

Z: atomic weight

Chapter 1 Introduction

“An experiment is a question which science poses to Nature, and a measurement is the recording of Nature's answer.”

- Max Planck (Planck, 1949)

"If these things were to be realised it hardly needs to be emphasised that the advances in the field of research into the causes of disease would be of immediate practical interest to the doctor. It would deeply affect real problems concerned to a large extent with diseases of growing clinical significance and thus of great importance for public health.

Should the possibilities of microscopical resolution exceed the assumed values by a factor of a hundred, the scientific consequences would be incalculable. What seems attainable now, I consider to be so important, and success seems to me so close, that I am ready and willing to advise on medical research work and to collaborate by making available the resources of my Institute".

- Ernst Ruska (Ruska, 1987)

In the field of medical and biological science, electron microscopy (EM) nowadays plays a great role in answering questions like functionally-relevant detailed architecture of cells and organelles (Kudryashev, 2018; Lučič et al., 2013), the fine structure of macromolecules from large to tiny (from several thousands to a couple of tens of kDa) (Eibauer et al., 2015; Fan et al., 2019; Flores et al., 2020; Galej et al., 2016; Huang et al., 2020; Zhang et al., 2018). The highest resolution structure resolved by cryo-EM currently is up to 1.62 Å of mouse heavy-chain apoferritin (Danev et al., 2019), which is at a near-atomic level and provides finer information than that of the light microscopy (LM). Also, its adaption on various specimen dimensions and complexities beyond the range that X-ray crystallography (XRC) and Nuclear Magnetic Resonance spectroscopy (NMR) could achieve (**Figure 1.1**). Moreover, EM is powerful and promising in revealing the biological dynamic behaviors *in vivo*, plus the transition among several conformational and functional states of molecular machines (Eibauer et al., 2012; Vafabakhsh et al., 2015). The Nobel Prize in Chemistry 2017 awarded to Jacques Dubochet, Joachim Frank and Richard Henderson “*for developing cryo-electron*

microscopy for the high-resolution structure determination of biomolecules in solution" is a millstone, likely enough to prove that cryo-EM today is a well-established tool for structural characterization of biological molecules in pursuing the knowledge on function-structure relationship. It has been 87 years after the first electron microscope was developed in 1933 by Ernst Ruska, and 31 years most-recently since he won the Nobel Prize in Physics in 1986 for his work in electron optics (Hawkes, 1990). Scientific researches in this filed get "incalculable" benefits with the developing of electron microscopy.

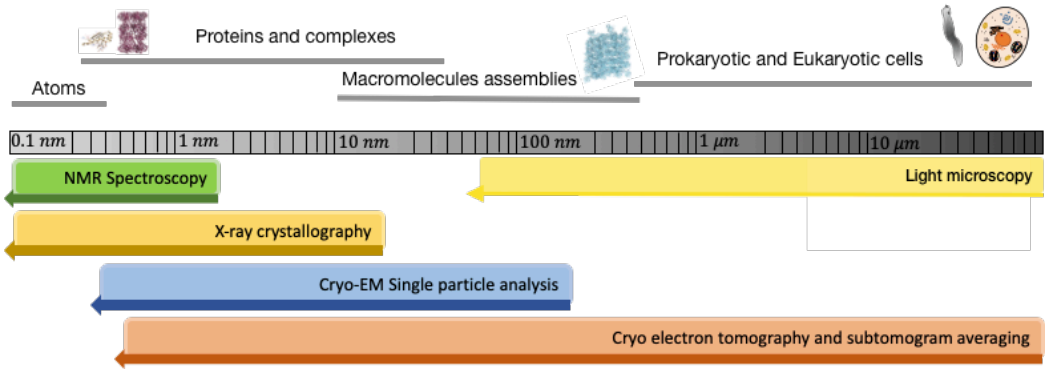

Figure 1.1 Scales and structural characterization techniques in molecular and cell biology. The scale ranges covered by different imaging methods in molecular biology from atoms to cells. This figure was reproduced from (Leigh et al., 2019). Copy right © 2019 Elsevier Inc.

EM application in medical and biological researches, as a big branch on the EM "family tree", shares the general "root" with other "branches", that is the theoretical basis of transmission electron microscopy. To get better understanding application of cryo-EM to biomolecular structural studies, this chapter starts with basic principles of transmission electron microscopy (TEM) in Section 1.1, then followed with the main introduction on its application in medical and biological scientific studies (Section 1.2 to 1.5), normally referring cryogenic electron microscopy as the cryo-EM studies. After that, in Section 1.6 and 1.7, my focus of study is introduced - pentameric ligand gated ion channels (pLGICs) and serotonin receptors which are important neurotransmitter receptors playing central role of synaptic signaling.

1.1 Transmission electron microscopy: Basics

This section is an introduction within several specific aspects that are fundamental of transmission electron microscopy and of great help to understand its advantages in principle.

1.1.1 The wavelength of electron

In a transmission electron microscope (TEM) (**Figure 1.2** A), a nearly parallel beam of electrons is extracted from a fine tip of a metallic crystal via i.e. thermal emission, and is accelerated with applied high voltage (**Figure 1.2** B). Then electrons travel through a series of magnifying electromagnetic coils equivalent to the optical lenses, incident on a thin specimen (**Figure 1.2** C). After that, the electrons get transmitted, further magnified by projection lenses and finally arrive at the detector (**Figure 1.2** D), and are recorded on a sensor and read-out. The image of a specimen recorded in this process contains high resolution information potentially up to atomic scale.

One of the fundamental reasons for the high resolution of transmission electron-microscopy is that the electrons as probes have extremely short wavelength when they are accelerated with high voltage acceleration.

At accelerating voltage larger than 100 keV, the relationship between the electron wavelength (λ) and the accelerating voltage (V) of the electron microscope is (Williams and Carter, 2009d),

$$\lambda = \frac{h}{\sqrt{2m_0 eV\left(1 + \frac{eV}{2m_0 c^2}\right)}}$$

where h is Planck's constant, m_0 is the resting mass of an electron. Given the equation above, the calculated wavelength of the electron beam operated in the modern commercial TEMs are listed in **Table 1.1**.

Table 1.1 Electron beam wavelength as a function of accelerating voltage.

Accelerating Voltage (kV)	Wavelength (Å)
120	0.0335
200	0.0251
300	0.0197

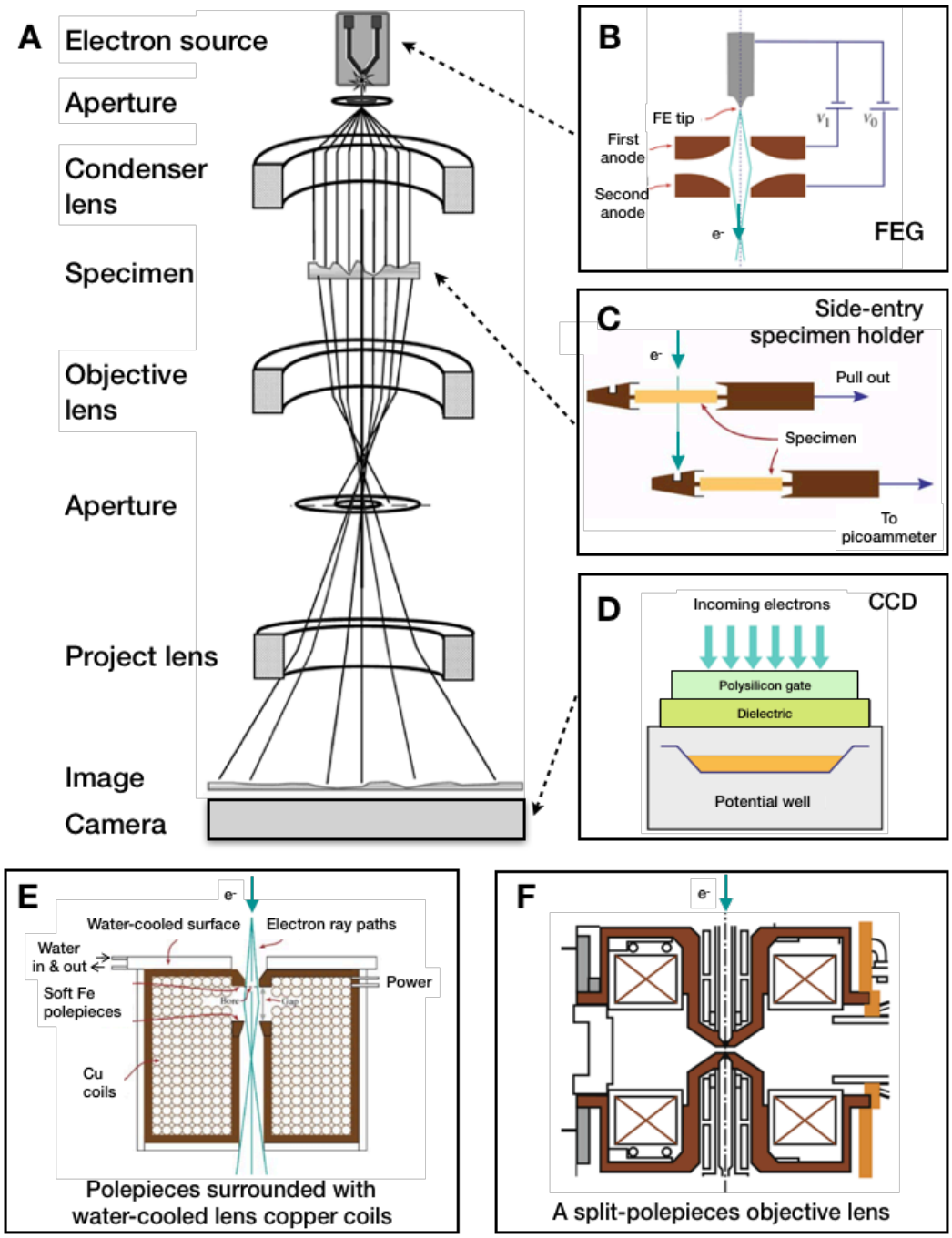

Figure 1.2 Schematic drawing of the TEM and part of its components. (**A**) Simplified schematic representation of an electron microscope. (**B**) FEG. (**C**) Side-entry specimen holder. (**D**) CCD camera. (**E**) magnetic lens with polepieces in lens coils. (**F**) objective lens with split polepieces. This figure was reproduced from (Orlova and Saibil, 2011; Williams and Carter, 2009d) with permission.

1.1.2 Elastic and inelastic electron scattering

Another fundamental reason for TEM can preserve higher resolution information of its specimen is that electrons having electrostatic interactions with the atoms of the specimen when they traveling through. These electrostatic interactions cause the scattering of the electrons, makes the specimen “visible” to the detector, which is the basis to understand the formation of TEM images, before any attempt of operating, processing or optimizing in practice.

The electron scattering can be grouped as elastic and inelastic scattering referring to a scattering without loss of electron energy, or with a certain amount of energy loss that normally detectable. In a simplified case, elastic scattering could be considered as coherent and inelastic scattering as incoherent (Williams and Carter, 2009a).

Elastic scattered electrons are the major source of contrast in TEM images. In the mostly simplified situation, only one scattering occurs during electron transmitted through the specimen, they are called single scattering. If the electron gets scattered more than one time, it is getting difficult to predict the events during scattering, as the electron is carrying more complicated information to recover, or just contributes to noise. Thus, the thinner the specimen, it is more likely to be single scattered or unscattered. Assuming the electron is scattered by an isolated atom, two types of elastic scattering can occur: either elastically scattered by the negatively charged electric cloud with a small angle ($< 10^{o}$), or by the attraction towards a positive nucleus. In the latter one, the angle is much larger that can approach 180^{o}, which is a complete backscattering electron (**Figure 1.3** A).

The energy loss during inelastic scattering is converted into different forms through X-ray emission, secondary electron emission and others, could be heat as well (**Figure 1.3** B). In the field of materials engineering, these spectrums are fundamental and useful information could be detected and analyzed for specimen chemical characterization, like EDXS. While in biological cryo-EM imaging, they are rather considered as better-to-avoid, because inelastic scattered electrons are one principle source of noise in TEM images, and are normally the major reason causing beam-induced damage to the specimen.

The electron scattering could occur whenever the electron has interacted with the elements it passes through. These elements include the contamination presenting in a vacuum chamber, the specimen itself apparently, also the detector (like scintillator or other types of sensors). And the final information

recorded on the TEM images will be a combination of all the electron scattering events. Thus, we have good reasons to keep designing better hardware (like vacuum system for cleaner chamber, detector devices generating less noises), and sample preparation solutions for thinner specimen.

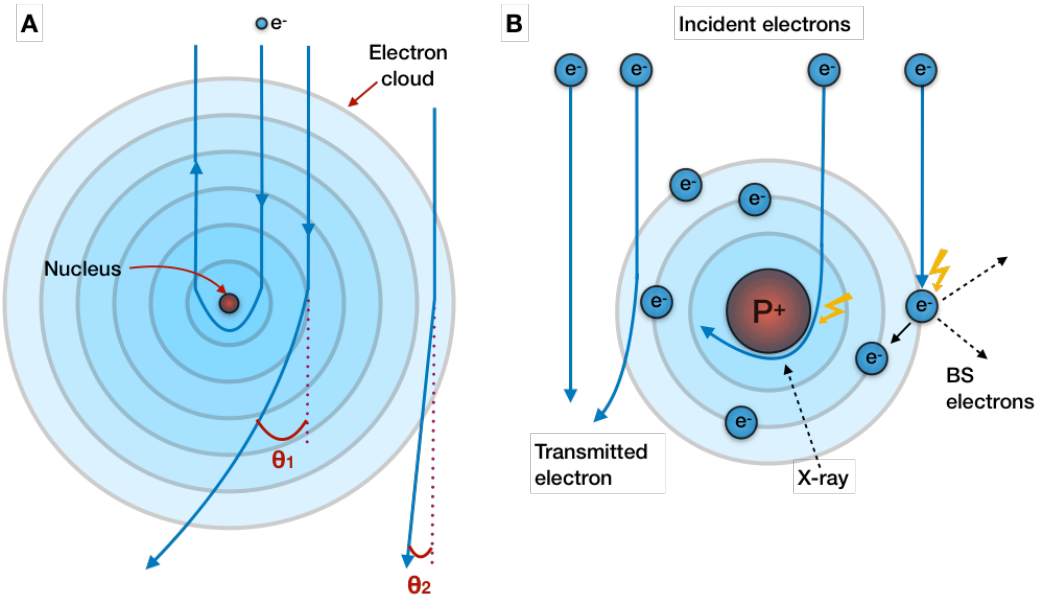

Figure 1.3 Electron scattering. (**A**) Schematic elastic electron scattering by an isolated atom. Coulombic attraction by the nucleus causes higher-angle scattering (θ_1, up to 180°). Coulombic interaction with the electron cloud results in low-angle scattering (θ_2). The potential within the electron cloud is always positive (Williams and Carter, 2009a). (**B**) Schematic of elastic and inelastic scattering in thin specimen. Electron energy loss during inelastic electron scattering contributes to the generation of X-ray, backscattered secondary (BS) electron, heat and so on (Orlova and Saibil, 2011).

1.1.3 Electromagnetic lens aberrations

In TEM, magnetic lenses are used for focusing and magnifying of the electron beam because they are not susceptible to high-voltage breakdown. In general, a magnetic lens is composed of a soft-iron polepieces sitting in middle of the lens (**Figure 1.2** E), surrounded by copper coils through which the current runs to magnetize the polepieces. The strength of magnifying is corresponding to the strength of the magnetic field, which could be adjusted through adjusting the lens's current. Objective lens is a very strong lens in a TEM, which is composed

of different configurations to the normal magnetic lenses, having its upper and lower polepieces with separate coils (called “split-polepieces” lens, **Figure 1.2** F) and spaces in between are left for manipulation of the inserted specimen and apertures or phase plate (Williams and Carter, 2009c).

In contrast to glass lenses, magnetic lenses are far from perfect. These lenses defects, spherical and chromatic aberrations (Budinger and Glaeser, 1976), curvature of the field, astigmatism and coma (F. Zemlin, 1978), limit the resolution of the microscope, but contribute to better depth of focus and depth of field. This section we will introduce very briefly only these ones: spherical aberration, chromatic aberration and astigmatic aberration, that limiting the performance of microscope substantially.

Spherical aberration (C_S), constant of a lens manufactured, comes from that some of the larger off-axis electrons scattered by the imaging object are not being converged back onto the same point on its Gaussian imaging plane, where a perfect lens does for comparison (**Figure 1.4** A). Thus, a point object P is imaged on the Gaussian imaging plane not as a point, but as a region (**Figure 1.4** B), with central intensity higher than the outer, which limit the resolution of most TEMs. It could be corrected with an additional magnetic lens as a compensator that diverge the large off-axis electrons first before it could be converged back onto the same point on its Gaussian imaging plan.

Chromatic aberration (C_C), represents how monochromatic the electron beam is referring to its energy spread. As we discussed in the previous sections, the energy of the electrons beam in TEM is related to the brightness and coherency of the electron source (differs a lot from thermionic tip to field-emission gun, or FEG), the stableness of its accelerating voltage, and the energy loss during inelastic electron scattering. The diverging electron beam with different energy would apparently convergent at different focal plane (**Figure 1.4** C) by magnetic lenses, according to Lorentz force. For a 300 kV TEM with field-emission gun (FEG), the chromatic aberration is rarely affecting the image resolution (Williams and Carter, 2009c).

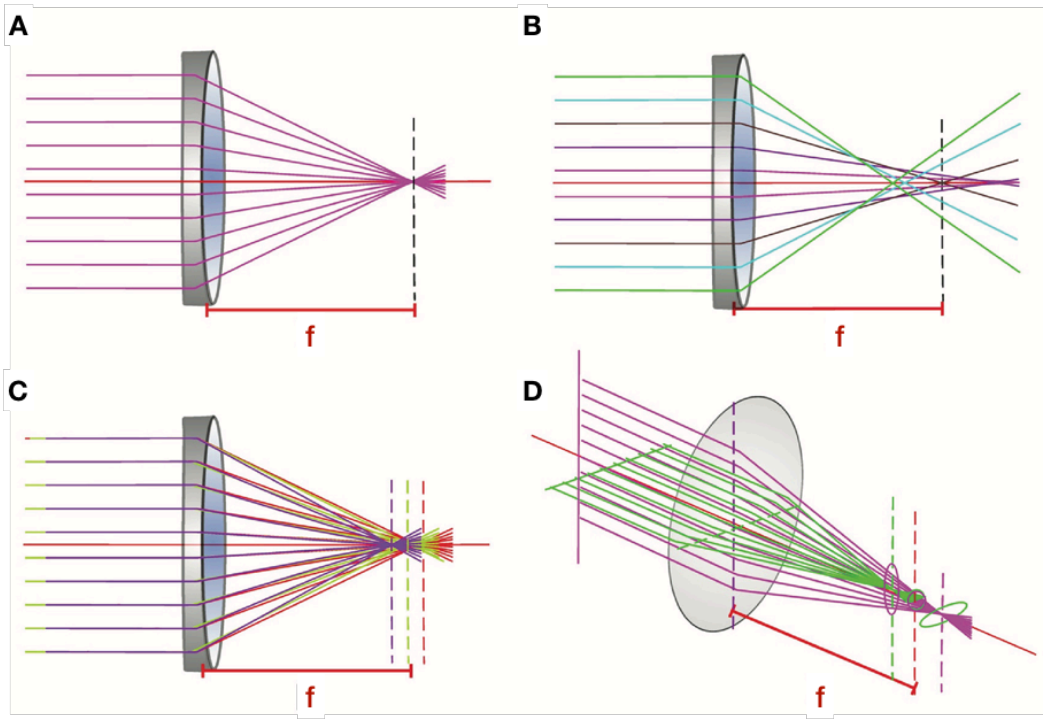

Figure 1.4 Ray diagrams of lens aberrations. (**A**) Perfect lens without aberration. (**B**) Spherical aberration. (**C**) chromatic aberration. (**D**) astigmatic aberration. Red f is the length of focus. This figure was reproduced from (Orlova and Saibil, 2011) with permission. Copyright © 2011 American Chemical Society.

Astigmatic aberration, or astigmatism, is observed when the electron travels through a non-uniform magnetic field created by the lens coils. The manufactured polepieces is made of soft-iron that has microstructural heterogeneities and hardly be exact symmetrical aligned down the bore. In consequences, the magnetic field strength would variate spatially, which results in the misaligning of electrons down through their expected focal point in plane (**Figure 1.4** D). Meanwhile, introducing a not well-centered aperture would also distribute the field with a non-uniform off-axis manner. These non-uniform filed could be easily compensated using stigmators.

In summary, there three aberrations contribute most to the limiting of image resolution, and are the most frequently encountered concepts during EM data collection and processing. Its influences on image formation will be introduced in Section 1.3.

1.2 Specimen preparation of electron microscopy on biomolecular structural studies

The on-developing state-of-art EM microscopy has its applications pretty diverging but interactive. Depending on the research of interest, applications are well designed in purpose of solving specific questions, from readily to more difficult cases, in accordance but not limited to the dimension, heterogeneity, integrity of the specimens, and the targeting resolution, the complex-complex or complex-membrane interactions and so on.

The most well-established and applied electron microscopy in structural biology studies are cryogenic- single particle analysis (cryo-SPA) and electron tomography (cryo-ET) with subtomogram averaging (STA). Cryo-SPA nowadays is very powerful, yields near-atomic resolution structures of biomolecules (Danev et al., 2019). In spite of the benefits of recent advances (Kuhlbrandt, 2014) in EM specimen preparation (Fan et al., 2019), data acquisition (Biyani et al., 2017), hardware development like phase plate (Khoshouei et al., 2016; Kunpeng Li et al., 2019) and director detector (Bammes et al., 2012; Cao et al., 2013) and advanced image processing methods (Li et al., 2013b; Zhao et al., 2015; Zivanov et al., 2018; Zivanov et al., 2019), cryo-SPA still requires the biomolecules in a well-isolated form, which is achieved by extracting them from their native environment through protein purification, which makes it impossible to understand the biological interaction of the biomolecule within its native environment. While, in contrast, cryo-ET with subtomogram averaging (STA), also benefited of recent advances in hardware (Khoshouei et al., 2017) and software (Bharat and Scheres, 2016; Navarro et al., 2018), breaks the limitation as its ability to determine structure in situ (Baker et al., 2017; Leigh et al., 2019; von Appen et al., 2015). Moreover, cryo-ET is capable to visualize much wider range of biology details from protein complexes up to cells in their biological environment (Irobalieva et al., 2016). In both cases of cryo-SPA and ET, samples introduced into vacuum chamber of an electron microscope need to be treated. In this section, the most-common applied EM specimen preparation methods are introduced.

1.2.1 Negative staining

The most commonly-used and simplest sample preparation method for the start of an EM structural study is negative staining for isolated macromolecular complexes. It is fast, easy to operate and provides information about the size, shape, integrity, homogeneity and some of other features of the analyzed sample. The staining solution normally contains heavy metal elements, like uranyl acetate (UA), uranyl formate (UF), ammonium molybdate, and methylamine tungstate and others. Staining solutions have different properties like pH value, density, grain size and contrast (Brillault and Landsberg, 2020). Although UA and UF are currently most-commonly used, the other staining might be particularly under demand for some proteins (Harris and Scheffler, 2002).

Preparation of a negative staining grid is as described following (**Figure 1.5** A). Firstly, the continuous carbon coated grid is treated with glow discharger, or plasma cleaner. The ionized gas is capable to conduct electricity and makes the carbon surface on the grid hydrophilic. Right after glow discharging, one droplet of the sample solution is applied on top of the treated side. Incubation of sample on the grid and then blotting the sample away on the side of the grid. Secondly, applying the staining droplet onto the grid and blotting dry with filter paper. Repeating two to three times with no incubation needed. Thirdly, applying the last staining droplet and leaving it staining for around 30 seconds on the grid before blotting. Note, depends on the final contrast of the staining, this incubation time is user-justified, based on the cumulated handling experience of particular sample in certain concentration. After blotting and air dry, the grid is ready for illuminating under TEM.

With negative staining, the electrons that interacted with heavy metal elements are strongly scattered off the optical axis. These electrons would not arrive at the imaging plane, that generates higher amplitude contrast in the image. Thus, the isolated protein could be well seen as “brighter” particles with the amplitude contrast created from excluded staining grains around the protein (**Figure 1.5** B).

Negative staining is widely applicable unless the sample is particularly sensitive to dehydration or buffer condition like pH value. Beside, as the dehydrating might introduce a certain extend of distortion and damage to the sample in general, cryo-plunge freezing is commonly the step next for cryo-SPA or some cryo-ET specimen preparation.

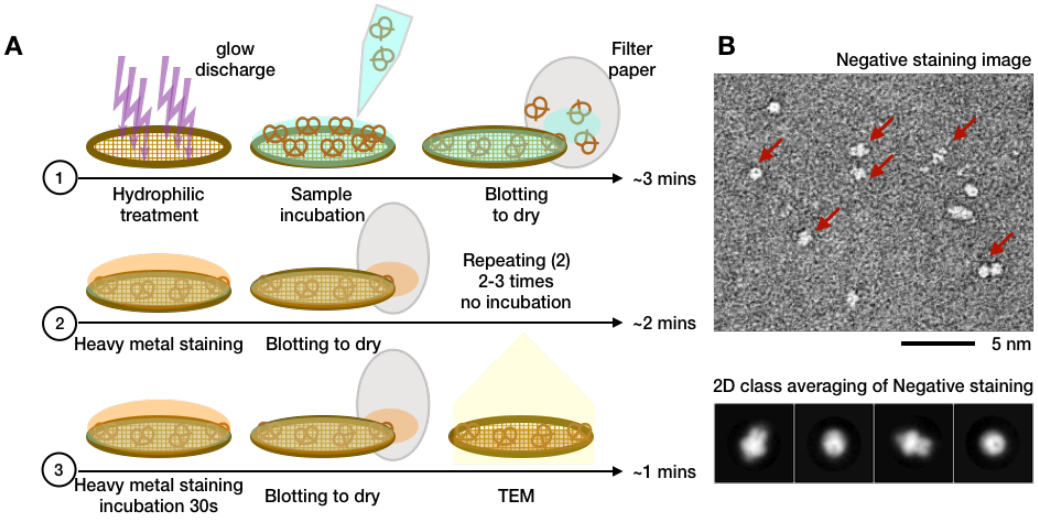

Figure 1.5 Negative staining. (**A**) The negative staining protocol of isolated proteins. (**B**) Negative staining images of serotonin receptor in lipid-nanodisc (top, red arrows indicate some of the serotonin receptors), and 2D class averaging presents the different orientations that receptor adapted on grid (bottom).

1.2.2 Cryo specimen preparation by plunge freezing

The EM specimen required for cryo-EM imaging, including cryo-SPA and some application of cryo-ET, has to be thin enough to allow electron transmission, ideally within a hundreds of nanometers thickness. To prepare such EM specimen with suitable thickness, typically less than 200 nm for cryo-SPA, plunge freezing of sample into liquid cryogen is applied. Since complete vitrification of thin water film is demonstrated in early 1980s (Brüggeller and Mayer, 1980), it is the most well-developed and widely-used method nowadays for aqueous biological samples like isolated macromolecules, viruses, thin bacteria cells, or the periphery of some larger cells. The fast cooling rate of liquid cryogen allows the formation of a continuous vitreous ice film on a thin substrate, which allows electron beam gets transmitted (Dubochet et al., 1988).

Plunge freezing is becoming very handy with the development of modern commercial devices, like Gatan Cryoplunge 3 GentleBlot System, Thermo Fisher Scientific Vitrobot, Leica EM GP. A brief description of the preparation steps is following (**Figure 1.6**). Firstly, the EM grids are pretreated to make sure its surfaces are clean and hydrophilic (**Figure 1.6** A). To get a hydrophilic surface or to improve the sample distribution on top of the grid, glow discharger or plasma

cleaner is the basic requirement, and chemical treatment is involved in some cases (Meyerson et al., 2014). Others approaches, like pre-coating with another substrate like graphene or graphene oxide films are developed (Palovcak et al., 2018; Wang et al., 2019), in order to solve some potential problems during plunge-freezing, such as poor particle orientation distribution (Drulyte et al., 2018), and biological sample damaging at the air-water interface (AWI) (D'Imprima et al., 2019; Noble et al., 2018). Secondly, around ~3uL biological sample suspension/solution with a desired concentration (**Table 1.2**) is applied onto of a pretreated EM grid (3mm in diameter). In this step, detergent could also be helpful to add in order to protect sample from AWI. Afterwards, the grid carrying sample is proceeded with filter-paper blotting inside the devices, and plunge freezing into cryogen which fixing the sample by forming a thin ice film onto the EM grid (**Figure 1.6** B). Time takes less than a minute from sample applied onto grid to become vitrified. Then, the EM specimen could be stored and ready for screening in microscopes. Proteins in cryo-EM images look darker than the ice they embedded in, and are expected to present with randomly different orientations (**Figure 1.6** C).

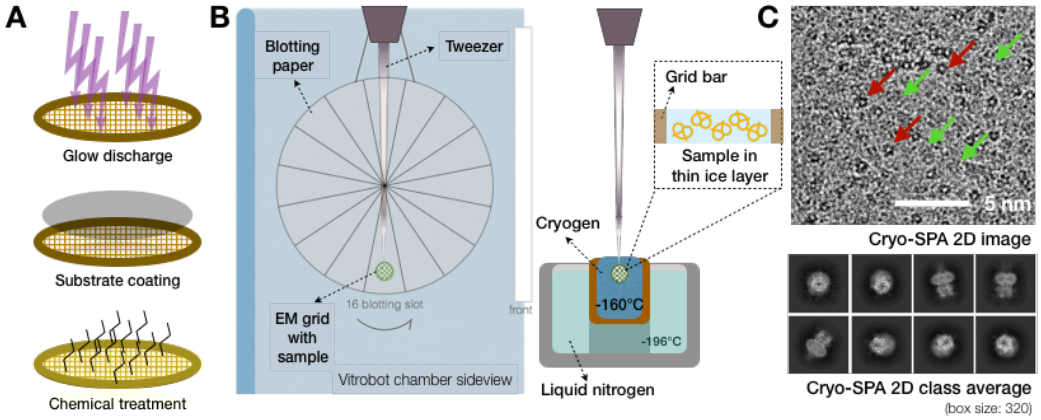

Figure 1.6 Cryo plunge freezing. (**A**) Grid pretreatment for cryo EM specimen optimization, including glow discharge, substrate coating and chemical treatment. (**B**) Schematic drawing of sample vitrification process using Vitrobot (Thermo Fisher Scientific), temperature of cryogen at ~ -160°C, required for ice vitrification. (Insert showing sample embedded in thin vitrified ice layer). (**C**) Cryo-SPA image of serotonin receptor (top, red arrows indicate some of the serotonin receptors are at their top-view oriented, and green arrows indicate for side-view oriented) and 2D averaged classes (bottom) showing various orientation of serotonin receptor in ice.

Table 1.2 Expected particle distribution on holey grids, given the concentration of protein in mg/ml and its molecular weight (MW, kDa). The table lists the expected number of single particles in cryo-SPA. The number is given per μm^2 and expected uniformly separated in the 800Å-thick ice layer. Red values represent a distribution that is too crowded, those in blue is too sparse, and those in green about right. If images of a grid showing much different number of particles, there might be something unexpected during EM specimen preparation. The table was reproduced from (Vinothkumar and Henderson, 2016) with permission. Copyright © Cambridge University Press.

Number of particles in projection per μm^2 in 800Å – thick ice-layer				
MW	**10 mg/ml**	**2 mg/ml**	**0.5 mg/ml**	**0.1 mg/ml**
10 kDa	48000 (45 Å)	10000 (100 Å)	2500 (200 Å)	500 (450 Å)
50 kDa	10000 (100 Å)	2000 (220 Å)	500 (400 Å)	100 (1000 Å)
250 kDa	2000 (220 Å)	400 (500 Å)	100 (1000 Å)	20 (0.2 µm)
1 MDa	500 (400 Å)	100 (10000 Å)	25 (0.2 µm)	5 (0.4 µm)
5 MDa	100 (1000 Å)	20 (0.2 µm)	5 (0.4 µm)	1 (1 µm)

Comparing with negative staining, the sample is fixed in its near-native state, without being dehydrated. The high cooling rate of the cryogen, commonly is liquid ethane or propane, or a mix of both (Tivol et al., 2008), allows rapid cooling and forming of thin vitreous ice film below around -160°C.

The method is still developing with newly-designed ultra-fast cryo-fixation vitrification systems, targeting on solving particular issues during plunge freezing, like prevention the biomolecules from attaching to the AWI (Jain et al., 2012), or direct preparation for sensitive proteins from its minimal amount of cell lysate for high resolution cryo-EM (Schmidli et al., 2019).

1.2.3 Other cryo specimen preparation for structural molecular biology

Cryo-ET and STA are also capable in studying the structures, like virus nucleocapsid, proteins embedded in lipid vesicles, small cells (< 3-5 µm). Under these targets, the EM specimen could be prepared as previously described in Section 1.2.2 by plunge-freezing. While, for many other targets of those biological samples with much larger size (from 10 µm up to 0.6 mm), they are too thick to get electrons transmitted. They require the application of high pressure freezing (Dahl and Staehelin, 1989) to first fix the bulky sample as frozen, which helps to preserve all components of a system or biological events in their native state. Then the frozen vitreous block needs to be further thinned, either using cryo-sectioning, or FIB-milling, to make it transparent to electron beam.

Cryo-sectioning, also known as frozen section, is used for performing microscopic analysis of a specimen. In practical, it is difficult to manipulate since the vitrified block has very high viscosity (Al-Amoudi et al., 2004). To get a thin section around 50-150 nm, needs great efforts with practice. Introducing artefacts, such as temporary warming-up, ice cube forming, vitreous block fracture during sectioning, winkled topology of the sections, poor attachment onto EM grid and so on, will cause failure of the entire work.

Cryo-focused-ion-beam milling (cryo-FIB) is introduced, to avoid the difficulties of vitreous cryo-sectioning (Hayles et al., 2007). This device using two beam FIB/SEM instruments, to allow thinning manipulation with FIB and imaging of the volume by scanning electron microscopy (SEM) at the same time. Thus, the manipulation is more precise.

Before cryo-FIB milling, a localized *in situ* chemical vapor deposition of material, is carried out via a gas injection system (GIS) to protect the surface topographical features (Hayles et al., 2007). Then a beam of focused gallium ions, is used to remove material from the surface of the vitreous sample during cryo-FIB milling. The focused and accelerated gallium ions sputtering onto the vitreous sample, takes away the surface atoms at a position that user defined. Progressively scanning the ion beam over the sample surface allows removing the materials in a successive layer-by-layer manner (Rigort and Plitzko, 2015). The plunge-freezing EM specimen could also get thinner using the cryo-FIB/SEM milling device. The technology is still under developing, needs more study on improvement of devices and methodologies to optimize the application and increasing the throughput.

1.3 Image formation and processing

Cryo-EM resolves fine structural details of the thin biological sample under characterization, through its electron beam interaction with EM specimen, forming 2D projection images and recording onto the camera devices, then giving the biology/computer scientists to align and project the information back into 3D.

There is no “easy-button on-a-click” to simply improve the resolution of the final EM map, with lots of aspects can affect it. In order to take good-use-of the microscope and get better structural details out of it, there are fundamental aspects we need to know, about the formation of the 2D projection images, how 2D images are aligned and back-projected into 3D reconstruction, and what is resolution defined in cryo-EM and how much biological information that can provide as well. In this section, we will go through a brief introduction on these aspects accordingly.

1.3.1 Image formation and contrast transfer function

Previously (Section 1.1.2), we have discussed already that electrons went through scattering contain all the information about the specimen. But for biological sample, that are mostly composed of light elements like H, C, O and N, when electrons travel through it, only a small portion of the electrons get scattered, thus the useful signal it containing about the specimen is rather weak, most are phase contrast rather than amplitude contrast (Williams and Carter, 2009d). Considering merging this important but weak signal, to those having no useful information of the specimen but rather contributing as background or noises, we would have to manage to “extract” them.

The strategy we adapt is to do periodogram averaging (Penczek et al., 1997), and rotational averaging of the image and adding up those containing similar “signal” (presents as power spectrum) as one group, so that the background could be subtracted and noises are suppressed. The way we group them is rather according to the defocus (the deviation between the focus of the objective lens from its “Gaussian focus” (Williams and Carter, 2009c) of the images. In real life, the defocus of the images usually is not the same as user-defined value during data collection (due to particles in the specimen are not embedded at the same

thickness, or tilting of specimen is introduced, also beam/lens aberrations), we would have to determine the correct defocus of the image collected.

Here, we introduce the (phase) contrast transfer function (CTF) (Erickson et al., 1971; Wade, 1992),

$$CTF(f) = E(f)\sin\left(\frac{\pi C_s \lambda^3 f^4}{2} - \pi\lambda d f^2\right)$$

where C_s is a spherical aberration of electromagnetic lens; λ is the electron wavelength; f is the spatial frequency, d is the applied defocus, $E(f)$ is an envelope function describing high resolution information degradation.

The estimation of the defocus usually done with fitting of the power spectrum of an image to a theoretical CTF value calculated at given defocus (**Figure 1.7** A). The best fitting represents the “real” defocus of the image. Envelope function has its effect on top of the defocus effect shown in **Figure 1.7** B.

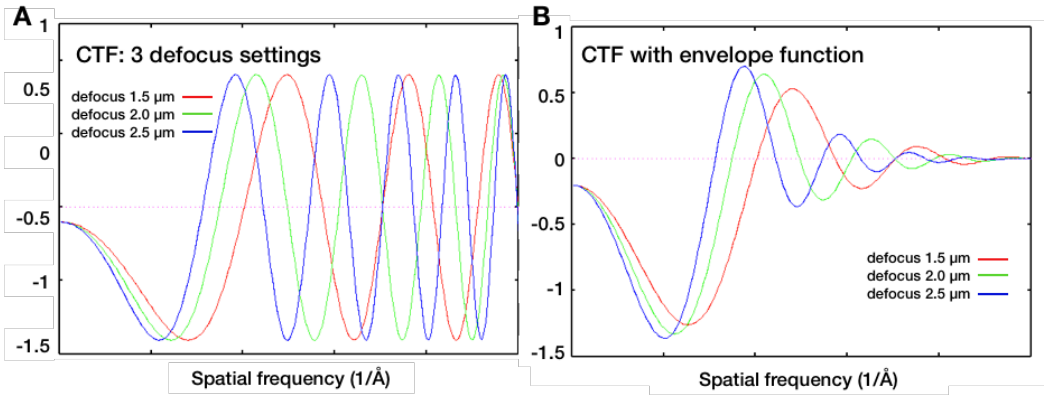

Figure 1.7 Theoretical contrast transfer function with different defocus settings. (**A**) Depending on the defocus settings, different features of the object appear enhanced or suppressed in the image. This is because the CTF oscillates between negative contrast transfer) and positive contrast transfer as we go from low to high spatial frequencies. At the exact locations of zero crossings, no contrast is transferred, information is lost. (**B**) Effect of envelope function on the damping of CTF from low to high spatial frequencies. This figure was reproduced from Spider webpage (2015).

Apart from the oscillation of CTF itself between negative contrast transfer and positive contrast transfer, the shape of CTF is also important for high frequency determination. There are several parameters related, as described in (Frank, 2006), defocus, *d* (the deviation between the focus of the objective lens from its "Gaussian focus"), spherical aberration, C_S (the third-order spherical aberration of the wave front in the objective lens), source size (the divergence of the energy source, expressed as a size in the back focal plane, hence a quantity in reciprocal space) and defocus spread (due to the variation of electron energies or the fluctuation of lens current).

Accurate CTF determination of the image allows to perform phase shift and helps to recover the high spatial frequency signal and contributes most important to push the resolution limitation of the final reconstruction. Inaccurate defocus applied, will derive a different CTF curve, that having the phase oscillating out of the real signal, and its negative effects at the high spatial frequency becomes much more significant than at lower spatial frequency. A relationship between CTF phase error at 300 kV and defocus inaccuracy is given in **Figure 1.8**.

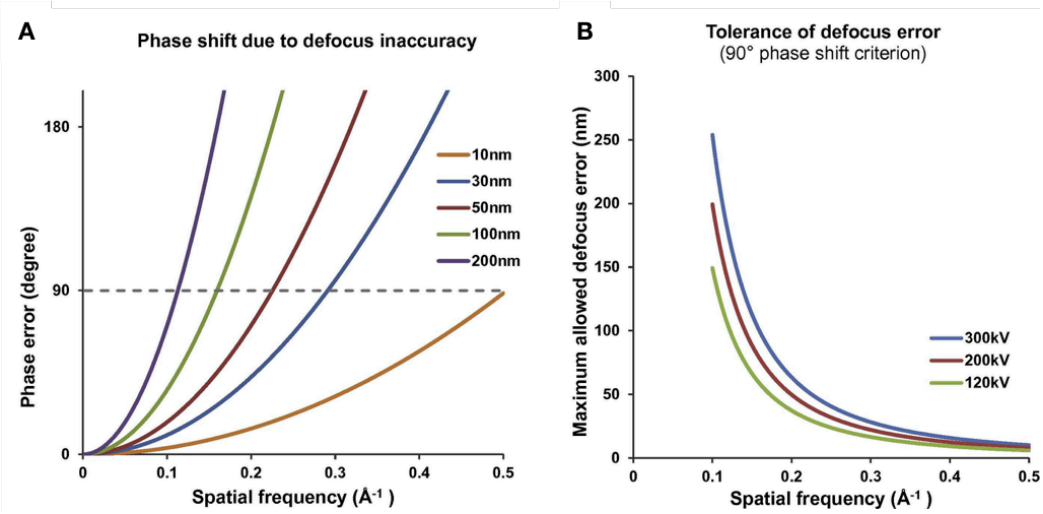

Figure 1.8 Relationship between CTF phase error and defocus inaccuracy. (**A**) The errors of CTF phases by different levels of defocus inaccuracy at 300 kV high tension. The dashed grey line represents the threshold for 90° phase shift criterion. (**B**) Based on the 90° criterion from (A), the maximum defocus inaccuracy allowed at various resolutions for three typical high tension values (300 kV, 200 kV and 100 kV) are plotted. This figure was adapted from (Zhang, 2016) with permission. Copyright © 2015 The Author. Published by Elsevier Inc.

1.3.2 3D reconstruction from 2D images

The strategy for reconstruction from 2D projections to 3D is designed based on the concept of the projection-slice theorem (**Figure 1.9** A). It states that the Fourier transform of a 2D projection of a 3D object in real-space is equivalent to taking a central 2D slice directly out of the 3D Fourier transform of that object (Bracewell, 2003).

With the concept, a projection matching procedure, shown as (**Figure 1.9** B-E), is taken to reconstruct specimen from 2D projections to 3D map, including several steps,

a. A 3D object, as initial model, is projected in all directions as references.

b. The full dataset of images is compared individually to a set of references projected from the initial 3D model, staring at low resolution (usually larger than 30Å) to avoid overfitting of noise at high resolution.

c. Once the best match, given with a height of correlation peak as comparison, is found between the image and one of the references, the shifts relative to the matching reference, and angles of that reference are assigned to the image.

d. Every iteration, new 3D map is calculated using images with the assigned angles and shifts, and the refined 3D reconstruction is then re-projected with a smaller angular increment to generate new references for the next iteration of refinement.

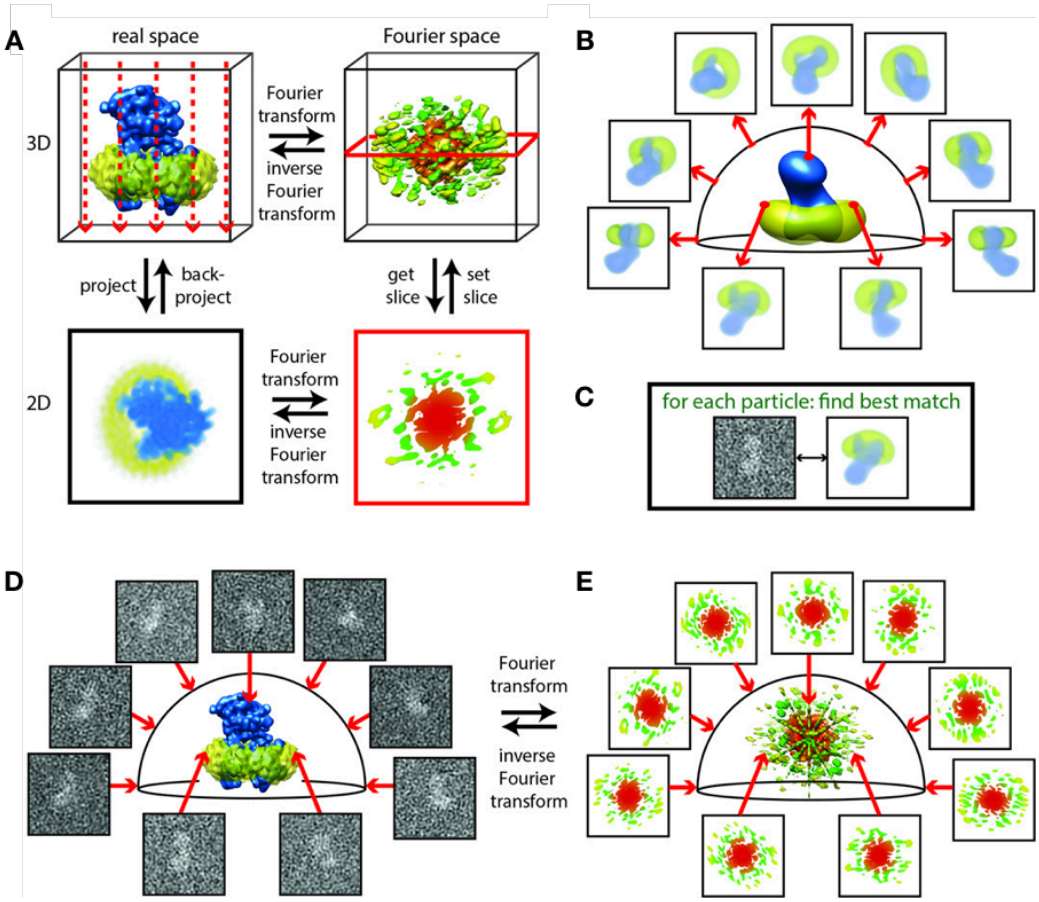

Figure 1.9 Basic concepts of cryo-EM structure determination. (**A**) The projection-slice theorem states that the 2D projection of a 3D object in real-space (left column) is equivalent to taking a central 2D slice out of the 3D Fourier transform of that object (right column) and inverse Fourier transform to real-space. (**B**) A 3D object is projected in all directions as references. (**C**) Comparison of each experimental projection with all references to find the best match of a given similarity. (**D**) Orienting all experimental projections relative to the 3D structure. (**E**) 3D reconstruction can be calculated by positioning 2D Fourier transforms of all experimental projections into the 3D Fourier transform and calculating an inverse Fourier transform. Steps (**B–E**) are performed iteratively. This figure was reproduced from (Nogales and Scheres, 2015) with permission.

1.3.3 Resolution assessment of cryo-EM structures by Fourier shell correlation

Resolution assessment in cryo-EM is to evaluate the quality of the structure reconstructed from specimen 2D projects. Currently, the method used to determine the resolution of cryo-EM structure is Fourier shell correlation (FSC), which is a function representing of spectral signal-to-noise ratio (SSNR). It is remarked in (Unser et al., 1987) that SSNR relates directly to the Fourier-based resolution criteria commonly used in crystallography (Liao and Frank, 2010). In this case, the SPA or STA dataset is divided into two half sets, and two structures are reconstructed independently, that allowing the comparison at the end for consistency by calculating correlations between the voxel values in different ranges of frequency spaces. The frequency at which the FSC drops below a defined threshold is the maximal reliable resolution. Currently, this threshold is suggested to be 0.143 by Rosenthal and Henderson, as a good indication of the “true” resolution of a cryo-EM map (Rosenthal and Henderson, 2003).

Meanwhile, over-fitting of FSC is a problem under discussion in cryo-EM, because there are much more noises than signal at the higher spatial frequency in the image, the noise tends to be aligned during iterative processing into the 3D map. Several programs are developed to reduce overfitting exaggerated resolution (Chen et al., 2013; Ramlaul et al., 2020).

To produce a map with visible high resolution features, a sharpening process is usually performed to enhance map visualization. It requires a negative *B*-factor (Fernandez et al., 2008) to be specified by user, or value estimated based on the reconstruction. With the development of the processing methods, sharpening using local map-calculated *B*-factor, is more appreciated than a global sharpening approach (Jakobi et al., 2017; Ramírez-Aportela et al., 2019).

Apart from the value given from a FSC determination, the amount of real biological features present in the map is still debatable case-by-case. Based on understanding of the need to answer biological questions, computational methods have been developed to construct a de novo atomic model from a cryo-EM density map, along with associated metadata that describe coordinate uncertainty and the density at each atom. This is informative for macromolecular assemblies that exhibit resolvability variations in different parts of their structure (Hryc et al., 2017).

1.4 Direct electron detectors

Cryo-EM has achieved its exponential success in solving the structure of biomacromolecules at a resolution below 4 angstroms in the most recent decade. One of the largest steps forward contributed to this achievement is the development of the modern direct electron detector/devices (DED) (McMullan et al., 2016). In replacement to the charge-coupled device (CCD) cameras, DED now takes its leading position with many of advantages.

The detective quantum efficiency (DQE) of a detector is one of the most important features that represents how good the performance of the detector is on recoding incident electron signal. It is given by the ratio of the square of signal to noise at output compared with input:

$$DQE = \frac{(\frac{S}{N})^2_{out}}{(\frac{S}{N})^2_{in}}$$

where *S* is the signal and *N* the noise (Williams and Carter, 2009b). The higher the DQE represents a better detection of the signal, so usually the DQE is less than 1, as the detector always add some noise to the signal. The DQE of a camera is incorporated with the detection efficiency, spatial resolution and noise properties of the detector in its definition (Faruqi, 2015).

Here, we need to introduce modulation transfer function (MTF). According to literature (McMullan et al., 2014), the MTF at spatial frequency (ω), measured in terms of the Nyquist frequency can be expressed as,

$$MTF(\omega) = sinc\left(\frac{\pi\omega}{2}\right) MTF_0(\omega)$$

where $MTF_0(\omega)$ can be viewed as the Fourier transform of an intrinsic point spread function, PSF(γ), of the detector. Point spread function (PSF) is a description of the width of the electronic noise of the detector. For its better description, author refers to the textbook (Williams and Carter, 2009e).

Using traditional CCD camera, the incident electrons at the detector need to be first converted into light with a phosphor scintillator (**Figure 1.10** A), and transferred via a lens or fiber optics. CCD camera then converts the light signal into an electronic image and read-out. During the conversion, every electron event entered into the detector as a dot is converted into a cloud of light at the sensor, which introduces unnecessary noises and suppresses the resolution of

the electronic image. In contrast, the DED records the incident electron event directly (**Figure 1.10** B), there is also electron scattering effect into point spread signal at the sensor, but comparing to CCD camera using phosphor scintillator, DED has its sensor made of silicon, with smaller atomic weight (Z), creating smaller point spread function (PSF), the primary event is rather to be identifiable within the designed physical pixel size and allowing sub-dividing of the pixels per unit of area (**Figure 1.10** C).

Furthermore, DED is fabricated using the developed monolithic active pixel sensors (MAPS) (McMullan et al., 2009) based on the complementary metal-oxide semiconductor (CMOS) technology which has a certain extend of radiation resistance, eliminating the influence by using scintillator and fiber optics, improves the performance of the detector significantly.

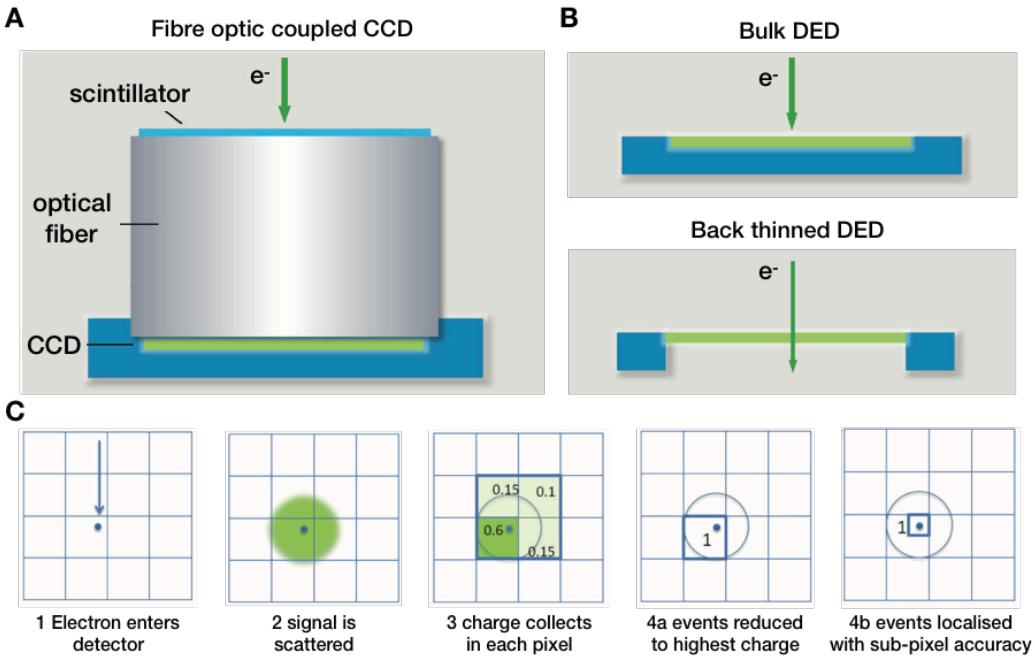

Figure 1.10 Schematic configuration of CCD and DED cameras. (**A**) Fiber optical coupled charge-coupled device (CCD) camera. (**B**) Bulk and back thinned direct electron detectors (DED). (**C**) Counting and super-resolution modes of a direct electron counting camera. Super-resolution model surpasses the theoretical information limit defined by physical pixel size. The high-speed electronics recognize each electron event (at > 400 frames per second) and finds the centre of that event with sub-pixel precision, quadrupling the effective number of pixels. This figure was reproduced from (Booth and Mooey, 2014).

The backthinning of a CMOS direct electron detector (**Figure 1.10** B) is observed experimentally improved the spatial resolution and efficiency at all spatial frequencies. With a Monte Carlo simulations of electron trajectories (**Figure 1.11**), it is showing pretty nicely that the primary electron scattering event is generated within only a few microns at the sensor, backthinning would effectively remove the backscattered electron events, which considered contributing some to the low frequency component, but mostly to the noise of the image at both low and high spatial frequency.

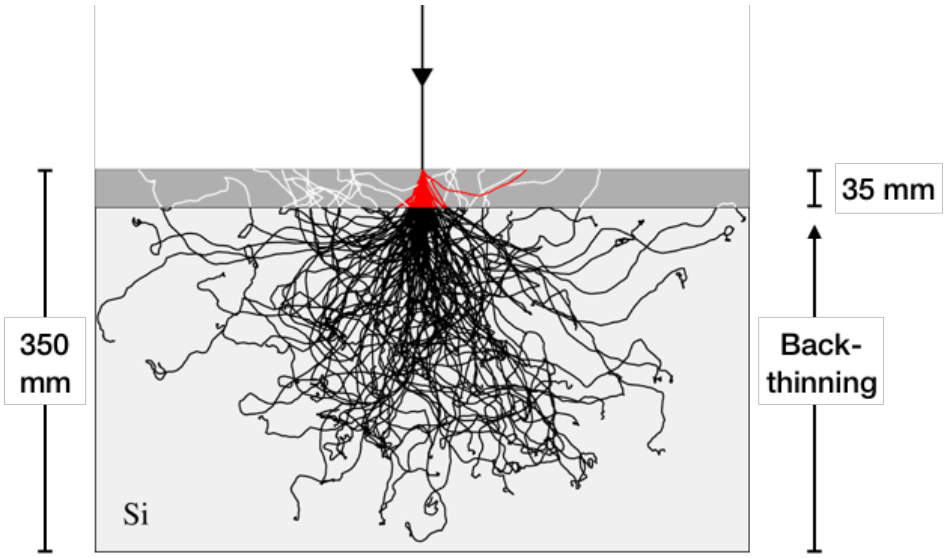

Figure 1.11 Monte Carlo simulation of 300keV electron tracks in silicon. After backthinning to 35 mm, only those parts of the electron tracks highlighted in red would contribute to the recorded signal, which therefore is expected to have a much improved modulation transfer function (MTF). Before backthinning, the additional white tracks would contribute a low-resolution component to the signal together with contributions to the noise at both low and high spatial frequencies. The overall thickness of the silicon in the figure is 350mm with the 35mm layer that remains after backthinning shown in grey. The black electron tracks in the substrate deposit energy but contribute minimally to the measured signal. This image was reproduced from (McMullan et al., 2009) with permission. Copyright © 2009 Elsevier B.V.

The experimental measurements of DQEs of the K2 Summit direct electron detector in its counting and super-resolution mode is shown, comparing to CCD camera in (**Figure 1.12** A) (Li et al., 2013a). The DQE of K2 Summit using super-resolution mode, that the electron event is sub-localized onto one quarter of its physical pixel, superior the physical Nyquist limitation and potential producing a better resolution of a collected image at both low and high spatial frequency. As electron-counting mode referring as the recoding of every individual electron, its performance would incorporate with the electron dose rate (**Figure 1.12** B), much higher dose would introduce coincidence loss, eventually reducing the detector conversion efficiency (DCE) of the camera.

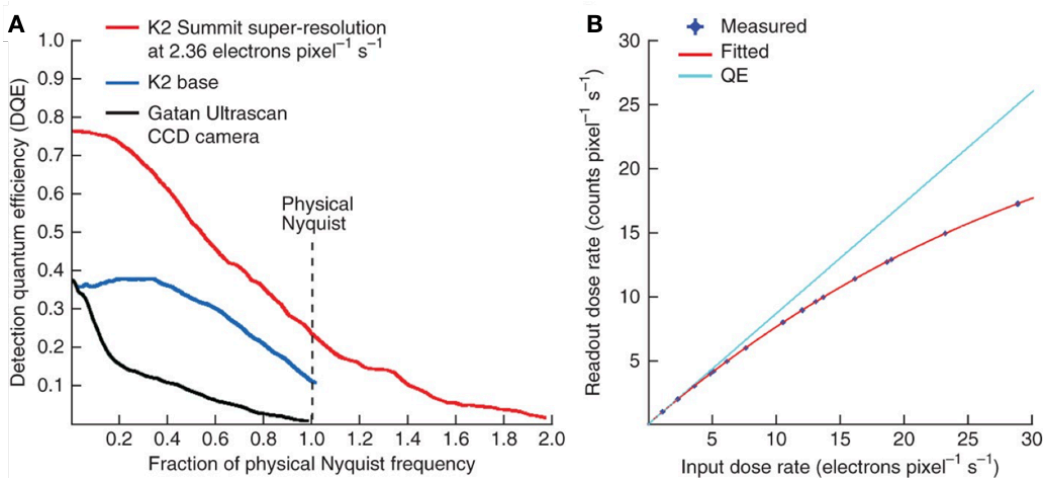

Figure 1.12 Detective Quantum Efficiency (DQE) and Detector Conversion Efficiency (DCE) of K2 Summit electron counting camera. (**A**) DQEs of K2 Summit were measured in both counting (red curve, taken at 2.36 e–/pixel/ sec) and linear charge accumulation modes (blue curve), and are compared with the DQE of a typical scintillator-based CCD camera, the Gatan US4000 Ultrascan (black). (**B**) The dose dependent DCEs of K2 Summit counting mode. Electron counts were measured as a function of incident electron dose rates and were fit to a polynomial curve. The straight line represents the ideal linear response with a slope of 0.87, corresponding to the quantum efficiency of the camera. This figure was reproduced from (Li et al., 2013a) with permission. Copyright © 2013 Nature America, Inc.

Besides, the readout time of DED, derived from MAPS that each pixel contains a photo detector, is much shorter since parallel readout of multiple channels is used with the rolling shutter. Therefore, DED provides data collection with much more rapid speed (above 1000 frames/s, or fps) than it is achievable with classical solutions e.g. with CCD camera (Deptuch et al., 2007).

Table 1.3 Physical properties of the direct electron detectors (DED). This table was reproduced from (McMullan et al., 2014) and Gatan Inc. homepage (2020), Thermo Fisher Scientific homepage (2019) with permission.

Detector	Sensor size	Pixel size (um)	Readout speed (fps)
DE-20	5120 x 3840	6.4	32.5
Falcon-II	4096 x 4096	14.0	18
Falcon-III EC	4096 x 4096	14.0	40
Falcon 4 DED	4096 x 4096	14.0	250
K2 Summit	3838 x 2710	5.0	400
K3	5760 x 4092	5.0	> 1500

Furthermore, with the fast read-out speed, as shown in **Table 1.3**, each image of the EM specimen is collected as movies with multiple frames in a short time. Superior than a single frame image collected over tens of seconds or a couple of minutes, a movie with multi-frames records the non-uniform beam-induced movement (shift and rotation) of the specimen during exposure, which could be estimated and corrected by computational algorithm based on the aligning of several patches or every individual particle, considering none of the particles would move the same to the others. It provided an effective recovery of the signal recorded, with sufficient accuracy for determination of near-atomic-resolution 3D reconstructions. The raw movie recorded with Falcon III camera in Titan Krios at 300 kV presents more accurate CTF estimation after motion correction (**Figure 1.13**).

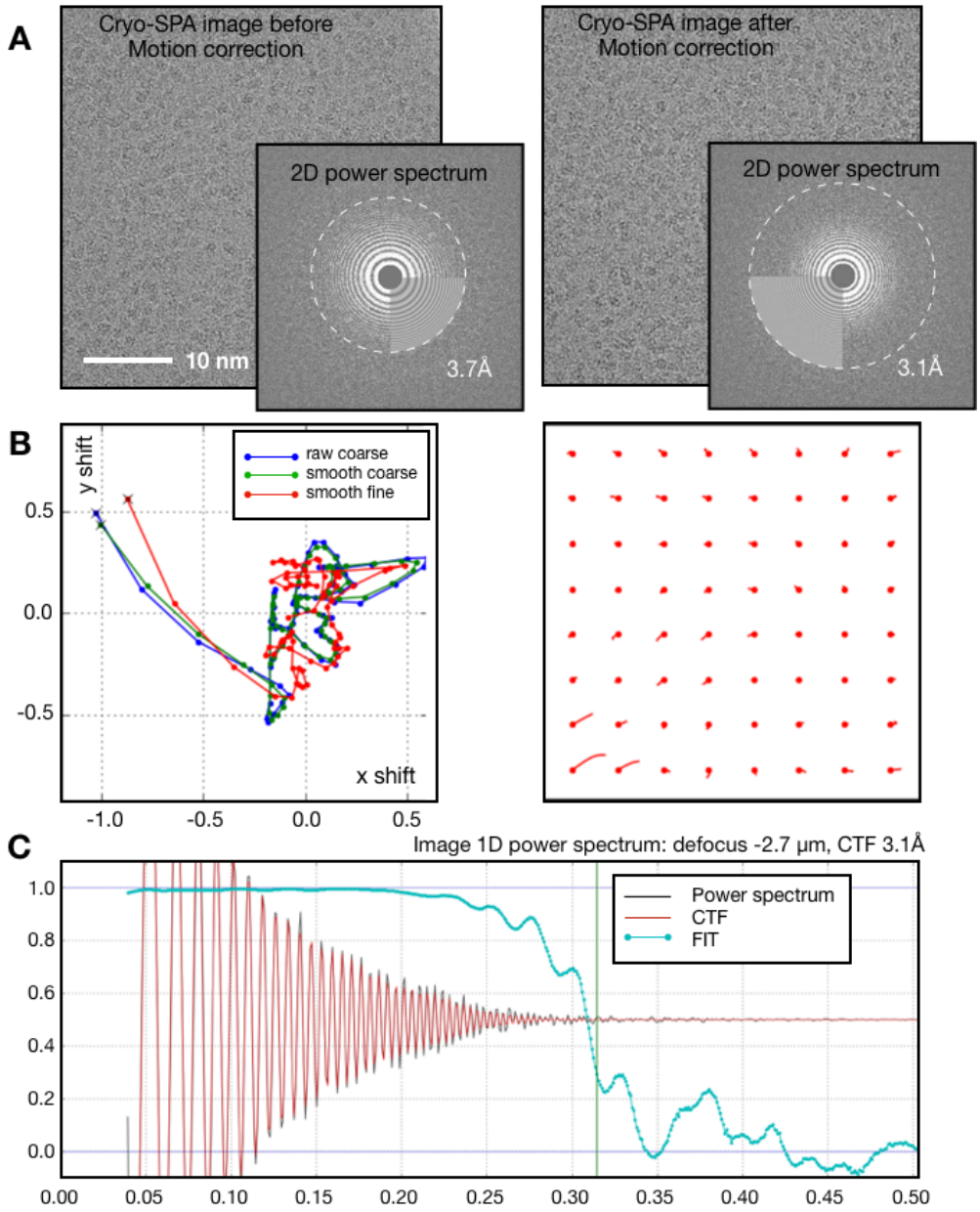

Figure 1.13 Motion correction for in-frame movements of EM specimen during exposure. (**A**) Raw cryo-EM micrographs and 2D power spectrums of serotonin receptor before and after motion correction, image looks sharper after motion correction and CTF estimation is more accurate as shown with fitted 2D power spectrum. (**B**) Align patches of micrograph and estimate local movement (left). Movement trajectories of every patch are shown in red arrow (right). (**C**) 1D power spectrum and CTF fitting of serotonin receptor cryo-EM micrograph after local movement correction.

1.5 Practical aspects of data collection and processing

The workflows of the two major cryo-EM applications are introduced as flow chat with brief description in this section, giving a fulfilled picture of them as methodology instructions, would facilitate the understanding of the results on method development in Section 3.7.

1.5.1 Well-established cryo-SPA workflow

A well-established cryo-SPA workflow, involving couples of newly-developed automated tools, are described below includes (**Figure 1.14**),

a. Automated data collection: data automatic collection with commercial and academic packages available, like EPU (Thermo Fisher Scientific), SerialEM (Mastronarde, 2005), Leginon (Suloway et al., 2005), UCSFImage4 (Li et al., 2015) and others (Tan et al., 2016).

b. Data preprocessing: motion correction (Zheng et al., 2017) and CTF estimation (Rohou and Grigorieff, 2015; Zhang, 2016) of the automated raw movies. The preprocess analysis could also be done on-the-fly in order to facilitate sample screening and effective data collection, with several developed packages, like Appion (Lander et al., 2009), FOCUS (Biyani et al., 2017), Warp (Tegunov and Cramer, 2019), cryoSPARC Live (Punjani et al., 2017). MicAssess (Li et al., 2020) is another tool released recently for determination on the best parameters for particle picking and 2D classification, and identification the good class averages that can be used in 3D reconstruction.

c. Particle picking and extraction: particle picking is rarely done manually today, with the development on automated picking packages with and without template, including Gautomatch (Zhang, 2017), cryoSPARC (Punjani et al., 2017), APPLE picker (Heimowitz et al., 2018); or by convolutional neural network training, including SPHIRE-crYOLO (Wagner et al., 2019).

d. 2D classification: for estimation on the heterogeneity and integrity of the particles extracted, and removing of “junk” particles during auto-picking. This could also be done on-the-fly with the above mentioned preprocess packages in step **b**. The algorithm that RELION adapts is Maximum likelihood. It utilizes the underlying statistics of the picked particles to calculate the likelihood that a given particle belongs to a given 2D class within the dataset (Scheres, 2012).

e. 3D refinement: 3D refinement of the selected good particles form step **d**, and refining against 3D reference initial model. The 3D initial model could be generated Ab-initio from selected 2D classes, or from a low pass filtered (normally ~ 50 Å) EM volume/model, for instance, available at electron microscopy data bank (EMDB).

f. 3D classification: for heterogeneous particle sets, 3D classification is done with each particle aligning to multi-references iteratively. Besides, 3D classification sometimes is directly adapted in replacement of 2D classification to clean the particle stacks. The classified good particles within a class, showing sharper features, is sent to further 3D refined. This process including step **d**, **e**, **f** normally done with several rounds. Packages available includes IMAGIC (van Heel et al., 1996), XMIPP (Sorzano et al., 2004), Frealign (Grigorieff, 2016), EMAN2 (Bell et al., 2016), cryoSPARC (Punjani et al., 2017), RELION-3.0 (Zivanov et al., 2018).

g. Map based CTF refinement (Zivanov et al., 2018) and dose-weighting on the final map with good particles.

h. Postprocessing: standard operations including map sharpening (for high resolution feature visualization and eventually model building) and local resolution estimation. 3DFSC estimation (Tan et al., 2017) and MonoRes (Vilas et al., 2018) are optional to estimate efficiency of particle orientation effects on local resolution. SIDESPLITTER (Ramlaul et al., 2020) is optional to estimate local resolution over-fitting.

In addition, processing steps may include particles focused classification (von Loeffelholz et al., 2017) for sample showing higher flexibility at different regions, symmetry expansion for improving local alignment and localized reconstruction on subunits (Ilca et al., 2015), image anisotropic magnification distortion

correction for large specimen with molecule weight in MDa (Zhao et al., 2015), also image aberration correction for dataset collected with beam tilt aiming for higher throughput (Wu et al., 2019).

Besides, the atomic model could be built manually against the final consensus cryo-EM map using packages like COOT (Emsley et al., 2010), and refined with PHENIX (Adams et al., 2002).

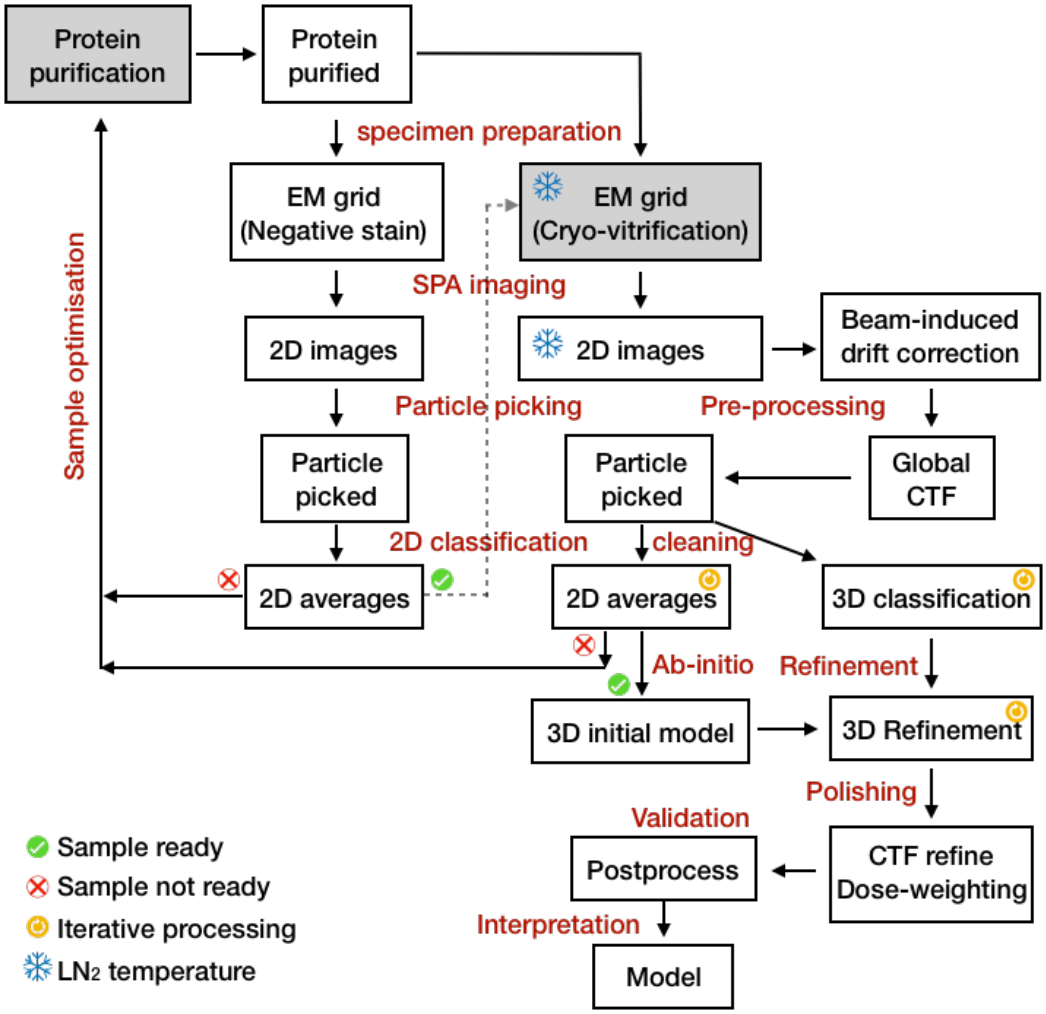

Figure 1.14 Cryo-SPA workflow. Starting from purified sample, cryo-EM SPA normally involves a negative stain (NS) screening step in order to make sure sample as expected. When it looks homogenous as 2D averaged classes, the sample could be taken starting to do cryo-SPA. The grey boxes indicate where it normally requires exclusive optimization. Iterative processing steps are indicated with yellow symbol.

1.5.2 Conventional cryo-ET and STA workflow

A conventional cryo-ET and STA workflow includes (**Figure 1.15**),

a. Tilt-series collection: collecting tilt-series as dose-fractionated 2D projections, using bi-directional tilting scheme or dose-symmetric tilting scheme (Hagen et al., 2017), with certain increments (normal 1-3°) until the maximum tilting angles of the stage are reached on both sides.

b. Tilting stack creation: aligning each of the dose-fractionated movie in the tilt-series into motion-corrected 2D projections for each tilting degree, and creating a tilt-stack. Global CTF estimation for each motion-corrected 2D projections could be done at this step.

c. Tilt-stack alignment: aligning each of the motion-corrected 2D projection in the stack based on specimen geometry and locations, typically using gold fiducial marker to improve the aligning accuracy. Packages available for tilt stack alignment includes IMOD, AuTom, Protomo, Alignator, RAPTOR, and TomoJ (Leigh et al., 2019).

d. Tilt-stack CTF correction: take the defocus estimated in step b, and performing contrast transfer function (CTF) correction on aligned tilt-stack.

e. Tomographic reconstruction: generating tomographic reconstructions using the CTF-corrected aligned tilt-stack at different binning sizes for different usages like visualization or particle picking/extraction, and averaging.

f. Particle picking and extraction: particle picking on the tomogram and sub-volume extraction with given box size.

g. Sub-volumes alignment: aligning of the extracted sub-volumes (particles) to a common average iteratively, following with optional multi-reference alignment (3D classification).

Additional steps may include 3D CTF correction (Kunz & Frangakis, 2016; Turoňová et al, 2017; Bharat et al, 2015), correction for local sample deformation based on gold fiducial marker alignment (Fernandez et al, 2019), and/or constrained refinement of tomographic geometry based on the positions of the particles (Bartesaghi *et al*, 2012; Himes & Zhang, 2018).

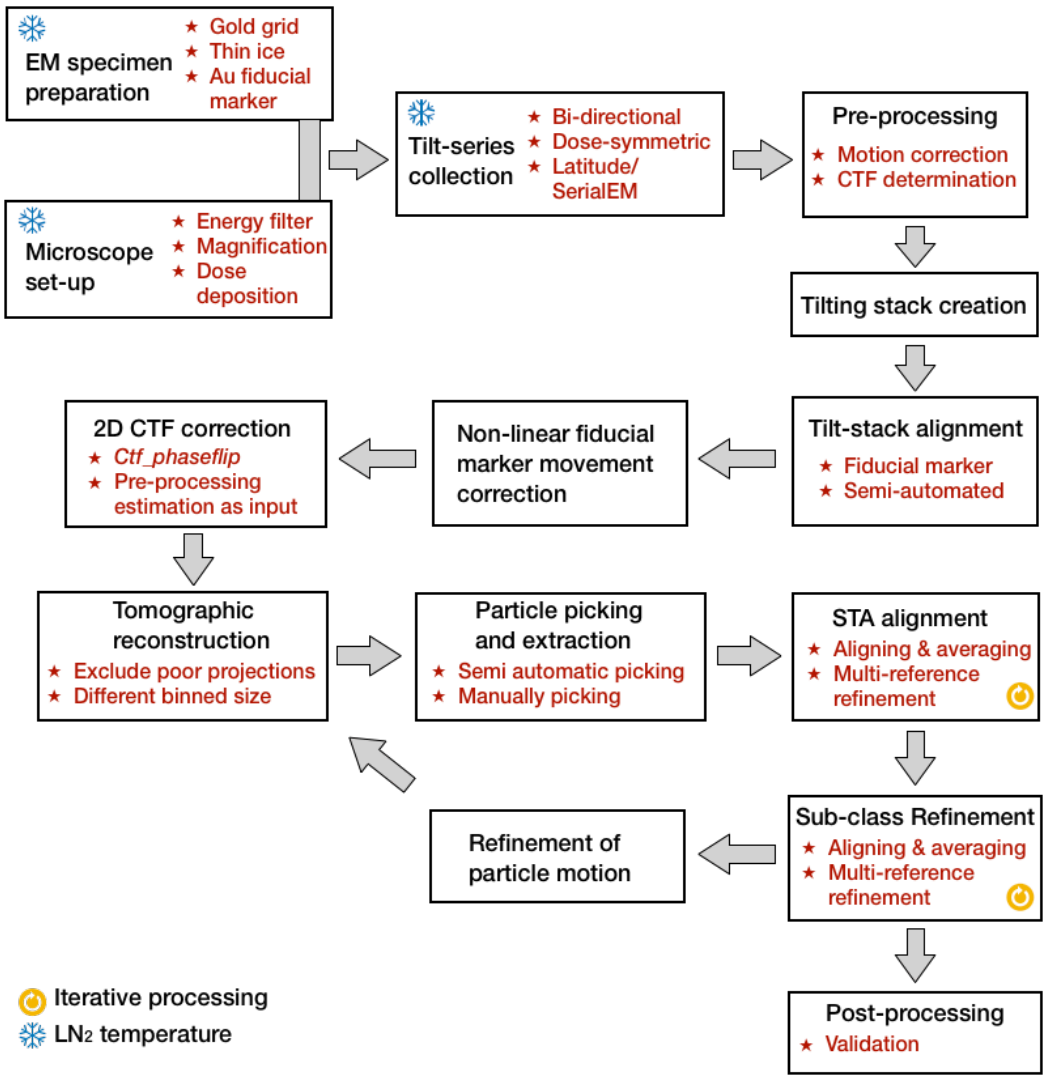

Figure 1.15 Conventional cryo-ET and STA workflow. Starting from EM specimen preparation and microscope aligning with user-justified magnification, electron dose, defocus and so on. Iterative processing steps are indicated with yellow symbol.

1.6 Pentameric ligand gated ion channels (pLGICs) and Cys-loop receptors

Pentameric ligand-gated ion channels (pLGICs) are membrane protein complexes with its eukaryotic homologs commonly including *Torpedo* nicotinic acetylcholine receptor (nAChR), gamma/γ-aminobutyric acid receptor type A ($GABA_AR$), serotonin receptor type 3 ($5HT_3R$), glycine receptor (GlyR) , zinc-activated cation channel, invertebrate glutamate-gated chloride channel (GluCl), and prokaryotic homologs including bacterial *Erwinia chrysanthemi* pentameric ligand-gated ion channel (ELIC) and the *Gloeobacter violaceus* pH-sensitive channel (GLIC) (Wu et al., 2015). **Figure 1.16** presents an overview of the various pLGICs structures resolved in different physiological conditions by X-ray crystallography and cryo-electron microscopy that available in database.

The eukaryotic pLGICs perform significant fast synaptic signal transduction by opening an embedded pore and allowing ions moving freely across membrane upon ligand activation (Jackson and Yakel, 1995; Wirth et al., 2017). The ligands are various types of neurotransmitters including acetylcholine (ACh), gamma/γ-aminobutyric acid (GABA), serotonin (5-HT) and glycine (Dent, 2010).

The pLGICs could be classified based on their ion selectivity (**Table 1.4**), cation- or anion-selective, which inducing either a depolarization or hyperpolarization effect upon ligand activation (Tovar and Westbrook, 2012). The nAChR, $GABA_AR$, $5HT_3R$ and GlyR also known as the Cys-loop receptors, which evolved from a common ancestral gene (Ortells and Lunt, 1995). In the following Sections 1.6.1 and 1.6.2, the typical cation-selective nAChR and anion-selective $GABA_AR$ would be introduced, before we introduce our main research topic, the $5HT_3R$ in Section 1.7.

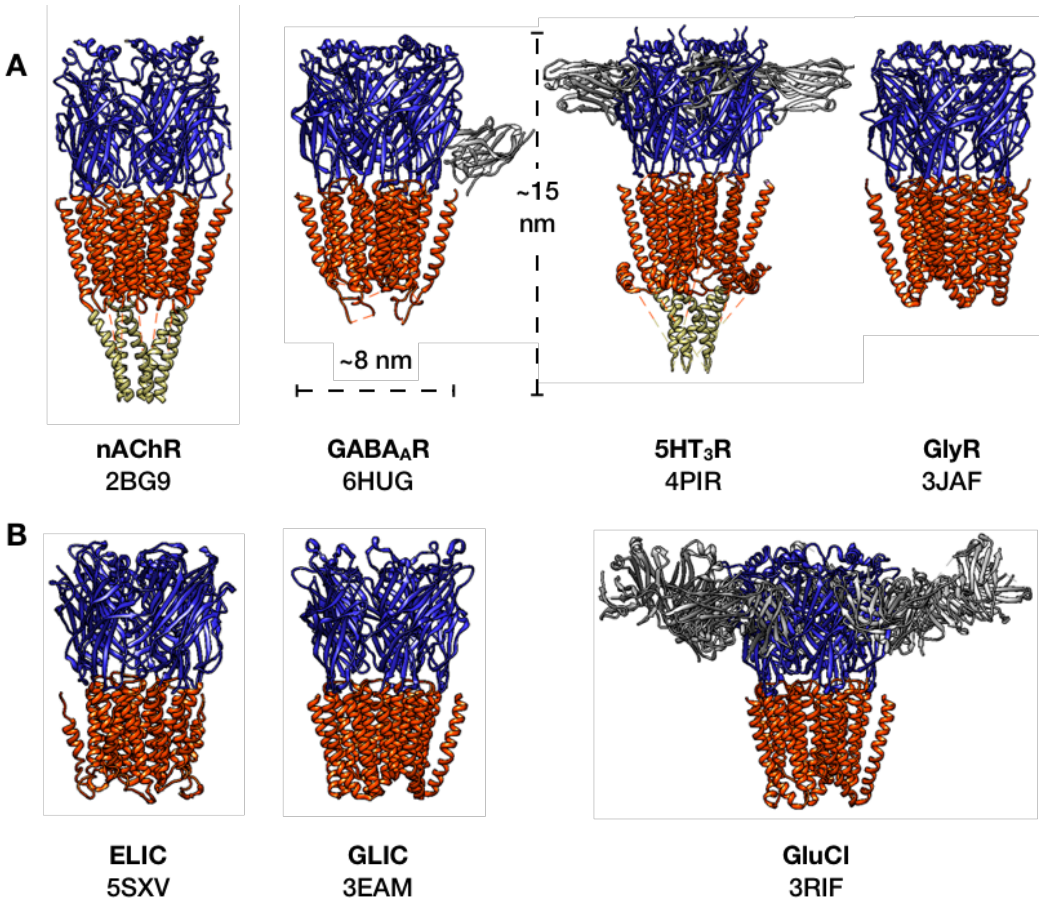

Figure 1.16 An overview showing the structural architecture of eukaryotic and prokaryotic pLGICs. (**A**) Structure of the nicotinic acetylcholine receptor (nAChR) from *Torpedo* (Left; PDB-2BG9) (Unwin, 2005); γ-aminobutyric acid receptor type A ($GABA_AR$) (middle; PDB-6HUG) (Masiulis et al., 2019); serotonin receptor type-3 ($5HT_3R$) (PDB:4PIR) (Hassaine et al., 2014); and Glycine receptor (GlyR) (right; PDB-3JAF) (Du et al., 2015). (**B**) Structures of the prokaryotic pLGICs, ELIC (left; PDB-5SXV) (Chen et al., 2017) and GLIC (middle; PDB-3EAM) (Bocquet et al., 2009), and the *C. elegans* GluCl (right; PDB-3RIF) (Hibbs and Gouaux, 2011). Only the receptors are coloured in medium blue at ECD, orange red at TMD, and dark khaki at ICD with any other stabilizing nanobodies shown in grey for clarity.

Table 1.4 Ligand, ion selectivity of eukaryotic pLGICs.

Receptor	Ion Selectivity*	Ligand
nAChR	Na/K/Ca	Acetylcholine
$GABA_AR$	Cl	GABA
$5HT_3R$	Na/K/Ca	5-HT
GlyR	Cl	Glycine

* Na: sodium permeable; K: potassium permeable; Ca: calcium permeable; Cl: chloride permeable

In order to understand how pLGICs mediating on fast neurotransmission, their structures have been extensively studied, especially for nAChR from *Torpedo* and gamma/γ-aminobutyric acid receptor type A ($GABA_AR$), in order to reveal the functional basis on gating of pLGICs. These earlier structural studies with X-ray crystallography (Brejc et al., 2001; Celie et al., 2005; Hassaine et al., 2014; Huang et al., 2015; Miller and Aricescu, 2014) and cryo-electron microscopy (Du et al., 2015; Laverty et al., 2019; Unwin and Fujiyoshi, 2012) had revealed an identical monomer topology among pLGICs - a N-terminal ligand binding pocket at its extracellular domain (ECD) with ligand binding pocket (LBP), four transmembrane helices M1-M4 at transmembrane domain (TMD) with M2 helix as the most constrain lining the pore, and one intracellular domain (ICD), including a disordered stretch often truncated/digested from its full-length or not resolved in the cytoplasmic side. The pLGICs are made of such five identical or homologous symmetrically arranged monomers, oligomerizing into a cylinder-shaped complex with about ~12-15 nm in height and ~8 nm in diameter, with the rotational axis coincides along the ion pathway.

Despite how consistent the topology is, functional studies, such as changes in affinity of agonist or antagonist, single channel conductance and whole cell patch-clamping electrophysiology studies of pLGICs in membrane with different lipid compositions have suggested that the pLGICs adapt massive different conformations that are lipid-dependent (Addona et al., 1998; Hosie et al., 2006; McCarthy and Moore, 1992; Sunshine and McNamee, 1994). Besides, EPR spectroscopy and Infrared difference spectroscopy studies suggested that the conformational dynamics of pLGICs in different membrane was in a tertiary or quaternary level (Ellena et al., 1983; Ryan et al., 1996). Since then, structural studies also have taken lipids/steroid into account, in aim of pointing out the

effects of lipid-protein interactions on functionality of pLGICs. A couple of lipid-modulation studies of different pLGICs have revealed and suggested their direct interactions at different sites in atomic-level. More details are described in the following Sections 1.6.1 and 1.6.2.

1.6.1 Cation-selective pLGICs: Nicotinic acetylcholine receptors (nAChRs) structure and lipid allosteric modulation

Nicotinic acetylcholine receptor (nAChR) of *Torpedo* electric tissue was the first electro-physiologically studied and biochemical identified neurotransmitter receptor in early 1970's (Changeux et al., 1970; Miledi et al., 1971). Its cationic-selectivity is triggered by binding nicotinic agonists, and inhibited with antagonist like mecamylamine (Hama and Menzaghi, 2001). The nAChRs have 17 homologous polypeptides (Kalamida et al., 2007), can be classified into 5 muscle nAChR subtypes (α1, β1, γ/ε, δ) and 12 neuronal nAChR subtypes (α2–10, β2–4). In consequence, there are many nAChR homo- and hetero-oligomeric subtypes, composing of different combinations of specific subunits, mediate diverse physiological functions.

The major step forward for the conformational study was the reporting of a refined 4 Å cryo-electron microscopy structure of the 2D crystals formed by membrane-associated *Torpedo* acetylcholine receptor (nAChR), revealing all the main functional regions of the nAChR with secondary structural details (Unwin, 2005). ACh-induced conformational changes of hetero-pentamer nAChR reported by Unwin and colleagues (Unwin and Fujiyoshi, 2012) suggest that asymmetric motions of the different subunits ultimately lead to relatively large changes in conformation of the β subunit, which plays the key role in transmitting changes from the agonist-binding site to the channel gate (daCosta and Baenziger, 2013).

The earliest hypothesis on allosteric transition with binding of neurotransmitter mediating signal transduction was proposed since 1960's, and allosteric transition was considered as a global conformational changes of the entire oligomer including binding at the LBPs in the ECD and the pore resizing along the TMD.(Changeux et al., 1967; Changeux, 1966). The postulated allosteric transition model by Monod, Wyman, and Changeux was named as MWC (Monod-Wyman-Changeux) theory, or MWC model (Changeux, 2012; Changeux and Edelstein, 2005). It describes that the existence of reversible equilibrium between a couple of global conformational states, called as a resting closed state

and an active open state, even without the presence of agonist. With the presence of agonist, as the effect of agonist binding and un-binding, the population of different states would change with energetic preferences.

Figure 1.17 shows a schematic diagram of kinetics of the ligand-gated ion channels (Tovar and Westbrook, 2012). A transition from resting to open state requires at least binding of two ligands shown as the diagram (**Figure 1.17** B), was revealed with patch-clamp recordings on a constructed chimera homomeric Cys-loop receptor composed of the ligand binding domain from the α-7 nicotinic receptor, but pore-forming TMD and cytoplasmic domains from the $5HT_{3A}R$ (Rayes et al., 2009).

Earlier structural study of nAChRs has taken membrane into consideration (Miyazawa et al., 2003), now with revealed finer structural details and postulated gating mechanism of pLGICs its own, many studies have reported cholesterol regulation on nAChR function and conformation (Fantini and Barrantes, 2009). For instance, mutagenesis study of the human Nicotinic α4β2 receptor (Paradiso et al., 2001) suggested a single tryptophan and a sequence (AGMI) at the end of the C terminus forms the binding site for steroids through π-π interaction. The equilibrium binding affinity and allosteric coupling study of nAChR (daCosta and Baenziger, 2009) in different membrane environments demonstrated POPC as a negative allosteric modulator that having its transmembrane pore region “uncoupled” from the agonist-binding sites, led to the receptor adapted a conformation showing no response to the presence of its agonist or desensitizing local anesthetic. Furthermore, it has been predicted the importance of M4 helices as a lipid-sensor that regulated the potentiation of gating by mediating ECD-TMD interface (composed of pre-M1, post-M4, Cys-loop, loop F and M2-M3 linker) (Baenziger et al., 2015).

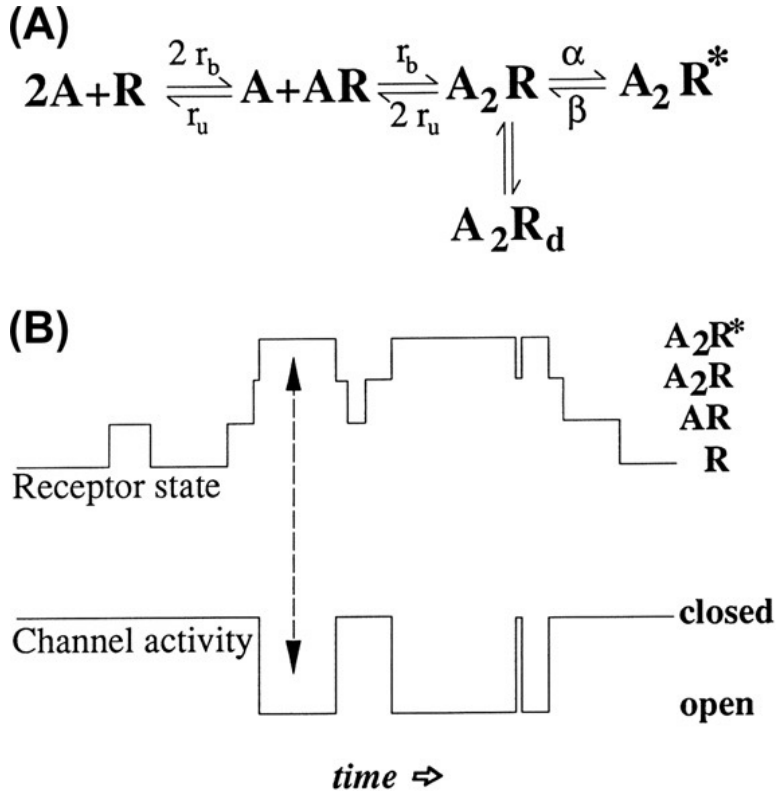

Figure 1.17 Kinetics of ligand-gated ion channels. (**A**) Example of a four- state kinetic scheme used to describe the behavior of ligand-gated ion channels. In this example, two agonist molecules (A) must bind before the channel can open (A2R*) or enter a non-conducting desensitized state ($A2R_d$). The rate constants for agonist binding and unbinding are designated r_b and r_u, and the rate constants for channel opening and closing are designated as α and β. (**B**) Relationship of the state of the receptor to the open and closing of the channel. The channel starts opening only after the receptor is in the A2R* state as indicated by the arrows. (Tovar and Westbrook, 2012). Reproduced with permission. Copyright © 2012 Elsevier Inc.

1.6.2 Anion-selective pLGICs: Gamma-aminobutyric acid type-A receptor ($GABA_AR$) structure and lipid allosteric modulation

This section we will introduce mainly of an anion-selective pLGICs: Gamma/γ-aminobutyric acid type-A receptor ($GABA_AR$) (Sigel and Steinmann, 2012), which is the principle mediators of fast inhibitory synaptic transmission in mammalian brain and other central nervous system.

Gamma/γ-aminobutyric acid type-A receptor ($GABA_AR$), found at 20-50% of synapses in the brain, suppresses neuronal activities by activated upon binding with γ-aminobutyric acid (GABA) and allowing chloride permeation through its opened transmembrane channel under physiological conditions. Many types of psychiatric disorder are considered relevant to the dysfunction of $GABA_AR$ (Nutt and Malizia, 2018). Its allosteric modulation with different drugs are of researchers' great interests for therapeutic purposes, including benzodiazepines the first one brought into clinic usage (Nutt and Malizia, 2018), volatile, and intravenous anesthetics. Others like, neurosteroid and alcohol are also found as allosteric modulators of $GABA_AR$ (Chen et al., 2017).

Since 1992, there have been nineteen types of $GABA_A$ subunits (α1-6, β1-3, γ1-3, ρ1-3, and single δ, ε, π, and θ subtypes) experimentally identified and grouped according to their sequence similarity (Laurie et al., 1992; Olsen and Sieghart, 2009), which are different in abundance in cells throughout the nervous system. These subunits contribute all together to the heterogeneity and functionality of the homo- and hetero-pentameric $GABA_AR$ receptors.

Conformational characterization of several different $GABA_ARs$ have been achieved successfully, including a 3 Å crystal structure of the human β3 homo-pentameric $GABA_AR$ bound with benzamidine (an agonist) representing a desensitized state (Miller and Aricescu, 2014); two different 3.9 Å cryo-EM structures of the Human α1β2γ2 $GABA_AR$ in complex with GABA and the benzodiazepine site antagonist flumazenil, revealing the heteromeric interaction between subunits (Zhu et al., 2018); a 3.2 Å cryo-EM structure of the human α1β3γ2 $GABA_AR$ in lipid nanodisc revealing a role of PIP_2, important component of the inner leaflet of plasma membranes, in regulating receptor trafficking (Laverty et al., 2019); and a 3.1 Å cryo-EM structure of the human α1β3γ2

$GABA_AR$ in lipid nanodisc bound to its channel-blocker picrotoxin (Masiulis et al., 2019).

The conformational details presented in these researchers demonstrated $GABA_AR$ having its common structural features shared with the entire pLGICs and Cys-loop receptor family. Every subunit is composed of an extracellular N-terminal domain containing the Cys-loop and LBP, followed with four TM helices (TM1-TM4) at the cross of the membrane region; and a large intracellular loop between TM3 and TM4. The gating mechanisms of $GABA_AR$ is still under debate including implicated regions of the loop-F modulated by benzodiazepines-bound, M2-M3 loop (Kash et al., 2003), β4-β5 linker of β subunit (Venkatachalan and Czajkowski, 2012), which supports that the gating of the $GABA_AR$ induced by ligand binding is a global transition process.

In these studies, effect of lipid allosteric modulation on $GABA_AR$ has been noticed. In the cryo-EM study of a human synaptic $GABA_AR$ (Zhu et al., 2018) observed a cholesterol binding site at membrane-subunit interface in the TMD between two adjacent subunits, forming extensive contracts with the transmembrane helices. Mutation of this tryptophan and the sequence eliminated the ability of steroid to potentiate this receptor. Beside, X-ray crystallography study of the invertebrates glutamate-gated chloride channel (GluCl) (Althoff et al., 2014), also anion-selective pLGICs, revealed a POPC-bound Apo conformation, that with POPC bound between subunits, near the extracellular side of the transmembrane domain, with their head groups wedged between the M1 and M3 helices of adjacent subunits. Having POPC-modulation, the Apo form of GluCl presented an expanded, open-like conformation of its TMD, demonstrated that POPC played a role as a positive allosteric modulator and potentiating agonist binding through direct interaction with allosteric binding pocket.

1.7 Serotonin receptor type-3 ($5HT_3R$)

Serotonin/ 5-hydroxytryptophan (5-HT), neurotransmitter, binds to serotonin receptors and regulates fast post-synaptic signaling. Serotonin receptor includes seven sub-families ($5HT_{1-7}R$), mostly belongs to G-protein coupled receptor (GPCR) family, except serotonin receptor type-3 ($5HT_3R$). Serotonin $5HT_3$ receptor, which is a cation-selective pLGIC and belongs also to the Cys-loop receptor family, has been implicated in many brain functions. It produces strong and fast depolarization upon serotonin activation, with its membrane-spanning ion pathway opening and selectively allowing cations, such as Na^+, K^+ and Ca^{2+} ions, to translocate through the postsynaptic cells. Dysfunction of $5HT_3R$ in considered relevant to several psychiatric and gastrointestinal conditions (Eisensamer et al., 2005). Antagonists binding of $5HT_3R$ (Espinosa Bosch et al., 2017; Zarkadas et al., 2020), such as binding of palonosetron, granisetron, tropisetron, ondansetron, have anxiolytic and antiemetic effects in humans and in animal models (Harvey Sternbach, 1991), which has make it an important therapeutic target for the treatment of emesis. A better understanding of its different conformations in response to agonists and antagonists binding, with the presence of membrane environment, are essential of drugs and treatments designing.

Serotonin $5HT_3R$ has several subunit classes, but only two of them are well documented as $5HT_{3A}$ and $5HT_{3B}$ subunits (Maricq et al., 1991; Nemecz et al., 2016; Peters et al., 2004). They construct as homopentamers of $5HT_{3A}R$ with five identical subunits, or they form heteropentamers of a repertoire of distinct subunit classes of $5HT_{3A}$ and $5HT_{3B}$ (Peters et al., 2004). The different oligomers present markedly different single-channel conductance being 0.4 pS for homomeric (Brown et al., 1998) and 16 pS for heteromeric (Davies et al., 1999), respectively. Throughout the thesis and this project, we are focusing on the introduction, characterization and discussion of the homopentameric $5HT_{3A}R$.

Electrophysiological studies have revealed the serotonin binding affinity of wild type $5HT_3R$ is in a range around one-hundred to several-hundreds of nM (Hovius et al., 1998; Jackson and Yakel, 1995; Thompson and Lummis, 2013). Combining with point mutagenesis studies and application of fluorescence-labelling antagonists measurements (Schreiter et al., 2003), functional sites are well-predicted and characterized in terms of loss and gain function. Also, the studies with different concentration of agonists applied has revealed its differential effects on the kinetics of $5HT_{3A}R$. The activation time of the receptor is in the ms range

(from several to a couple of hundred ms), and the activation rate increases with the increasing of the concentration of 5-HT and reaches its highest by applying 100 µm 5-HT (Corradi et al., 2009; Solt et al., 2007). These well-established experiments and studies helped to understand the functional behavior of the $5HT_{3A}R$ in response to ligand binding and unbinding, establishing allosteric kinetic models among different conformational states (resting – open – desensitization – resting), which is of great importance for the structural characterization studies.

The first high resolution $5HT_3R$ structure was resolved by using X-ray crystallography (PDB-4PIR) (**Figure 1.18** A) on a detergent solubilized mouse $5HT_{3A}R$ with nanobodies stabilized in its resting conformation at 3.5 Å resolution (Hassaine et al., 2014). The resolved structure is in good quality for most regions, including well-resolved ECD, the approximate 40-Å-long transmembrane pore, and part of its intracellular domain. It revealed the five-fold symmetry of $5HT_3R$ around a central ion pathway perpendicular to the membrane plane, and a similar architecture at ECD and TMD to other pLGICs (**Figure 1.16** A). Afterward, there are several cryo-EM structures without (Basak et al., 2018b) (**Figure 1.18** A) and with the presence of serotonin reported (Basak et al., 2018a; Polovinkin et al., 2018) (**Figure 1.18** B), revealed the resting and serotonin-bound states of the detergent solubilized mouse serotonin $5HT_{3A}R$, helped to understand the agonist induced conformational changes. Most recently, cryo-EM study has reported the palonosetron-bound mouse serotonin $5HT_{3A}R$ at 2.8 Å resolution, establishing the inhibition mechanism by the –setron drug family (Zarkadas et al., 2020) (**Figure 1.18** C).

Currently, to assign these serotonin-bound conformations as open conformation is still under discussion with the insistence of, for instance MD simulation studies (Guros et al., 2020). An unambiguous open-conformation of the $5HT_{3A}R$ allowing free ion permeation is still under revealing and highly demanded for understanding of the gating mechanism of $5HT_3R$ serotonin receptor. Moreover, giving the structural homology between $5HT_3R$ and the nAChR (**Figure 1.16**), specific lipid-modulation or cholesterol-regulation on $5HT_3R$ gating is on particularly interest. Combining of these two aspects, our research aims in this project become clearer. Starting from Chapter 2, we will describe the methods used in this project and Chapter 3 and 4 are the results and discussions of our work, followed with conclusion and perspective in Chapter 5 and 6.

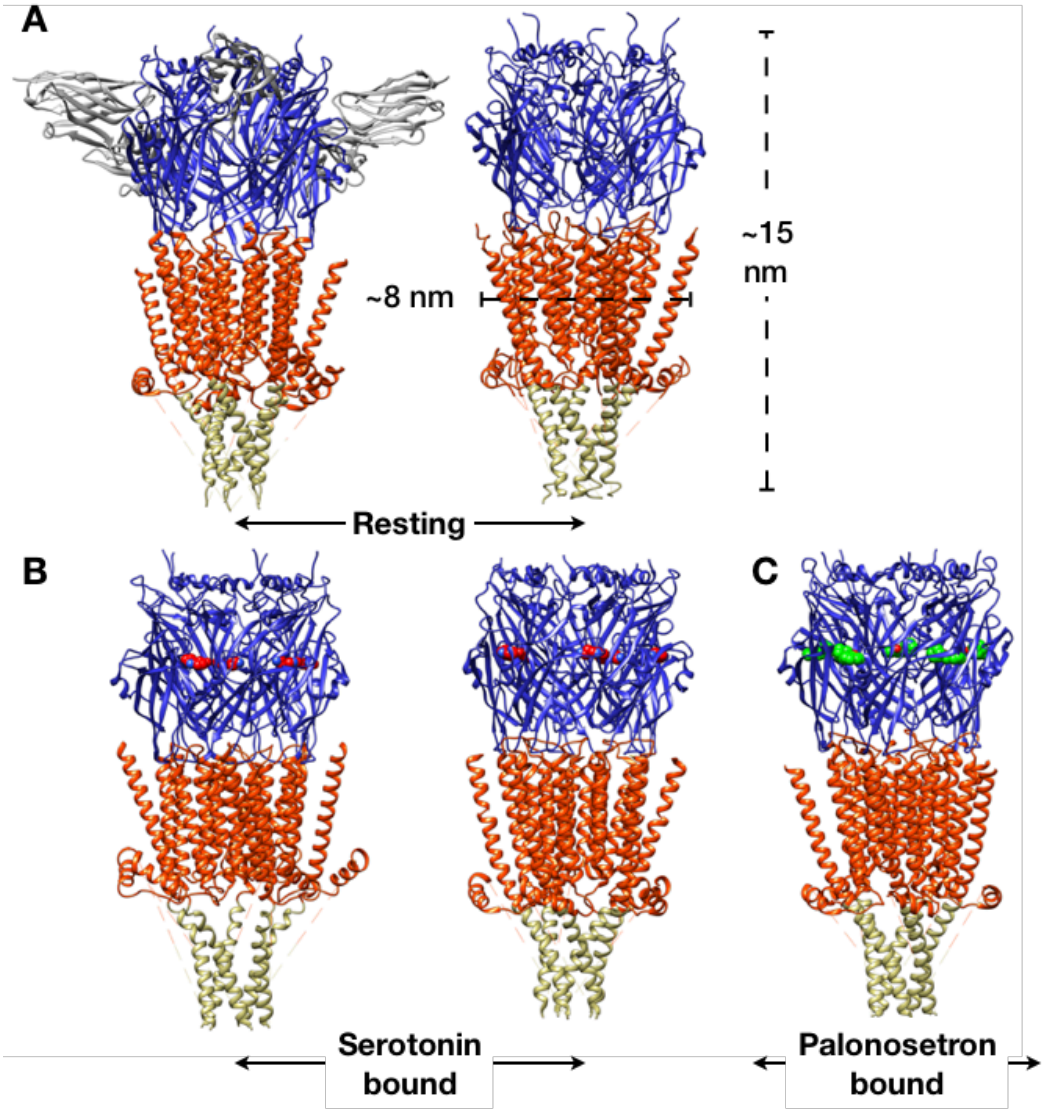

Figure 1.18 Architecture of the $5HT_{3A}R$. (**A**) Resting state. Crystal structure (left, PDB-4PIR) (Hassaine et al., 2014) and cryo-EM structure (right, PDB-6BE1) (Basak et al., 2018b). (**B**) Serotonin-bound state cryo-EM structure (left, PDB-6DG8; right, PDB-6HIQ), serotonin shown in red as sphere (Basak et al., 2018a; Polovinkin et al., 2018). (**C**) Antagonist-bound state cryo-EM structure (PDB-6Y1Z), palonosetron shown in green as sphere (Zarkadas et al., 2020).

Chapter 2 Materials and Methods

2.1 The $5HT_{3A}R$ serotonin receptor single particle analysis

The murine wild-type serotonin $5HT_{3A}R$ receptor was expressed using a stable T-Rex-293 cell line, purified and reconstituted into saposin-lipids nanodiscs, formed Salipro-$5HT_{3A}R$ nanoparticles. The cell line optimization protocol is available from Prof. Dr. Horst Vogel's group (Hassaine et al., 2014). The optimized serotonin receptor expression, purification and reconstitution, including the production of TEV protease and saposin done by Dr. Patricia M. Dijkman., are described following, in this section.

2.1.1 Production of TEV protease

Starter cultures (50 mL LB, 100 µg/mL ampicillin) were inoculated with TEV plasmid-transformed BL21(DE3), and incubated overnight at 37 °C and 200 pm. In 5 L conical flasks, aliquots of 1.25 L 2×YT medium supplemented with 100 µg/mL ampicillin were inoculated with 12.5 mL of starter culture each, and incubated at 37 °C at 120 rpm, usually growing 7.5 L of culture at a time. When the culture reached an OD_{600} of 0.25 the temperature was lowered to 20 °C. Expression was induced at an OD_{600} of 0.6 by addition of IPTG (Sigma-Aldrich) to a final concentration of 0.4 mM, and cells were grown overnight. Cells were harvested by centrifugation (7,000×g, 4 °C, 15 min) and stored at -80 °C or used directly. All purification steps were carried out at 4 ºC or on ice unless stated otherwise. Cell pellet (~40 g) was resuspended in ~3-4-fold volume of TEV sample buffer (50 mM Tris-HCl pH 7.4, 300 mM NaCl). supplemented with protease inhibitors (2 µg/mL leupeptin, 2 µg/mL pepstatin A, 0.2 mg/mL benzamidine-HCl, 20 µg/mL AEBSF, and 3 µg/mL aprotinin). Cells were incubated on ice with DNase I (~1 mg) and lysozyme (1 mg/mL) for 20 min and then lysed using a Microfluidizer processor (Microfluidics M-110L) at 80 psi. Cell debris was separated from lysate by centrifugation (70,000×g, 50 min, 4 °C). Supernatant was filtered through a 0.2 µm syringe filter and imidazole was added to a final concentration of 30 mM, before loading the sample onto a 5 mL HisTrap HP column (GE Healthcare), pre-equilibrated with sample buffer supplemented

with 30 mM imidazole. The sample was washed with ~50 (column volumes) CV of 30 mM imidazole sample buffer and then eluted with an imidazole step gradient of 100 mM for 4 CV, 150 mM for 4 CV, 200 mM for 2 CV, and 350 mM for 6-8 CV. Fractions were analyzed by SDS-PAGE and the cleanest fractions were pooled and concentrated using a Amicon Ultra centrifugal concentrator (10,000 MWCO) and diluted in sample buffer supplemented with 50% glycerol (v/v) to dilute the imidazole concentration below 100 mM. Final TEV concentration was determined by A_{280} (ε_{280} = 32, 290 $M^{-1}cm^{-1}$).

2.1.2 Production of saposin

Saposin A fused to an N-terminal hepta-His tag separated by a TEV protease recognition site (sequence: MHHHHHHHENLYFQSSLPCDICKDVVTAAGDMLKDNATEEEILVYLEKTCDW LPKPNMSASCKEIVDSYLPVILDIIKGEMSRPGEVCSALNLCES) cloned into a pET-21 vector was expressed in Rosetta-gami 2(DE3) *E. coli* cells. Specifically, cells were grown in 5 L flask at 37 ºC, 180 rpm, in TB medium supplemented with 100 µg/mL ampicillin to high density (OD600~2) at which point expression was induced by addition of 0.7 mM IPTG. The temperature was lowered to 30 ºC, and cells were harvest 16 h post-induction. The cell pellet was flash-frozen in liquid nitrogen and stored at -80 ºC until further use. All purification steps were carried out at 4 ºC or on ice unless stated otherwise. Cells were resuspended in lysis buffer (20 mM HEPES, 150 mM NaCl, pH 7.5), supplemented with protease inhibitors, 1 mM MgCl2, 1 mg DNAse I, and 1 mg/mL lysozyme, and subsequently disrupted using a Microfluidizer processor (Microfluidics M-110L) at 80 psi. The cell lysate was clarified by centrifugation (26,000 g, 30 min), and the supernatant was heated at 85 ºC for 10 min in a water bath. The debris was removed by centrifugation (26,000 g, 30 min), and the supernatant was passed through a 0.45 µm-pore filter. Imidazole was added to the filtrate to a final concentration of 20 mM, and the sample was applied at a flow rate of 2 mL/min to a 5 mL HisTrap HP column (GE Healthcare) equilibrated with lysis buffer supplemented with 20 mM imidazole. The column was washed with 25 CV of lysis buffer supplemented with 20 mM imidazole, followed by 25 CV of lysis buffer supplemented with 40 mM imidazole. Saposin was eluted with 10 CV of lysis buffer supplemented with 500 mM imidazole. Peak fractions were pooled and incubated with TEV protease at a 1:1 molar ratio, and the sample was dialysed overnight against dialysis buffer (20 mM HEPES, 300 mM NaCl, pH 7.5) using SnakeSkin dialysis tubing, 3.5 kDa

MWCO (Thermo Fisher Scientific). The sample was filtered, and cleaved saposin was then separated from TEV and any uncleaved material by IMAC on a 1 mL HisTrap HP column (GE Healthcare) equilibrated with dialysis buffer. The flow-through was collected, followed by a 20 mM imidazole wash to remove non-specifically bound cleaved saposin, and a 20-500 mM imidazole gradient over 20 mL to recover any uncleaved saposin and TEV. Fractions were analysed by SDS-PAGE, and fractions corresponding to cleaved saposin were pooled and concentrated to 1-2 mM using an Amicon Ultra centrifugal concentrator (MWCO 3.5 kDa).

2.1.3 Cell culturing, $5HT_{3A}R$ expression, purification and reconstitution in saposin

A stable T-Rex-293 cell line was used for the expression of a murine wild-type 5-HT_{3A} receptor construct containing four N-terminal StrepII tags as previously described (Hassaine et al., 2014). Cells were adapted to serum-free suspension culture in FreeStyle-293 expression medium (Thermo Fisher Scientific) and cultivated at 37 ºC in 1 L flasks under orbital agitation at 120 rpm. Protein expression was induced by adding 4 µg/ml tetracycline when the cell density reached ~$4x10^6$ cells/mL, at which point the temperature was lowered to 30 ºC. Sodium butyrate was added to a final concentration of 6.8 mM 4-6 h post-induction. The typical total culture volume was 4 L. Cells were harvested after 48 h, flash-frozen in liquid nitrogen, and stored at -80 ºC until further use. All purification steps were carried out at 4 ºC or on ice unless stated otherwise. Cells were resuspended in 10 mM HEPES, 1 mM EDTA, pH 7.4, supplemented with protease inhibitors (2 µg/mL leupeptin, 2 µg/mL pepstatin A, 0.2 mg/mL benzamidine-HCl, 20 µg/mL AEBSF, and 3 µg/mL aprotinin) using a dounce homogenizer, and subsequently disrupted using a Microfluidizer processor (Microfluidics M-110L) at 80 psi. Cell debris was removed by centrifugation (10,000 g, 45 min), and membranes were collected from the clarified lysate by ultracentrifugation for 6 h at ~130,000 g. The membrane pellet was flash-frozen in liquid nitrogen, and stored at -80 ºC until further use. The membrane pellet was resuspended in 50 mM Tris, 500mM NaCl, pH 8 (final concentrations). $C_{12}E_9$ (Anatrace) was added dropwise to a final concentration of 0.75% (w/v), and the membranes were solubilised under gentle stirring for 2 h. Non-solubilised material was removed by centrifugation for 1 h at 49,000 g. The supernatant was then passed through a 0.45 µm-pore filter and applied to a 5 mL Streptactin Superflow

high capacity column (IBA), equilibrated with 50 mM Tris, 150 mM NaCl, 0.01% $C_{12}E_9$, pH 8 (Strep buffer), at a flow rate of 1 mL/min. The column was washed with 250 mL of Strep buffer, and the receptor was subsequently eluted with 10 mM D-desthiobiotin in Strep buffer. The peak fractions were pooled and concentrated to 300-500 µL (~10-30 μM) using an Amicon Ultra centrifugal concentrator (MWCO 100,000, Merck). For tests with the sample in detergent, the sample was then filtered through a 0.22 µm-pore centrifugal filter and submitted to size-exclusion chromatography on a Superose 6 Increase 10/300 column (GE Healthcare) equilibrated with 25 mM HEPES, 125 mM NaCl, pH 7.4 (SEC buffer) supplemented with 0.01% $C_{12}E_9$. Alternatively, purified receptor was reconstituted using saposin into porcine brain polar lipid (BPL, Avanti) Salipro-reconstituted-$5HT_{3A}R$ particles. Specifically, BPL was resuspended at 83 mg/mL in 25 mM HEPES, 150 mM NaCl, 5% C12E9, pH 7.4, sonicated 3x1 min in a bath sonicator followed by ten freeze/thaw cycles, and incubation at room temperature for a minimum of 4 h. Purified $5HT_{3A}R$ was incubated for 15 min at room temperature with a 450-fold molar excess of detergent-destabilised BPL, assuming a molecular weight of 650 g/mol for BPL. Saposin was then added to 30-fold molar excess relative to $5HT_{3A}R$, and the sample was incubated 15 min at room temperature. Subsequently, the sample was incubated for 15 min at room temperature with 100-200 mg of wet BioBeads SM2 resin (Bio-Rad), and this last step was repeated once. The sample was then filtered through a 0.22 µm-pore centrifugal filter and submitted to size-exclusion chromatography on a Superose 6 Increase 10/300 column (GE Healthcare) equilibrated with SEC buffer. SEC peak fractions were pooled and concentrated to ~0.5-2.5 mg/mL.

2.1.4 Negative staining analysis

The purified detergent solubilized (0.01% $C_{12}E_9$) serotonin receptor and Salipro-reconstituted-$5HT_{3A}R$ nanoparticles after size exclusion chromatography were collected at several different peak fractions. For initial determination of the homogeneity of different peak fractions of these samples, each fraction was diluted to a final concentration of 0.01 to 0.02 mg/mL (buffer condition – 25 mM HEPES, 125 mM NaCl, pH 7.4, with and without 0.01% $C_{12}E_9$ for detergent-solubilized and membrane-reconstituted samples, respectively) and negatively stained with 2% (w/v) uranyl formate. Negative staining images were collected using a Tecnai Spirit BioTwin transmission electron microscope (Thermo Fisher Scientific) at 120 kV at a nominal magnification of 49,000 x on a Gatan Rio CCD

camera (4k x 4k). For the most homogeneous sample of both detergent-solubilized and membrane-reconstituted $5HT_{3A}R$, a group of images were collected at a defocus around -1.5 µm to -3.5 µm. Contrast transfer function (CTF) estimation was performed with CTFFIND 4.1 (Rohou and Grigorieff, 2015). Particles were auto-picked using Gautomatch-0.53 (Zhang, 2017), and 2D class averages were performed with RELION-2.0 and higher (Scheres, 2012).

2.1.5 Cryo-EM sample preparation and specimen optimization

After negative-stain screening, the most homogenous fractions of Salipro-$5HT_{3A}R$ were pooled and concentrated to around 0.43 mg/mL. Grids were prepared in the presence and absence of serotonin for Salipro-5HT-activated state and Salipro-resting state, accordingly. For the Salipro-activated state, the Salipro-$5HT_{3A}R$ was mixed with 100 µM serotonin and 2 mM $CaCl_2$, and incubated on ice for 45-60 minutes. To optimize the ice thickness and particle distribution of the cryo-EM specimen, a set of grids were prepared in advance, including normal and amorphous carbon-back-coated QUANTIFOIL® Holey Cu-carbon-R2/2, Au-carbon-R2/2, UltraAuFoil grid, and C-flat™ Holey Cu-carbon R2/2 grids. Besides, cryo-EM specimens were also prepared with and without adding of CHAPS. Three µl of concentrated Salipro-$5HT_{3A}R$ was applied onto freshly plasma-cleaned (NanoClean, model 1070, Fischione Instruments) grids, and then plunge-frozen into liquid ethane using a Mark IV Vitrobot device (Thermo Fisher Scientific). For normal grids, plasma cleaning was performed with argon/oxygen (Ar/O_2) atmosphere, ratio of 95/5, at 35 W for 2 minutes. And for carbon-back-coated grids, time was limited up to 35 seconds on the opposite of carbon-coated side. The cryo-EM specimens prepared on different grids with and without CHAPS were screened; final datasets were collected from the cryo-EM grids prepared with CHAPS for its thinner uniform ice thickness and good particles orientation distribution.

2.1.6 Cryo-EM single particle data collection

The datasets of both Salipro-5HT-activated and Salipro-Apo states were collected on a Titan Krios cryogenic transmission electron microscope (Thermo Fisher Scientific) at 300 kV with a Falcon III direct detector device at a nominal magnification of 96,000 x yielding a pixel size at the specimen of 0.832 Å in counted mode. Movies were collected with EPU, a data collecting automation software package (Thermo Fisher Scientific), with an imaging setting of total exposure equals to 30 electrons over 69 frames, and a defocus range between -1.6 µm to -2.6 µm at the Max Planck Institute of Biophysics. For the Salipro-Apo state, two datasets were collected on different dates from the same grid using the same imaging settings. Additional data collection details are given in **Table 2.1**.

Table 2.1 Details of cryo-EM single particle data collection and model validation.

	5-HT	***Apo (C5)***	***Apo (C1)***
		Data collection and processing	
Microscope	Titan Krios	Titan Krios	
Magnification	96,000	96,000	
Voltage (kV)	300	300	
Detector	Falcon III	Falcon III	
Electron exposure (e-/Å^2)	30	30	
Number of frames/movie	69	69	
Defocus range (μ)	-1.6 to -2.6	-1.6 to -2.6	
Pixel size (Å)	0.832	0.832	
Symmetry imposed	C1	C5	C1
Number of images	2,261*	5,028*	
Particles extracted (total)	642k	3.2M	
Particles refined (final)	251,610	238,701	152,877
Resolution unmasked (Å)	3.13	3.50	3.46
Resolution masked (Å)	2.77	3.17	3.10
FSC threshold	0.143	0.143	0.143
		Model vs Map cross validation (Å)	
Model vs Half map (work)	3.3	4.1	3.9
Model vs whole map	3.2	4.0	3.7
FSC threshold	0.5	0.5	0.5
			Validation
Ramachandran Plot Favored (%)	95.73	98.78	98.06
Allowed (%)	4.27	1.22	1.94
Disallowed (%)	0	0	0
Molprobity score	1.41 (100^{th} percentile)	0.99 (100^{th} percentile)	1.16 (100^{th} percentile)
Molprobity clashscore	3.27 (100^{th} percentile)	2.19 (100^{th} percentile)	3.69 (100^{th} percentile)
Poor rotamers (%)	0	0	0

*(*Two datasets were collected on different dates for Salipro-Apo state on the same grid with the same settings, and subsequently merged.)*

2.1.7 Image processing

During data collection, all datasets were pre-processed “on-the-fly” using Warp (Tegunov and Cramer, 2019) for movie motion correction, CTF estimation, and automatic particle picking. The auto-picked particles were imported into cryoSPARC (Punjani et al., 2017) for 2D classification, in order to monitor data quality including particle orientation and integrity. Warp also excluded poor micrographs during “on-the-fly” processing (25 for Salipro-Apo state, none for Salipro-5HT-activated state) including poor ice quality, out-of-range focused, large drifting detected and little particle picked. Finishing data collection, all the subsequent data were imported into RELION-3.0 (Zivanov et al., 2019). Drift correction and dose weighting were performed using MotionCor2 (Zheng et al., 2017) with a 5 x 5 patch. CTF determination was performed using CTFFIND4.1 (Rohou and Grigorieff, 2015) and Gctf-v1.06 (Zhang, 2016) for Salipro-Apo dataset and Salipro-5HT-activated dataset, respectively. Particle picking was performed with crYOLO (Wagner et al., 2019) and Warp for Salipro-Apo dataset and Salipro-5HT-activated dataset, respectively. Auto-picked particles were extracted with a box size of 320 pixels, and imported into cryoSPARC to perform particle cleaning using 2D classification (multi-rounds if necessary) and 3D heterogeneous refinement (3D classification) with C5 symmetry (3D heterogeneous refinement was attempted both with C1 and C5 symmetry, and the latter resulting in better separation of the particles). The most homogenous particle sets after cleaning and separation, were taken to perform 3D homogeneous refinement. The output file, as a result of the selected most homogeneous particle set, was taken to generate a star file using Pyem (Asarnow et al., 2019) and imported back into RELION-3.0. Particles were further 3D classified without alignment and without imposing symmetry in RELION-3.0. Most of the particles fell into one class. For the Salipro-Apo state, with the above processing, the datasets yielding both symmetric (C5) and asymmetric (C1) maps, and for the Salipro-5HT-activated state, the datasets only generated one asymmetric (C1) map. To assess the reliability of the (a)symmetry of our final maps, symmetry expansion was performed along the C5-pseudo symmetric axis, then 3D classification without alignment into 12 (for Salipro-Apo state) or 16 (for Salipro-5HT-activated state) classes using a loose monomer mask was performed. At the obtained resolution, the differences between classes obtained for the Salipro-Apo-C5 dataset was negligible. While for Salipro-Apo-C1 and Salipro-5HT-activated datasets, obvious differences between classes could be found. Therefore, the three different consensus datasets of the three maps (Salipro-Apo-C5, Salipro-Apo-C1 and Salipro-5HT-actIvated) were then

subjected to several rounds of polishing, CTF refinement and 3D refinement with C5 symmetry imposed (for Salipro-Apo-C5) or without symmetry imposed (for Salipro-Apo-C1 and Salipro-5HT-activated). Local resolution was estimated in RELION-3.0, and global directional resolution estimation was performed using 3DFSC (Tan et al., 2017). A detailed image processing pipeline shown in **Figure 2.1**.

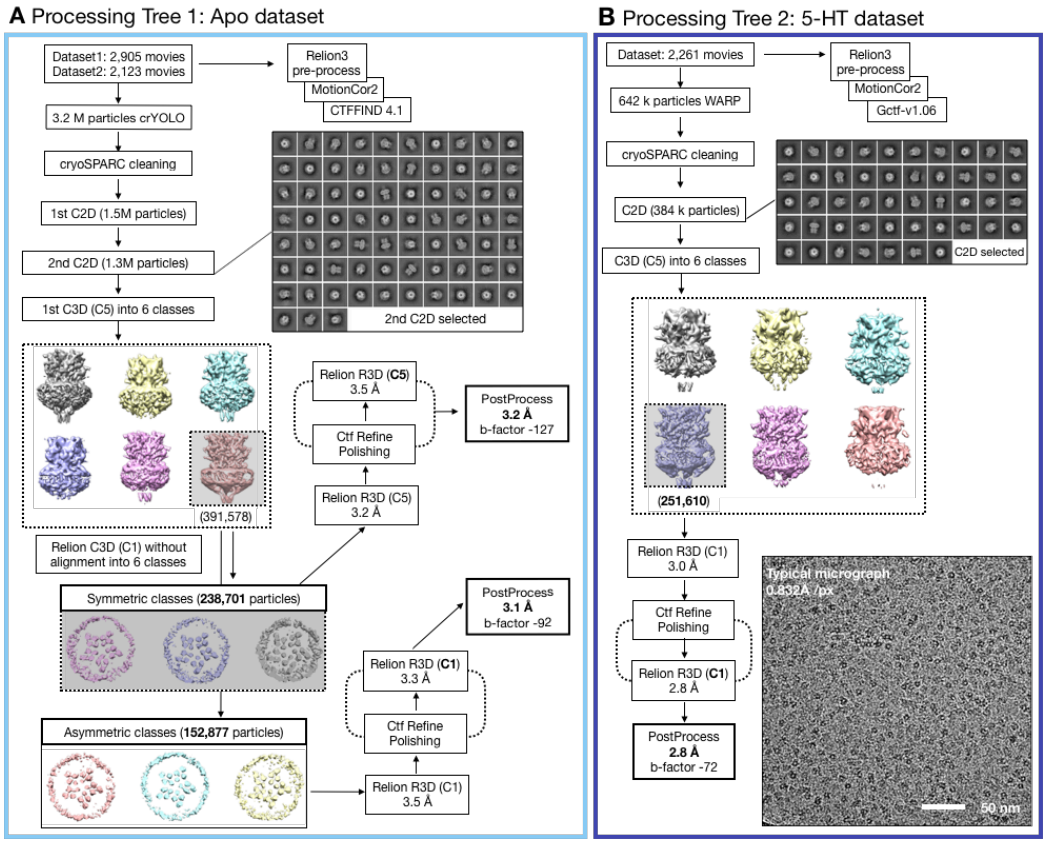

Figure 2.1 $5HT_{3A}R$-Salipro cryo-EM data processing workflow. There cryo-EM structures were resolved with the two datasets collected for $5HT_{3A}R$-Salipro-Apo and $5HT_{3A}R$-Salipro-5HT states.

2.1.8 Model building and analysis

The initial model for Salipro-5HT-activated state was built manually in COOT (Emsley et al., 2010) with secondary structure prediction from PSIPRED (Buchan and Jones, 2019) and the guidance from the published murine serotonin X-ray structure (PDB-4PIR). EM map sharpness was performed using RELION-3.0 with automatic b-factor estimated. PHENIX (Adams et al., 2002) was used for model refinement, and the model was validated with Molprobity (Chen et al., 2010). The refined model was then used for local-sharpening of the RELION refined EM map using LocScale (Jakobi et al., 2017). The LocScale sharpened EM map was subsequently used for further iterative refinement in COOT and PHENIX. The Salipro-Apo models (C5 and C1) were built with the same method as described for the Salipro-5HT-actvated model. The final models built were then taken to generate density maps from all their specified atoms using UCSF Chimera (Pettersen et al., 2004) at a resolution of 2 Å, for performing model to map cross validation using RELION-3.0. At the extracellular domain (ECD), resolved densities corresponding to the N-linked glycosylation adjacent to N82, N148 and N164 were not modelled. Static pore radius profiles of the models were determined using HOLE programme (Smart et al., 1996) and visualized in VMD (Humphrey et al., 1996). CASTp (Tian et al., 2018) was used to calculate the volume of the inter-subunit cavity. Structural figures were prepared using UCSF Chimera and VMD. A detailed model validation is listed in **Table 2.1**.

2.1.9 Molecular dynamics simulations

The molecular dynamics (MD) simulations and lipid order calculation were performed with collaboration by Dr. Rongfeng Zou and Dr. Shuguang Yuan at the Chinese Academy of Sciences. Experimental details are as following.

All protein models were prepared using the Schrödinger software suite under the OPLS_2005 force field (Shivakumar et al., 2010). Hydrogen atoms were added to the repaired cryo-EM structures at physiological pH (7.4) with the PROPKA (Søndergaard et al., 2011) tool to optimise the hydrogen bond network provided by the Protein Preparation tool in Schrödinger. Constrained energy minimisations were carried out on the full-atomic models, until the RMSD of the heavy atoms converged to 0.4 Å. All liganded receptor structures were prepared using the Schrödinger 2015 software suite; the LigPrep module was used for geometric optimisation applying the OPLS_2005 force field. The ionisation state of ligands

was calculated with the Epik (Greenwood et al., 2010) tool employing the Hammett and Taft methods in combination with ionisation and automatization tools (Greenwood et al., 2010).

Membrane systems were built using the membrane building tool CHARMM-GUI (Jo et al., 2008) with the experimental structures pre-aligned in the OPM (Orientations of Proteins in Membranes) database (Lomize et al., 2011). To mimic the lipid composition of BPL, we used POPC (1-palmitoyl-2-oleoyl-glycero-3-phosphocholine), POPS (1-palmitoyl-2-oleoyl-sn-glycero-3-phospho-L-serine), POPE (1-palmitoyl-2-oleoyl-sn-glycero-3-phosphoethanolamine), and cholesterol at a molar ratio of 15:22:39:24. The simulation system contains a total of 300 lipids for both apo- and 5HT-bound Salipro-$5HT_{3A}R$. For the simulations of the 6DG8 structure, we included 244 POPC lipids to mimic the detergent environment used in the original work. In addition, 0.15 M NaCl was added to each simulated system. We modelled the protein, lipids, water and ions using the CHARMM36m force field (Klauda et al., 2010). Ligands were assigned with CHARMM CgenFF force field (Vanommeslaeghe et al., 2012). Ligand geometry was submitted to ORCA (Neese, 2012) for optimisation at the Hartree-Fock 6-31G* level when generating force field parameters. The system was gradually heated from 0 K to 310 K followed by a 1 ns initial equilibration at constant volume with the temperature set at 310 K. The protein backbone and heavy atoms of the ligands were restrained during the equilibration steps with a force constant of 3 kcal/(mol.$Å^2$), after which restraints were released and a further 200 ns of simulation was run. Simulations were run in triplicate and the last 50 ns were used for analysis. All bond lengths to hydrogen atoms were constrained with M-SHAKE. Non-bonded interactions were treated using the force switch of 10-12 Å. Long-range electrostatic interactions were computed by the Particle Mesh Ewald (PME) summation scheme. All MD simulations were done in GROMACS (Pronk et al., 2013). The simulation parameter files were obtained from CHARMM-GUI website (Jo et al., 2008). The radius profiles of M2 based on MD simulations were analysed using CHAP (Klesse et al., 2019).

2.1.10 Lipid order calculation

The lipid order parameter ($-S_{CD}$) for the different lipid species present in the MD trajectories was calculated by the MEMBPLUGIN tool in VMD (Guixà-González et al., 2014). $-S_{CD}$ is the carbon deuterium order parameter which is typically derived from NMR experiments. This parameter quantifies the order of

phospholipid hydrocarbon tails by averaging (ensemble and time) the angle Θ, per C-H bond with respect to the bilayer normal, z -axis, independently for every methyl group in each lipid acyl tail over a given lipid moiety in the membrane. The membrane order parameter is expressed as follows (Schindler and Seelig, 1975):

$$-S_{CD} = -\frac{1}{2}(3 < cos^2\Theta > -1)$$

where Θ is the instantaneous angle between the C-H bond and the bilayer normal and the angular brackets < > indicate time and ensemble average.

2.1.11 Thermo-stability and microscale thermophoresis characterization

Thermal stability of serotonin receptor in detergent and reconstituted into Saposin-lipid-nanoparticles were determined using nanoDSF (Magnusson et al., 2019), and serotonin binding affinity was assessed using microscale thermophoresis (MST) (Jerabek-Willemsen et al., 2014) by Dr. Patricia M. Dijkman.

The thermal stability of the receptor in detergent and reconstituted into BPL Salipro particles, respectively, was determined using nanoDSF on a Prometheus NT.48 instrument (NanoTemper Technologies). Samples obtained after size-exclusion chromatography were diluted to 0.20-0.25 mg/mL and loaded into nanoDSF grade standard capillaries (NanoTemper Technologies). Samples were heated from 15 to 95 ºC at 1 ºC/min, and the ratio between intrinsic fluorescence at λ=330 and 350 nm after excitation at λ=280 nm was used to monitor receptor denaturation. The first derivative of the unfolding curves was used to determine the transition midpoint using PR.ThermControl software (NanoTemper Technologies).

The affinity of Salipro-5HT$_{3A}$R for serotonin was assessed by microscale thermophoresis (MST). Salipro-5HT$_{3A}$R was labelled with NT-647-NHS dye (NanoTemper Technologies) as per the manufacturer's instructions. Labelled receptor (final concentration 9.5 nM) was added to a dilution series of 5-HT 0.3 nM-11 µM (final concentrations) in 25 mM HEPES, 150 mM NaCl, pH 7.4, supplemented with 0.007% (w/v) Tween-20 (final concentration) using LoBind tubes (Eppendorf) to prevent adsorption of the sample. Under these conditions, the fluorescence was found to be constant (within±10%) for all points in the

titration curve. The samples were loaded into premium coated capillaries (NanoTemper Technologies). Microscale thermophoresis experiments were carried out on a blue/red Monolith NT.115 (NanoTemper Technologies) using the red filter set, an excitation power of 100%, and an MST power of 60%. MST data were analysed in MO.Affinity Analysis software (NanoTemper Technologies), using -1 s to 0 s before IR laser was turned on as the cold region, and 20 to 21 s after the IR laser was turned on as the hot region.

2.1.12 Lipidomics

Lipidomics experiments were performed with collaboration by Dr. Martina Zandl-Lang and Dr. Harald Köfeler at the Medical University of Graz, Austria.

Three biological replicates of Salipro-5HT_{3A}R (~1 nmol final) were prepared as described above. The gel filtration peak at ~17 mL corresponding to saposin discs without the receptor inserted (empty discs) were also collected for each biological repeat. Lipids were extracted by a methyl-tert-butyl ether (MTBE) protocol as previously described (Matyash et al., 2008). Briefly, the samples were extracted in methanol/MTBE/water and the organic phase was dried, resuspended in 300 µL methanol:chloroform 1:1 and 12:0/13:0 PC, 17:0/20:4 PC, 14:1/17:0 PC, 21:0/22:6 PC (2 μM each), 17:1 LPC (1.5 µM), Cer/Sph-Mix LM6002 (1.5 µM), 12:0/13:0 PE, 17:0/20:4 PE, 14:1/17:0 PE, 21:0/22:6 PE (3 µM each), 12:0/13:0 PS, 17:0/20:4 PS, 14:1/17:0 PS, 21:0/22:6 PS (3 µM each), 12:0/13:0 PI, 17:0/20:4 PI, 14:1/17:0 PI and 21:0/22:6 PI (2 µM each) were added as internal standard (all lipid species are quantitative LM standards from Avanti Polar Lipids). All of the extracts were again dried and resuspended in 50 µL isopropanol:chloroform:methanol (90:5:5 v/v/v). Data acquisition was performed on a Q Exactive Focus Orbitrap instrument (Thermo Scientific) coupled to a Vanquish UHPLC (Thermo Scientific) according to previously published protocols (Fauland et al., 2011; Triebl et al., 2017). Briefly, chromatographic separation was performed on a BEH C8 column (100 × 1 mm, 1.7 µm, Waters, Milford, MA, USA), thermostated to 50 °C. Mobile phase A was deionised water containing 1 vol% of 1 M aqueous ammonium formate (final concentration 10 mM) and 0.1 vol% of formic acid as additives. Mobile Phase B was a mixture of acetonitrile/isopropanol 5:2 (v/v) with the same additives. Gradient elution started at 50 % mobile phase B, rising to 100 % B over 40 minutes; 100 % B was held for 10 minutes and the column was re-equilibrated with 50 % B for 8 minutes before the next injection. The flow rate was 150 µL/min, the samples were kept at 8 °C and the injection

volume was 2 µL. The mass spectrometer was operated in Data Dependent Acquisition mode using a HESI II ion source. Every sample was measured once in positive polarity and once in negative polarity. Samples were measured in positive electrospray mode at 4.5-kV source voltage, 275 °C source temperature, and 300 °C capillary temperature in full scan (mass/ charge ratio (m/z), 160 to 1.150). In negative electrospray mode, the source voltage was at 3.8 kV, the source temperature was at 325 °C, and the capillary temperature was at 300 °C in full scan (m/z 300 to 1.100). Full scan profile spectra were acquired in the Orbitrap mass analyser at a resolution setting of 70 000 at m/z 200. For MS/MS experiments, the 3 most abundant ions and ions from the inclusion list (data dependent fragmentation mode) of the full scan spectrum were sequentially fragmented. Data analysis was performed by Lipid Data Analyzer, a custom developed software tool described in more detail by Hartler and colleagues (Hartler et al., 2017; Hartler et al., 2011) and with the added internal standards as a one-point calibration and normalised to total protein amount.

2.2 Conventional cryo-ET and STA of 5-HT_{3A}R serotonin receptor micro-vesicles

The cell-derived serotonin receptor micro-vesicles ($5HT_{3A}$R-MVs) were prepared by Dr. Catarina Alves from cell culture supernatant, following the approach to Pick et al, 2005 (Pick et al., 2005) with modifications. The cell pellet after centrifugation was discarded and supernatant was collected and underwent ultracentrifugation at 23,000 g for 30 minutes. The subsequent collected pellet was corresponded to $5HT_{3A}$R-MVs and was hydrated with 500 µL PBS overnight. The $5HT_{3A}$R-MVs suspension was then added to a centrifuge tube for a Swinging Bucket rotor. And 20% sucrose cushion in PBS was gently added with a syringe and 18 G needle to the bottom of the tube in a volume ration of 1:4. The tube was carefully placed in the rotor support and underwent ultracentrifugation at 100,000 g for 1 hour 10 minutes. The supernatant was discarded after ultracentrifugation and leftover sample was hydrated and resuspended with PBS overnight. Possible glucose contamination could be removed with another ultracentrifugation step (at 100,000 g for 1 hour 10 minutes). Supernatant was discarded and sample was hydrated and resuspended with 100 to 200 µL PBS overnight. An optimized protocol is available from Dr. Horst Vogel's group.

2.2.1 EM specimen preparation for cryo-ET

The re-suspended $5HT_{3A}$R-MVs specimen was mixed and homogenized with 10 nm Protein-A gold nanoparticles as fiducial markers (Cell Microscopy Core, Netherlands, UMC Utrecht) in a volume ratio of 2:1, right before plunge-freezing. 3.5 µL of sample mixed with gold fiducial markers was then applied on a twice glow discharged (PELCO easiGlow™ Glow Discharge Cleaning System) Quantifoil Au-carbon R1.2/1.3 300-mesh grid, blotted using a Mark IV Vitrobot (Thermo Fisher Scientific), and plunge-frozen in liquid ethane. Grids were stored in liquid nitrogen until data collection.

2.2.2 Cryo-ET data collection

The tomograms of $5HT_{3A}$R-MVs were recorded using a first generation FEI Titan Krios (Thermo Fisher Scientific) operated at 300 kV, with the EM specimen maintained at liquid nitrogen temperatures. Tomograms were acquired at a nominal magnification of 64,000 x (2.2 Å/pixel at counted mode; 1.1 Å/pixel at super-resolution mode) using SerialEM (Mastronarde, 2005) with the dose-symmetric script (Hagen et al., 2017) and the hybrid variant (Appendix I). Movie stacks with 0.3-0.4 $e^-/Å^2$ per frame (1.5-2 $e^-/Å^2$ per 2D projection) were recorded on a post-GIF K2 Summit direct electron detector (Gatan, Inc.) in super-resolution mode. The total electron dose for both the conventional dose-symmetric and hybrid tomograms was kept the same, ~100 $e^-/Å^2$. The conventional tomograms had the total dose equally distributed over 41 tilt projections, from -60° to 60° with a tilting increment of 3°. The hybrid tomograms had their untilted (0°) 2D projections with a total dose of 15-20 $e^-/Å^2$, and with the remaining dose equally distributed over the remaining 40 tilted 2D projections over the same angular range.

2.2.3 Tomographic processing and conventional subtomogram averaging

Each tilt projection was aligned using MotionCor2 (Zheng *et al*, 2017); and the average defocus was determined using Gctf-1.0.6 (Zhang, 2016). The aligned projections were assembled into stacks and aligned using gold fiducial markers in IMOD-4.10 (Kremer et al., 1996), and the resulting aligned tilt-stacks were CTF-corrected using *ctfphasefilp* from IMOD (Xiong et al., 2009). The generated CTF-corrected reconstructions were used for particle sub-boxing using the Dynamo catalogue tools (Castano-Diez et al., 2017). The vesicle surface models were manually created in Dynamo-1.133 (and higher), and sub-volumes were cropped using Dynamo. Particle orientations adapted the vectors at the coordinates perpendicular to the defined vesicle surfaces, cropping separation with user-justified step in pixel. Manually picking was involved in some of the tomograms where the protein insertion was found non-uniform.

Subtomogram averaging was performed using sub-volumes cropped on bin4 tomograms (4.4 Å/pixel) with sub-boxing size of 80 in Dynamo version 1.133 (and higher) (Castano-Diez et al., 2012).

2.3 Hybrid SPA-STA tomographic workflow

2.3.1 EM specimen preparation for cryo-ET

The TMV specimen, 33 mg/mL, was gently mixed with 10 nm protein-A gold nanoparticles as fiducial markers (Cell Microscopy Core, Netherlands, UMC Utrecht), with a volume ratio of 1 to 0.8, immediately before plunge-freezing. 3 µL of sample mixed with gold fiducials markers was then applied on a twice glow discharged (PELCO easiGlow^{TM} Glow Discharge Cleaning System) Quantifoil Au-carbon R1.2/1.3 300-mesh grid, blotted using a Mark IV Vitrobot (Thermo Fisher Scientific), and plunge-frozen in liquid ethane. Grids were stored in liquid nitrogen until data collection.

2.3.2 Cryo-ET data collection

TMV tomograms were recorded using two transmission electron microscopes, a first generation FEI Titan Krios and an FEI Titan Krios G2 (Thermo Fisher Scientific) operated at 300 kV, with the specimen maintained at liquid nitrogen temperatures. Tomograms were acquired at a nominal magnification of 64,000x (2.2 Å/pixel in counted mode) using SerialEM (Mastronarde, 2005) with the dose-symmetric script (Hagen et al., 2017) and the hybrid variant (Appendix I). The 2D projection movie stacks with 0.3 $e^-/Å^2$ per frame (1.5-1.8 $e^-/Å^2$ per projection) were recorded on a post-GIF K2 Summit direct electron detector (Gatan, Inc.) in super-resolution mode. The total electron dose for both the conventional dose-symmetric and hybrid tomograms was kept the same, ~95 $e^-/Å^2$. The conventional tomograms had the total dose equally distributed over 41 tilt images, from -60° to 60° with a tilting increment of 3°. The hybrid tomograms had their untilted 2D projections with a total dose of 15-20 $e^-/Å^2$, with the remaining dose equally distributed over the remaining 40 tilted images over the same angular range.

2.3.3 Tomographic processing and hybrid subtomogram averaging

For the conventional data processing, each tilted 2D projection was aligned using MotionCor2 (Zheng *et al*, 2017); and the average defocus was determined using CTFFIND4 (Rohou & Grigorieff, 2015) or Gctf-1.0.6 (Zhang, 2016). The aligned projections were assembled into stacks and aligned using gold fiducial markers in IMOD-4.10 (Kremer et al., 1996), and the resulting aligned tilt stacks were CTF-corrected using *ctfphasefilp* from IMOD (Xiong et al., 2009). The generated CTF-corrected reconstructions were used for particle picking using the Dynamo catalogue tools (Castano-Diez et al., 2017). Subtomogram averaging was performed using Dynamo-1.133 (and higher) (Castano-Diez et al., 2012). For TMV, two independent half sets were generated by assigning different filaments into different sets, these sets were processed independently.

For the hybrid datasets processing, in the step of tilting stack creation, all the motion-corrected 2D projections were normalized to have the same mean value of 128 and standard deviation of ~11. The higher dose untilted projections for all tomograms had a mean value of 128 and standard deviation of ~4, which was 2.7 times lower, according to the relation,

$$(\sigma_{HD})^2 / (\sigma_{LD})^2 = e^-_{LD} / e^-_{HD}$$

The generated tilt-stacks were processed according to the conventional STA processing workflow described above. After the conventional processing, the data was exported to RELION-3.0 using a Matlab script, *dyn2rel*, written by Ricardo Sanchez, available from Dr. Kudryashev's lab, detailed description in the preprinted manuscript (Sanchez et al., 2020). Local refinements were running with *relion_refine* refinement command for two independent half-sets in RELION-3.0 (Zivanov et al., 2019). Refined parameters for helical symmetry are helical twist 22.033 degree and rise 1.41 Å. The detailed description is in Sanchez & Zhang, et al., submitted.

Chapter 3 Results

In this chapter, experimental results of the serotonin receptor $5HT_{3A}R$ in the presence of lipid bilayers are described in Section 3.1 to 3.5. It includes biochemical and biophysical characterization of the receptor in lipid bilayers, structural characterization of the receptor, analysis of the functional states of the resulting atomic models. After that, an approach to characterize the receptor in natively derived vesicles without the need of protein purification is discussed in Section 3.6. Following that, a method development aiming at higher resolution for cryo-ET and STA are described in Section 3.7.

3.1 $5HT_{3A}R$-Salipro: negative staining and serotonin binding affinity determination

In order to provide the physiologically important lipid bilayers, we firstly reconstituted the full-length murine homopentameric $5HT_{3A}R$ with BPL, forming the saposin-lipoprotein nanoparticles ($5HT_{3A}R$-Salipro) (Flayhan et al., 2018; Frauenfeld et al., 2016) for further specimen stability estimation and structural characterization. The homogeneity of the purified $5HT_{3A}R$ before and after reconstituted into Salipro were confirmed by negative staining (NS) (**Figure 3.1**). Negative staining on both detergent-solubilized and membrane-embedded $5HT_{3A}R$ show nice homogenous domain features of $5HT_{3A}R$ (**Figure 3.2** B).

Besides, the measurements of the apparent melting temperature done by Dr. Patricia. M. Dijkman suggested $5HT_{3A}R$-Salipro was more stable then $5HT_{3A}R$ in detergent ($5HT_{3A}R$-Detergent), T_m=67 °C and 61 °C respectively (**Figure 3.1** C), which is in an agreement with the previous study showing that lipids stabilized the receptor (Tol et al., 2013).

And the $5HT_{3A}R$-Salipro binding affinity of serotonin was then determined using microscale thermophoresis (MST). The results suggested a serotonin binding affinity of $5HT_{3A}R$-Salipro at a level around 300±90 nM and 80±40 nM in the absence and presence of 2 mM calcium chloride ($CaCl_2$) accordingly (**Figure 3.1** D), which agreed well with literature for membrane-inserted serotonin receptor (Hovius et al., 1998; Yan et al., 1999), suggesting the binding affinity of serotonin for membrane-embedded $5HT_{3A}R$ is in a range around 10^{-7} M.

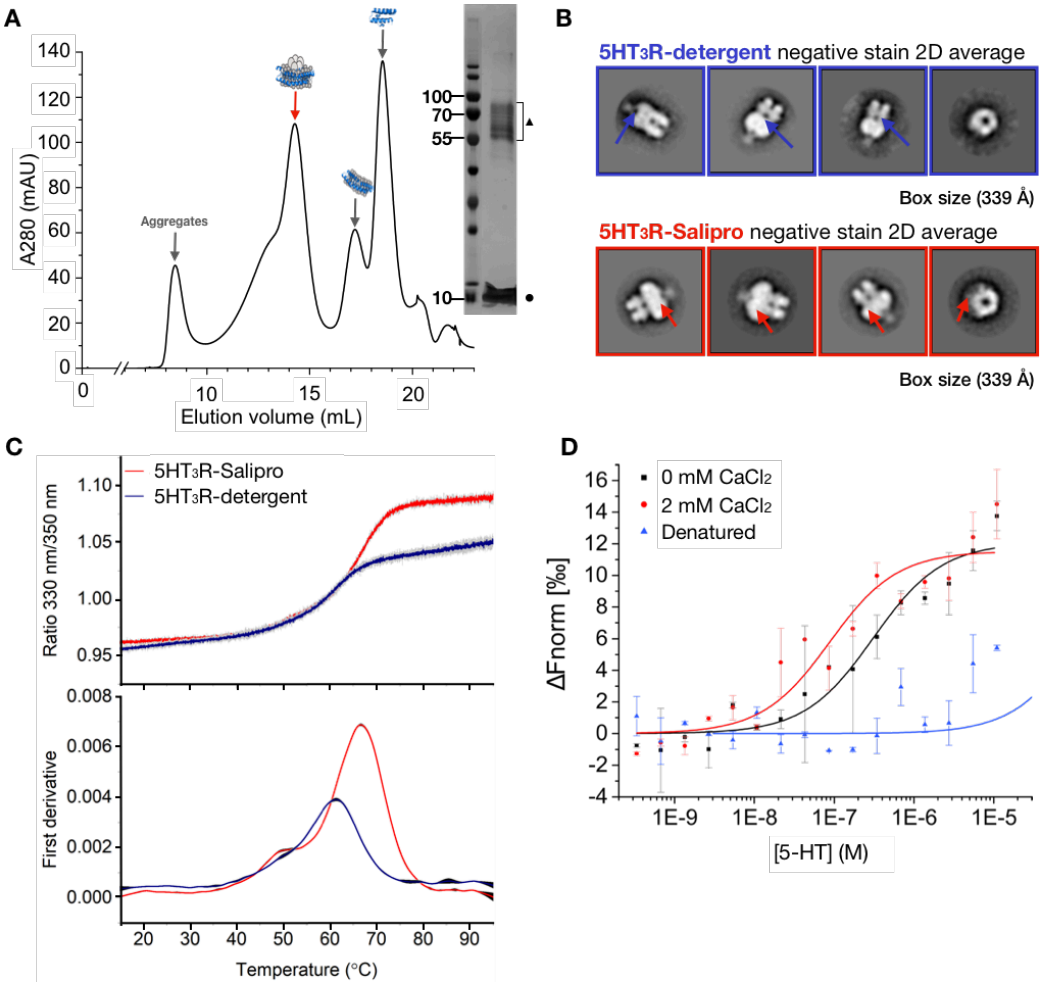

Figure 3.1 Characterizations of $5HT_{3A}R$-Salipro. (**A**) Gel filtration chromatogram and SDS-PAGE gel for the Salipro-reconstituted $5HT_{3A}R$ (saposin, solid sphere and $5HT_{3A}R$-Salipro, solid triangle). (**B**) Negative staining 2D average classes of $C_{12}E_9$-solubilized (top) and Salipro-reconstituted (bottom) $5HT_{3A}R$. Arrows indicate detergent micelle (blue) and salipro-lipid belt (red). (**C**) NanoDSF measurements of thermal stability for $5HT_{3A}R$-Salipro (red, apparent T_m=67 ºC) and detergent-solubilized $5HT_{3A}R$ (dark-blue, apparent T_m=61ºC). Grey shading represents SD with n=2. (**D**) Affinity of $5HT_{3A}R$-Salipro in BPL determined by microscale thermophoresis (MST), K_d=300±90 nM in absence (black) and 80±40 nM in presence (red) of 2 mM $CaCl_2$. Denatured $5HT_{3A}R$-Salipro (blue) as a negative control showed no significant ligand binding. Error bars represent SD with n=2.

3.2 $5HT_{3A}$R-Salipro architecture: cryo-EM SPA structural analysis

Cryo-electron microscopy single particle analysis (cryo-EM SPA) was applied for structural determination of serotonin receptor ($5HT_{3A}$R) reconstituted in saposin-lipid discs. The EM structures of the $5HT_{3A}$R-Salipro in its different conformations (two Apo states and one serotonin-bound state) were resolved at high resolution with and without the presence of its native agonist - serotonin.

The EM density maps shew clearly all components of $5HT_{3A}$R-Salipro, including the full length serotonin receptor itself, the glycosylation, the saposin-lipid belt and some well-defined densities considered to be as cholesterol and phospholipids moieties (**Figure 3.2** A). The atomic models for each conformation were built accordingly and described directly their great differences of the pore radium by comparison to the models of $5HT_{3A}$R-Detergent serotonin bound conformation (Basak et al., 2018a) (**Figure 3.2** B, C).

The estimated resolution and model validation for each $5HT_{3A}$R-Salipro state is shown in **Figure 3.3**, describing the nominal resolution of the three different conformations are 3.2 Å of symmetric (C5) $5HT_{3A}$R-Salipro-Apo, asymmetric (C1) 3.1 Å of $5HT_{3A}$R-Salipro-Apo, and 2.8 Å of asymmetric (C1) $5HT_{3A}$R-Salipro-5HT state. Their map quality of each conformation is shown in **Figure 3.4**.

Unbiased Molecular dynamic (MD) simulations, performed in the collaboration with Dr. Yuan and Dr. Zou, further proved the serotonin bound $5HT_{3A}$R-Salipro conformation stayed stable in lipids and was conductive allowing free ion permeation, with an average pore diameter of ~10 Å along the transmembrane domain (TMD), that we will discuss later in this section.

Beside, each conformational state of the $5HT_{3A}$R-Salipro is compared in great details to the reported $5HT_{3A}$R-Detergent forms by Basak and colleagues, PDB-6BE1 and 6DG8 (Basak et al., 2018a; Basak et al., 2018b).

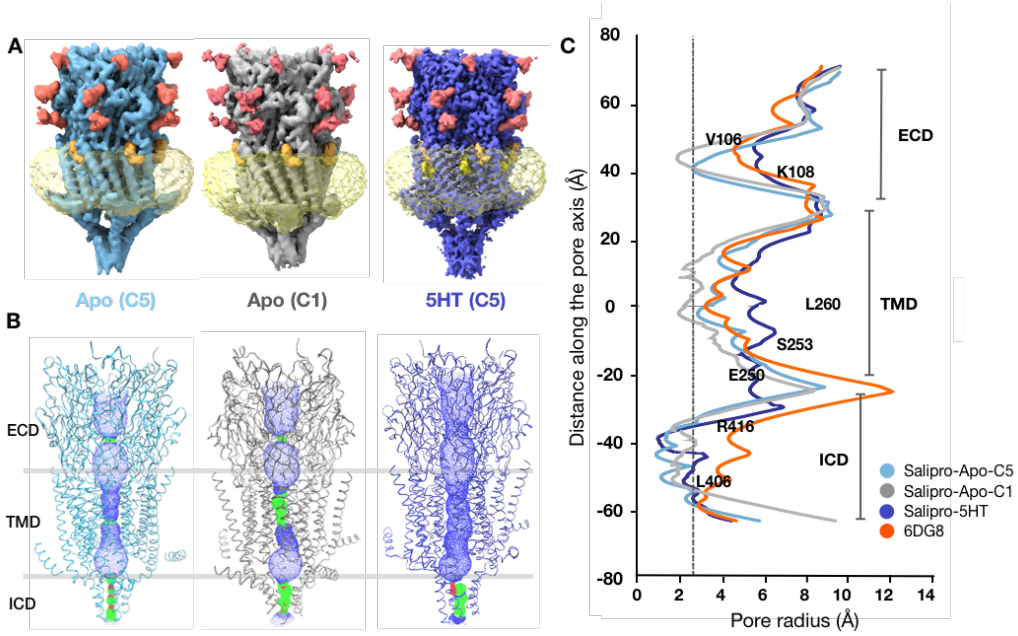

Figure 3.2 Cryo-EM revealed three $5HT_{3A}R$-Salipro conformations. (**A**) Cryo-EM density maps of $5HT_{3A}R$-Salipro-Apo (C5 symmetric, light-blue; C1 symmetric, grey) and $5HT_{3A}R$-Salipro-5HT (5-HT, dark-blue), with red, orange, yellow (only in $5HT_{3A}R$-Salipro-5HT) and transparent-yellow densities corresponding to glycosylation, cholesterol, inter-subunit phospholipids and saposin-lipid bilayer, respectively. (**B**) Models built for different $5HT_{3A}R$-Salipro conformations, with ion permeation pathways estimated with HOLE programme (Smart et al., 1996). Red, green and blue spheres represent radii of <1.8 Å, 1.8-3.3 Å, and >3.3 Å, respectively. (**C**) Static pore radius plot of three $5HT_{3A}R$-Salipro conformations along the receptor pseudo-symmetric axis, overlaying with a $5HT_{3A}R$-Detergent serotonin bound conformation (PDB-6DG8) (Basak et al., 2018a). Dashed line represents hydrated sodium ion (radius 2.76 Å).

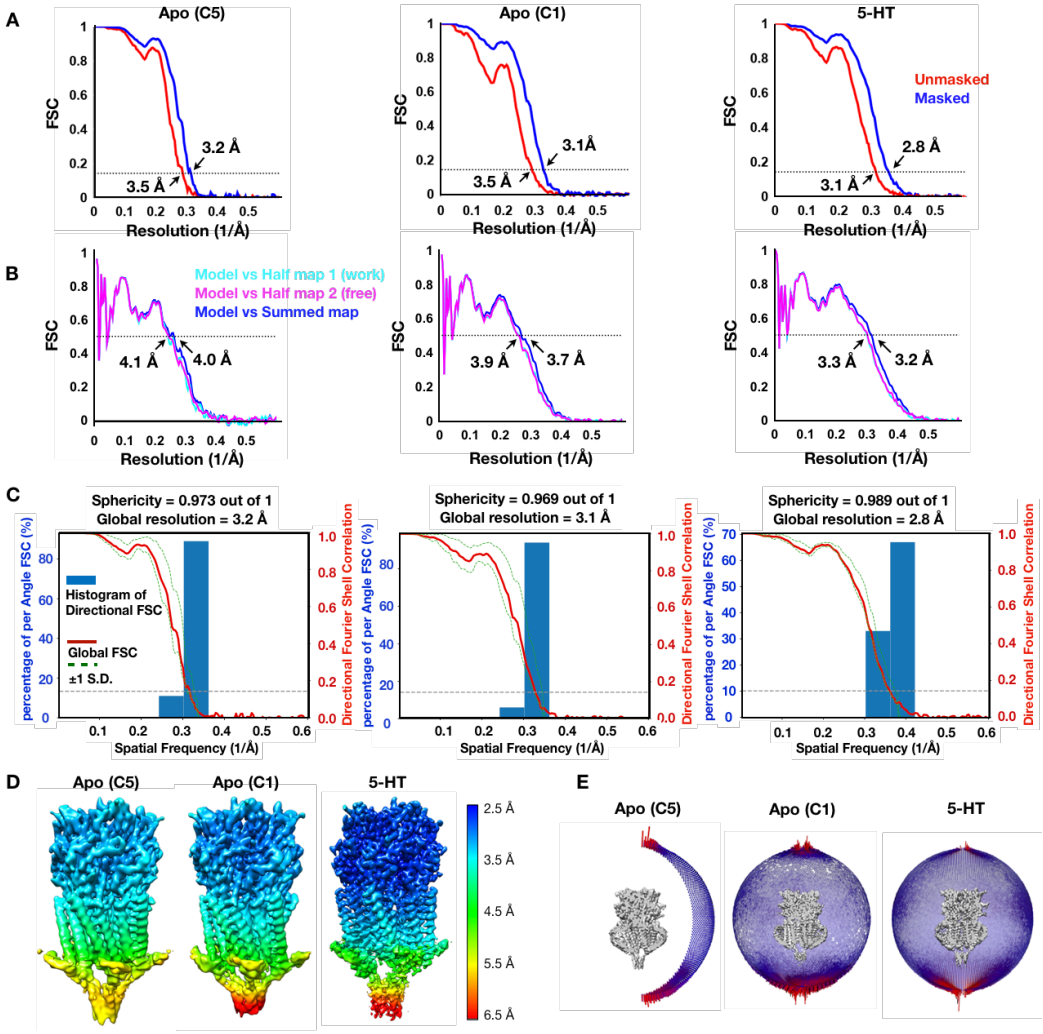

Figure 3.3 Resolution estimation and model validation. (**A**) FSC curves for the reconstruction after (blue) and before (red) applying a soft mask in RELION-3.0 processing. (**B**) FSC curves of the refined built models versus half map 1 (used during refinement, cyan), versus half map 2 (not used during refinement, magenta), and versus summed map (full dataset, blue). (**C**) 3DFSC describing the global and directional resolution. (**D**) Local map resolution estimated using RELION-3.0; maps locally sharpened using LocScale. (**E**) Angular distribution of particles that contributed to the final maps.

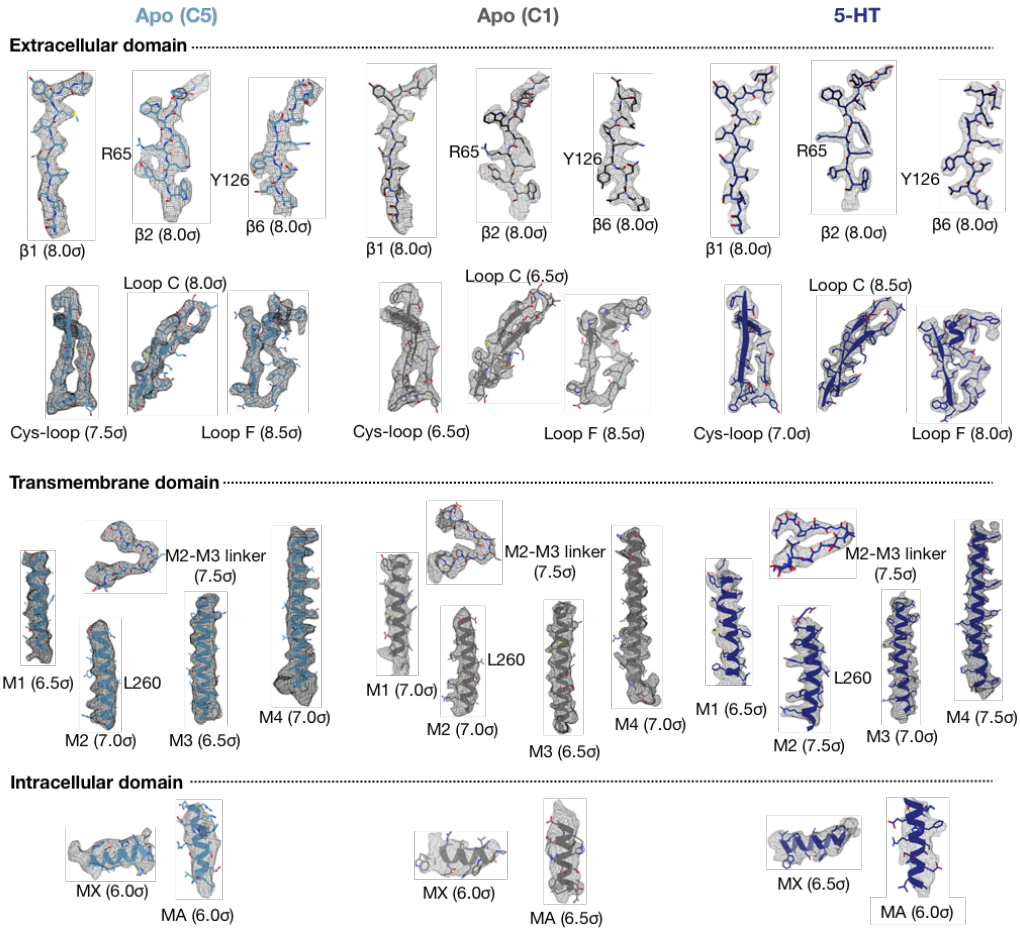

Figure 3.4 Map quality. Representative regions of the built $5HT_{3A}$R-Salipro-Apo forms (C5, light-blue; C1, grey) and $5HT_{3A}$R-Salipro-5HT (dark-blue) models and corresponding EM map densities locally sharpened using LocScale (mesh) at the listed contour levels.

3.2.1 Cryo-EM reveals Apo state symmetric $5HT_{3A}$R-Salipro conformation

Applying RELION 2D averaging, 3D classification with and without symmetry imposing and symmetry expansion, the $5HT_{3A}$R-Salipro-Apo dataset, collected in the absence of serotonin, finally yields two different Apo conformations of the $5HT_{3A}$R-Salipro (**Figure 3.2** A). The main form follows C5 symmetry and derived from 61% of the particles at the nominal resolution of 3.2 Å, the other is asymmetric (C1) with 39% of the particles at 3.1 Å (**Figure 3.3** A). Local resolution and 3DFSC indicated increased flexibility along the receptor axis from ECD towards ICD with the decreasing of its local resolution.

The asymmetric Apo form is currently the first observed asymmetric Apo form of the homo-pentameric serotonin receptor according to literature, that would be described separately in the next Section 3.2.2. The C5 symmetric $5HT_{3A}$R-Salipro-Apo form will be taken as the main Apo form when comparing with the published cryo-EM $5HT_{3A}$R-Detergent-Apo form (PDB-6BE1). And a detailed comparison between our asymmetric Apo form to the symmetric Apo form would be given (Section 3.2.2).

The differences between $5HT_{3A}$R-Salipro-Apo form and the $5HT_{3A}$R-Detergent-Apo form (PDB-6BE1) are all over the receptor from ECD on-top to the ICD at bottom (**Figure 3.5**). The $5HT_{3A}$R-Salipro-Apo has a more compact ECD, the root mean square deviation (RMSD) for every individual chain at ECD between $5HT_{3A}$R-Salipro-Apo and $5HT_{3A}$R-Detergent-Apo is around 1.4 to 1.5 Å. Also, the M4 helices of the $5HT_{3A}$R-Salipro-Apo are about ~9° more tilted measured at their bottom (**Figure 3.5** A), and there are “kink” between M4 and MA helices (**Figure 3.5** H). The more tilted M4 helices of $5HT_{3A}$R-Salipro-Apo have its W426 seating about 10.6 Å more upwards away from those of the $5HT_{3A}$R-Detergent-Apo form.

Together with M4 tilting, M1 and M3 helices of $5HT_{3A}$R-Salipro-Apo state present tilting ~15° and ~9° compared to that of the detergent state accordingly, resulting in the displacement about 7 Å. (**Table 3.1**). Furthermore, MX helices also seat more upwards, the displacement measured at W320 (chain C) is about 16.4 Å (**Figure 3.5** I).

As a result, the $5HT_{3A}$R-Salipro-Apo form is remarkably shorter along its receptor axis than the $5HT_{3A}$R-Detergent-Apo form. The TMD of the $5HT_{3A}$R-Salipro-Apo form is ~40 Å across the TMD, which is about 7 Å shorter than the detergent Apo form presents (PDB-6BE1). The upward rearrangements of both W426 at M4 and W320 at MX helices are considered to be more energetic-favorable as seating at the hydrophobic mismatch of lipid bilayers (de Jesus, 2013).

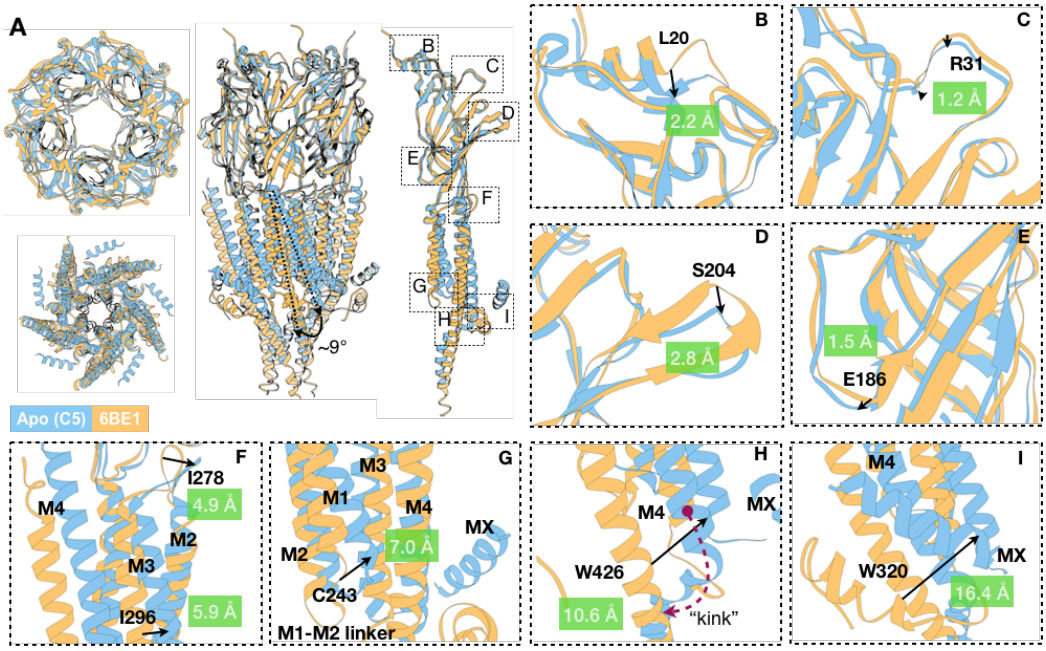

Figure 3.5 Detailed comparison of symmetric $5HT_{3A}$R-Salipro-Apo form to $5HT_{3A}$R-Detergent-Apo form. Overview (**A**) with different regions at the ECD (**B-E**), and TMD (**F-I**), the highlighting the structural differences between the C5 symmetric $5HT_{3A}$R-Salipro-Apo (light-blue) and $5HT_{3A}$R-Detergent-Apo (6BE1, yellow) forms.

Table 3.1 Tilted TMD helices of C5 symmetric $5HT_{3A}R$-Salipro-Apo compared with $5HT_{3A}R$-Detergent-Apo (PDB-6BE1) form.

Apo (C5) vs 6BE1					
Tilting (Å)	**M1 (C243)**	**M2 (G249)**	**M3 (L307)**	**M4 (W426)**	**Sum**
A	7	4	7	11	29
B	7	4	7	11	29
C	7	4	7	11	29
D	7	4	7	11	29
E	7	4	7	11	29
Average	7	4	7	11	29
Angle-tilted (°)	**M1**	**M2**	**M3**	**M4**	**Sum**
A	14	7	9	9	39
B	16	7	9	10	42
C	14	6	9	10	39
D	16	7	9	10	42
E	13	4	8	9	34
Average	15	6	9	10	39

3.2.2 Cryo-EM reveals an asymmetric Apo conformation of $5HT_{3A}$R-Salipro

After initial screening to get rid of broken particles from the Apo dataset (processing steps including multiple iterations of 2D averaging/ 3D classification with C5 symmetry for better particle separation), the data processing underwent a 3D classification without alignment into 6 classes without force imposing symmetry (C1 symmetry applied), which offered a well separation of two major particle sets: the symmetric and asymmetric particle sets.

Afterwards, different particle sets were regrouped according to their degree of symmetry and refined with proper symmetric settings respectively (C5 or C1). With this approach, the symmetric and asymmetric $5HT_{3A}$R-Salipro-Apo forms were both well resolved in near atomic resolution, allowed the building of atomic models for both forms.

As a homo-pentameric serotonin receptor, the construct among five subunits are the same. However, the existence of the asymmetric conformation of $5HT_{3A}$R-Salipro-Apo was demonstrated with further analysis. In order to evaluate the degree of symmetry of the $5HT_{3A}$R-Salipro-Apo conformations, symmetry expansion of the particle sets assigned to the Apo-$5HT_{3A}$R-Salipro-C5 form was first performed along its symmetry axis (the pore axis) and 3D classified into 16 classes without alignment using a loose monomer mask. At the resolution obtained (~4.3 to 4.6 Å estimated by 3D classification in Relion), no notable differences were found, suggesting that the consensus C5 symmetric $5HT_{3A}$R-Salipro-Apo form is promising at the resolution achieved.

With the same strategy, obvious differences were found between the different monomer classes extracted from the C1 asymmetric $5HT_{3A}$R-Salipro-Apo form (**Figure 3.6**). Therefore, in the absence of ligand, the majority of particles adapt a C5 symmetric Apo form, meanwhile, there are still a large number of particles adapting a C1 asymmetric Apo form.

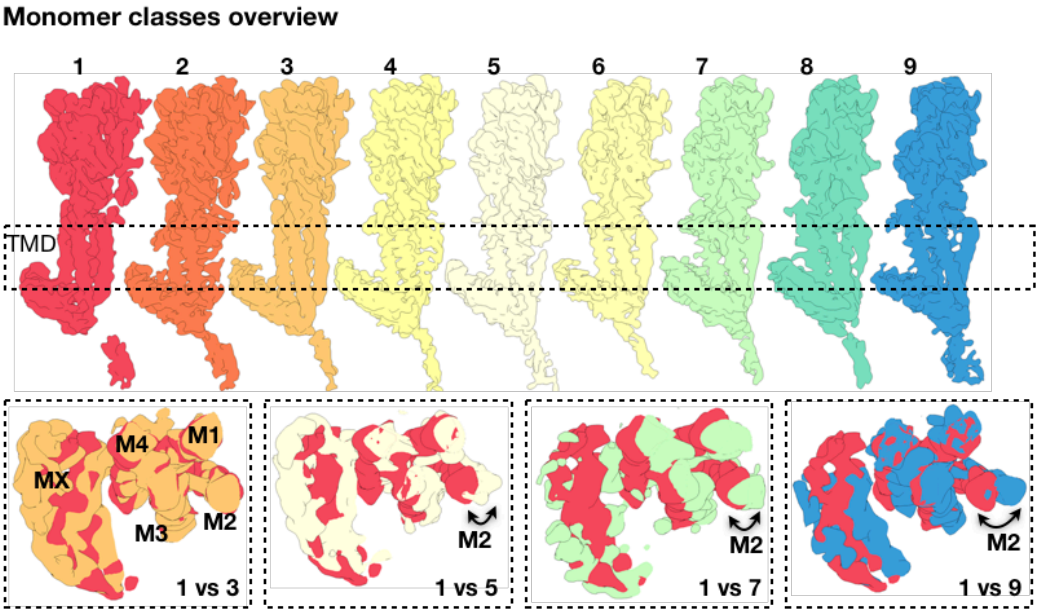

Figure 3.6 Symmetry expansion and focused monomer 3D classification of asymmetric 5HT$_{3A}$R-Salipro-Apo-C1 dataset. Symmetry expanded monomer-focused 3D classification of the particles corresponding to 5HT$_{3A}$R-Salipro-Apo-C1 yielded nine well-resolved classes. The classes are ordered according to the position of their TMD relative to the pore axis (furthest: class 1; closest: class 9). The bottom panel shows a cross section of a superposition of the indicated class with class 1 at the TMD viewed from the ECD, highlighting the structural differences between the classes.

Comparing between our two 5HT$_{3A}$R-Salipro-Apo forms, although their global conformational architectures are the same, differences could be easily found towards the cytoplasmic side between the asymmetric and symmetric Apo 5HT$_{3A}$R-Salipro forms. The RMSD measurements for each subunit of the asymmetric 5HT$_{3A}$R-Salipro-Apo form to the C5 symmetric 5HT$_{3A}$R-Salipro-Apo form are shown in **Table 3.2**, at the whole chain and at different domains.

Table 3.2 Asymmetry of C1 $5HT_{3A}$R-Salipro-Apo. Root mean square deviation (RMSD) between the individual chains of the C1 asymmetric $5HT_{3A}$R-Salipro-Apo form and between each chain and the C5 symmetric $5HT_{3A}$R-Salipro-Apo form is given calculated for **A**, the whole chain, **B**, the ECD only, and **C**, the TMD only.

A, WHOLE CHAIN

RMSD (Å)	A	B	C	D	E	C5
A		2.30	1.42	1.63	1.40	1.01
B	2.30		2.90	2.93	1.70	2.11
C	1.42	2.90		2.08	2.20	1.29
D	1.63	2.93	2.08		1.67	1.32
E	1.40	1.70	2.20	1.67		1.05

B, ECD ONLY

RMSD (Å)	A	B	C	D	E	C5
A		0.42	0.45	0.52	0.44	0.52
B	0.42		0.48	0.51	0.46	0.51
C	0.45	0.48		0.43	0.43	0.55
D	0.52	0.51	0.43		0.48	0.58
E	0.44	0.46	0.43	0.48		0.47

C, TMD ONLY

RMSD (Å)	A	B	C	D	E	C5
A		3.49	2.01	2.40	2.11	1.32
B	3.49		4.51	4.56	2.40	3.23
C	2.01	4.51		3.24	3.40	1.88
D	2.40	4.56	3.24		2.57	1.98
E	2.11	2.40	3.40	2.57		1.46

As the RMSD shown in **Table 3.2** B and **Figure 3.7** A, there is no significant differences were observed among the ECDs of the five subunits of the asymmetric $5HT_{3A}$R-Salipro-Apo form (RMSD, 0.4-0.5 Å) or to the C5 symmetric $5HT_{3A}$R-Salipro-Apo form (RMSD 0.5-0.6 Å), except that at the position of S204, part of loop C, was observed to vary by about 0.4-1.5 Å relative to its position in the C5 symmetric $5HT_{3A}$R-Salipro-Apo form (**Figure 3.7** B).

Larger differences where observed between subunits at the TMD (RMSD 2.0-4.6 Å), with chain B deviating most from the C5 symmetric $5HT_{3A}$R-Salipro-Apo form (RMSD 3.2 Å, compared to 1.3-2.0 Å for the other chains). The M2 helix of every chain presents different displacements relative to its position in the C5 symmetric $5HT_{3A}$R-Salipro-Apo conformation; taking a cross section at L260 (9' position along M2 helices, **Figure 3.7** D), the carbon backbone displacement varies from 1.8 to 3.8 Å. Also, the M2 helices of chain A/C/D are positioned closer to the receptor pore axis, while M2 of chain B/E are positioned further away (**Figure 3.7** C). As a result, the asymmetric $5HT_{3A}$R-Salipro-Apo form is slightly more constrained at TMD domain compared to the C5 symmetric $5HT_{3A}$R-Salipro-Apo form (**Figure 3.2** B).

At the ECD-TMD interface, the conformational arrangement of the Cys-loop, M2-M3 linker, the β1-β2 loop and the conserved pocket, composed of W187, R218, D145, F142 and E53 (Nemecz et al., 2016), are also found stay conformational identical and consistent between the two Apo forms (**Figure 3.7** E).

In order to evaluate the stability of the asymmetric $5HT_{3A}$R-Salipro-Apo conformation, we performed MD simulations together with the symmetric $5HT_{3A}$R-Salipro-Apo and the serotonin-bound $5HT_{3A}$R-Salipro-5HT conformation, that we will discuss later in Section 3.2.3.

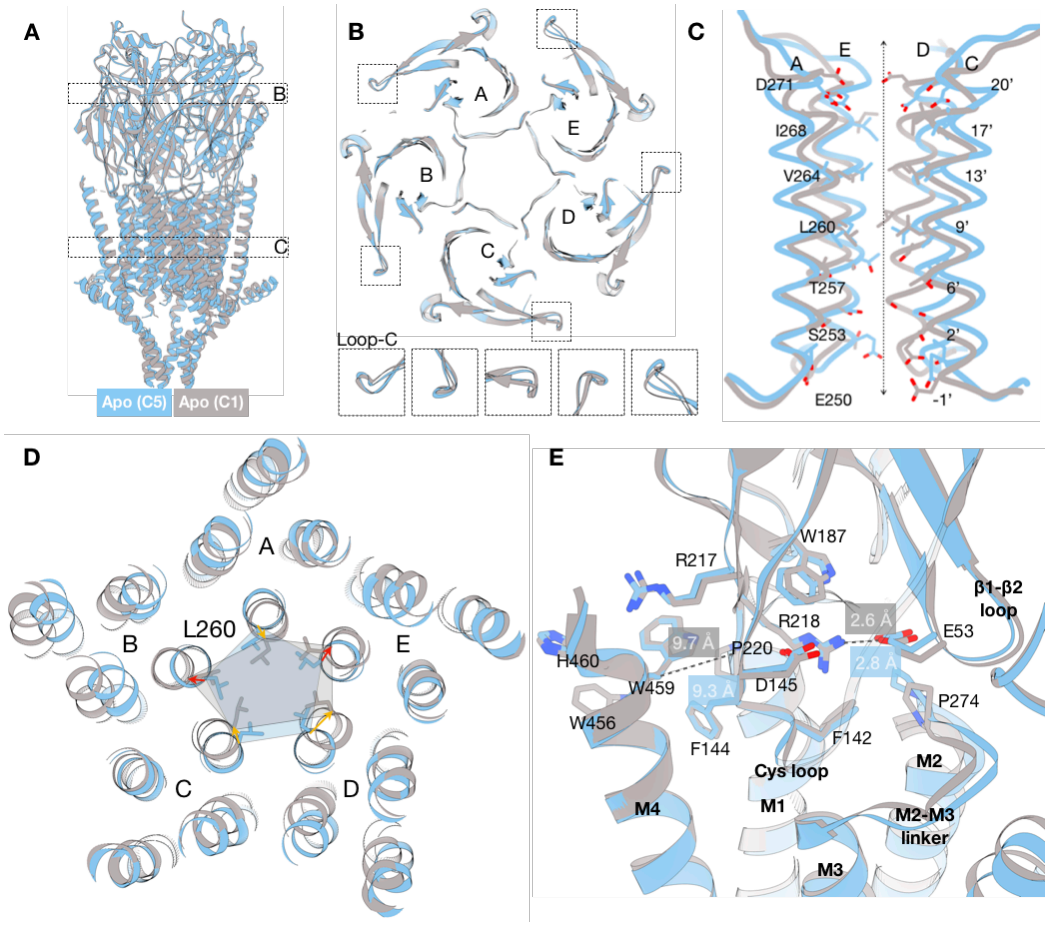

Figure 3.7 Comparison of two Apo conformations of $5HT_{3A}R$-Salipro. (**A**) Overview of the models for the $5HT_{3A}R$-Salipro-Apo forms in superposition (C5, light blue, and C1, grey). (**B**) Cross section at ECD. (**C**) M2-pore lining residues. (**D**) Cross section at L260, 9' position of M2 helices showing the relative displacements of every M2 helix, viewing from ECD side downwards to ICD. (**E**) the conserved region at ECD-TMD interface.

3.2.3 Cryo-EM reveals serotonin-bound state $5HT_{3A}$R-Salipro conformation

The dataset of the $5HT_{3A}$R-Salipro with the presence of 100 µM serotonin (in a saturated concentration (Corradi et al., 2009), and 2 mM $CaCl_2$) yields only an asymmetric serotonin-bound conformation with applying the same processing strategy as the $5HT_{3A}$R-Salipro-Apo dataset.

The resolved EM density of serotonin-bound $5HT_{3A}$R-Salipro ($5HT_{3A}$R-Salipro-5HT) shew well defined densities for serotonin (5-HT) molecules in all five ligand binding pockets (LBPs) (**Figure 3.8**). The serotonin-bound EM map is at a nominal resolution of 2.8 Å (**Figure 3.3**, 5-HT), allowed the building of promising atomic model. Local resolution estimation and 3DFSC shew also its increased flexibility towards TMD and ICD, as these domains are where the receptor responses the most during channel opening and conducting (Nemecz et al., 2016).

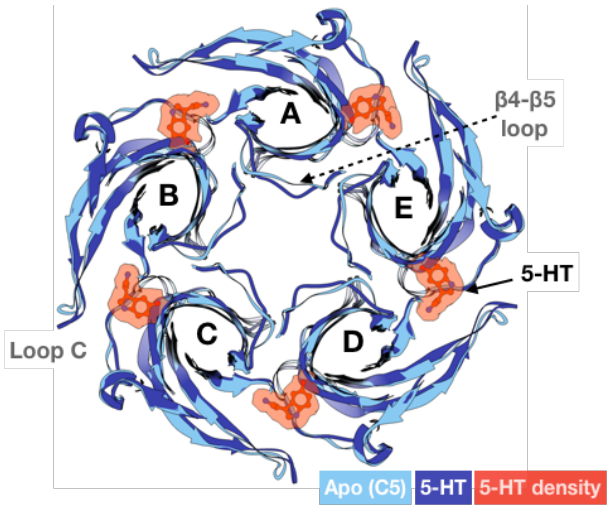

Figure 3.8 Cryo-EM revealed serotonin-bound $5HT_{3A}$R-Salipro state. Cross section at LBPs, all five EM densities of serotonin (5-HT) molecules (transparent red, contoured at σ 8.0) observed in the $5HT_{3A}$R-Salipro-5HT map (dark blue).

Comparing with the serotonin-bound $5HT_{3A}$R-Detergent form (PDB-6DG8), $5HT_{3A}$R-Salipro-5HT form also looks shorter along its receptor axis (~40Å, versus ~45Å for 6DEG) , mainly due to its TMD helices are more tilted ~6-7° (**Table 3.3**) and resulting in a displacement about ~4-7Å at the bottom of every TMD helix (from M1-M4, respectively). The ECD of $5HT_{3A}$R-Salipro-5HT shew no big differences (**Figure 3.9** A), but more compact than the $5HT_{3A}$R-Detergent-5HT,

the RMSD at ECD between the two forms is about 1.5 Å. While, the differences are much more obvious at TMD and ICD. The M4 and MX helices of $5HT_{3A}$R-Salipro-5HT seat more upwards. The displacement of every chain measured at W320 (MX) of $5HT_{3A}$R-Salipro-5HT is 8.2 Å, 6.7 Å, 10.3 Å, 7.0 Å and 5.3 Å accordingly (**Figure 3.9** D). More importantly, each M2 helices of $5HT_{3A}$R-Salipro-5HT seats further away from its pore axis, results in a more open conformation than $5HT_{3A}$R-Detergent-5HT (6DG8, known previously as the “most-open” state) (**Figure 3.9** E). Based on the static pore profile (**Figure 3.2** C), the pore diameters of the $5HT_{3A}$R-Salipro-5HT and $5HT_{3A}$R-Detergent-5HT states measured at the central location (the 9’ constriction site - L260) of the hydrophobic gate on the pore-lining M2 helices are 11.7 Å and 6.7 Å accordingly. $5HT_{3A}$R-Salipro-5HT has its pore size about 5 Å larger in comparison.

Table 3.3 Tilted TMD helices of $5HT_{3A}$R-Salipro-5HT (5-HT bound) compared with $5HT_{3A}$R-Detergent-5HT (PDB-6DG8).

5-HT bound vs 6DG8					
Tilting (Å)	**M1 (C243)**	**M2 (G249)**	**M3 (L307)**	**M4 (W426)**	**Sum**
A	5	3	8	6	22
B	8	3	4	8	23
C	5	5	7	6	23
D	6	7	3	7	23
E	6	3	4	7	20
Average	6	4	5	7	22
Angle-tilted (°)	M1	M2	M3	M4	Sum
A	6	7	12	4	29
B	9	6	4	9	28
C	5	9	12	3	29
D	9	6	2	8	25
E	6	4	3	6	19
Average	7	6	7	6	26

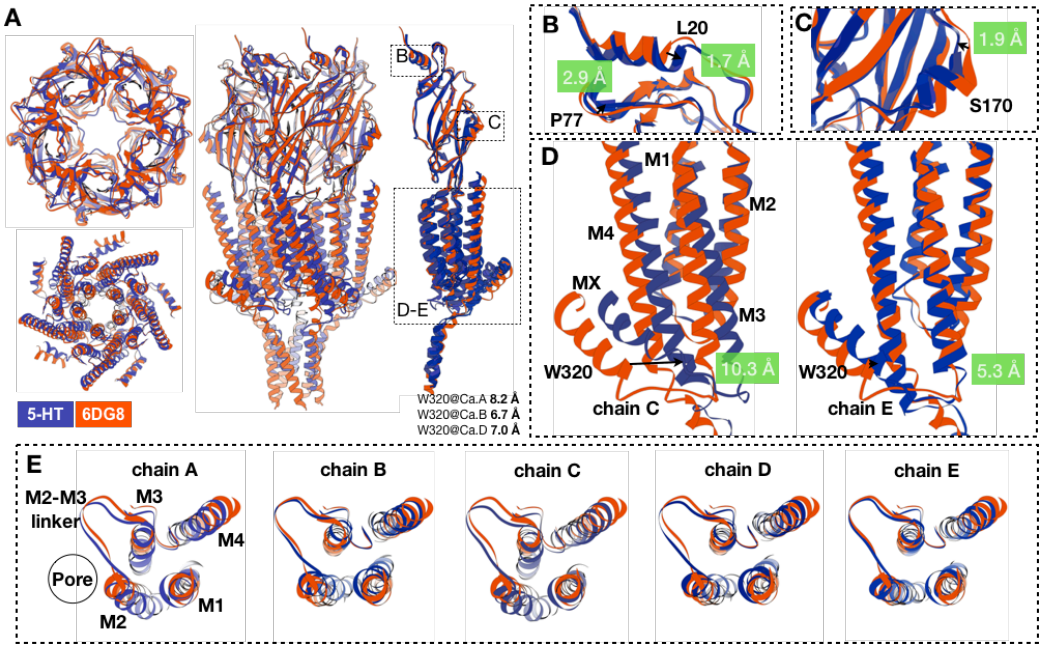

Figure 3.9 Detailed comparison of $5HT_{3A}$R-Salipro-5HT (dark-blue) to $5HT_{3A}$R-Detergent-5HT (6DG8, orange) in superposition. Overview (**A**) with different regions showing conformational differences at the (**B-C**) ECD; (**D**) position of MX differs between the $5HT_{3A}$R-Salipro-5HT and $5HT_{3A}$R-Detergent-5HT forms by 8.2 Å, 6.7 Å, 10.3 Å, 7.0 Å and 5.3 Å measured at the Cα atom of W320 of chain A to E, respectively (only chain C and E are shown representing the largest and smallest difference); and (**E**) superposition of the $5HT_{3A}$R-Salipro-5HT and 6DG8 at the TMD for the individual chains.

The unbiased all-atom molecular dynamic (MD) simulations (3x200 ns) were performed in an explicit lipid bilayer by Dr. Yuan and colleagues. During all three simulations, several sodium (**Figure 3.10**) permeation events were observed of the $5HT_{3A}$R-Salipro-5HT conformation. The results demonstrate that our $5HT_{3A}$R-Salipro-5HT state is fully opened that allows free sodium ion permeation through the pore. While, applying the similar un-constrained MD simulations on the $5HT_{3A}$R-Detergent-5HT forms (PDB-6DG8), neither water molecule wetting of the pore, nor free sodium ion conductance was seen (**Figure 3.10** A, 6DG8), which presents as our two Apo forms (**Figure 3.10** A). This observation makes the previous claimed “most-open” serotonin-bound state in detergent (6DG8) more ambiguous, and brings the gating mechanism still open for discussion.

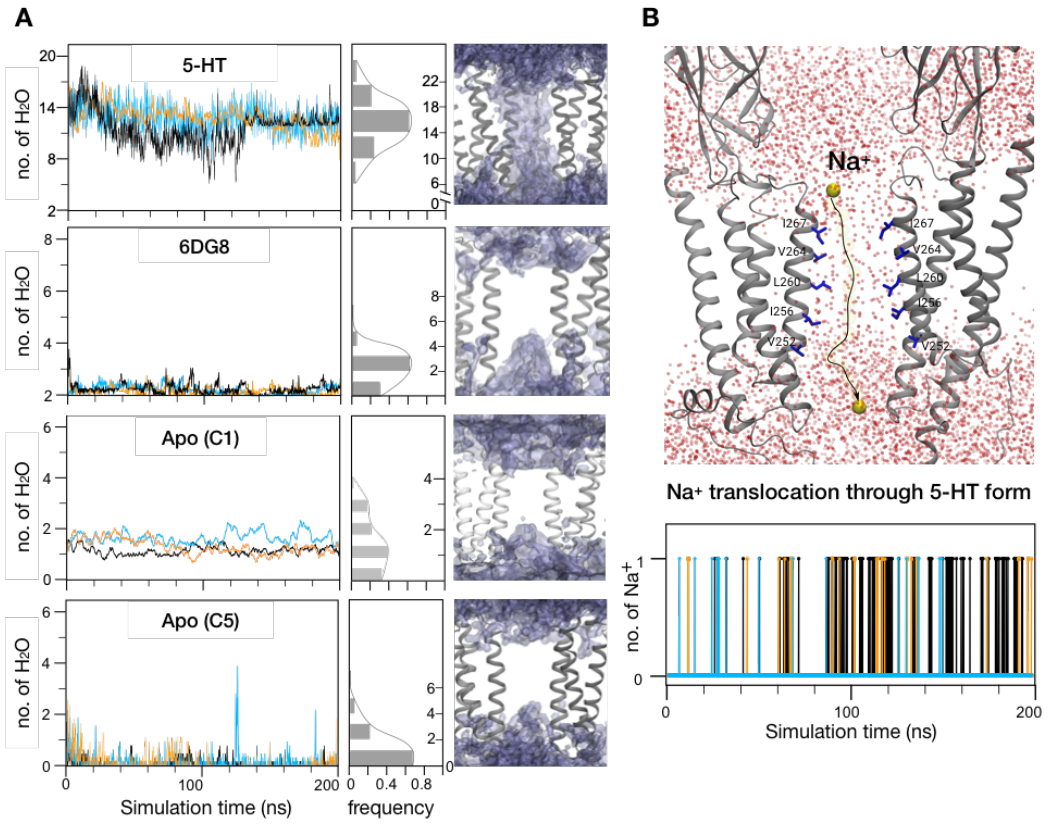

Figure 3.10 Pore wetting during MD simulations for $5HT_{3A}R$-Salipro-5HT form (5-HT) and $5HT_{3A}R$-Detergent-5HT conformations (PDB-6DG8), together with the two $5HT_{3A}R$-Salipro-Apo forms (C1 and C5) for comparison. (**A**) Averaged water molecules density within 4 Å of L260 at TMD of $5HT_{3A}R$-Salipro. Left – number of water molecules, solid lines in different colors indicate results of three simulations. Right – water molecule densities shown in purple, two subunits of $5HT_{3A}R$-Salipro shown in grey. (**B**) Upper panel – the trajectory of a single sodium ion (yellow) translocated across the pore. Lower panel – number of sodium ions translocated through the pore during three 200 ns simulations.

During the unbiased MD simulations, significant differences in the conformation of M2 helices were observed (**Figure 3.11**) for our $5HT_{3A}$R-Salipro-5HT conformation. Firstly, the cross-sectional areas circulated by M2 helices were measured for each forms at I268 (next to ECD) and V252 (next to ICD), showing that the M2 helices in the $5HT_{3A}$R-Salipro-5HT form adopted an "A" shape, with the cross-sectional area about 110 $Å^2$ larger at the intracellular region compared to the extracellular region, while M2 helices in $5HT_{3A}$R-Detergent-5HT adapted "V" shape, respectively (**Figure 3.11** A). Secondly, the root-mean-square fluctuation (RMSF) of M2 indicated that $5HT_{3A}$R-Salipro-5HT is much more flexible than $5HT_{3A}$R-Detergent-5HT (**Figure 3.11** B). Thirdly, M2 helices of the $5HT_{3A}$R-Salipro-5HT and $5HT_{3A}$R-Detergent-5HT forms presented very different curvatures. The M2 helices of the $5HT_{3A}$R-Salipro-5HT were noticed in average larger than the $5HT_{3A}$R-Detergent-5HT. The former one has its M2 helices bending mainly at V252 near the ICD, while the latter at I268 near the ECD (**Figure 3.11** C). Sodium ions passing through the M2 circulated pore region virtually were unhindered within approximately 2-3 ns, suggesting that the flexibility of M2 observed of the $5HT_{3A}$R-Salipro-5HT conformation could be essential for channel permeation.

With the static comparison and further demonstration from unbiased all-atoms MD simulations, it is clear that our serotonin-bound $5HT_{3A}$R-Salipro form is fully conductively opened. Thus, it is important to look into more details about the reason why binding of serotonin induced the channel opening of the serotonin receptor in lipid bilayer, but not of those in detergent.

To further demonstrate the hypothesis, five serotonin molecules were placed in the LBPs of both the $5HT_{3A}$R-Salipro-Apo forms and the X-ray crystallography resolved detergent-solubilized Apo forms (PDB-4PIR) (Hassaine et al., 2014), and 3x200 ns unbiased all-atom MD simulations were performed. Interestingly, water wetting of the pore was seen only for the $5HT_{3A}$R-Salipro-Apo conformations, but not for the latter, supporting the allosteric role of the lipid environment in stabilising receptor conformations that are primed for gating (**Figure 3.12**).

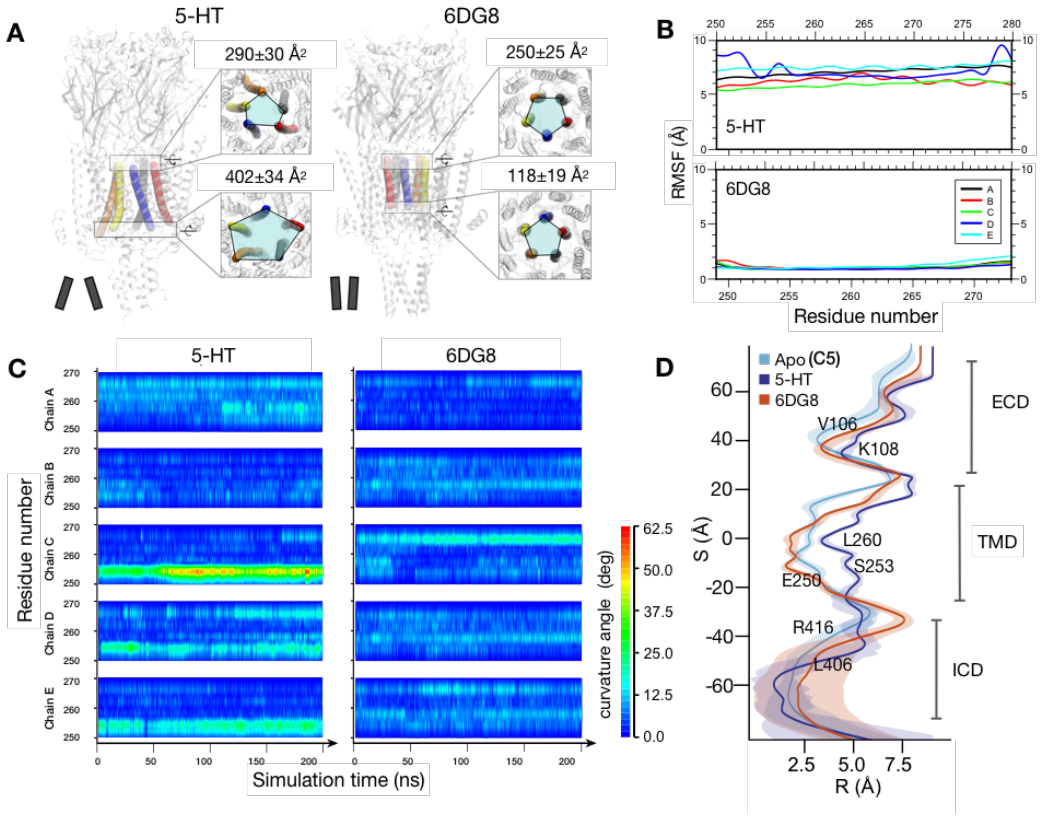

Figure 3.11 M2 conformation during MD simulations for different serotonin-bound models. (**A**) Cross-sectional area at I268 (upper panels) and V252 (lower panels) showing different conformation of M2 for $5HT_{3A}R$-Salipro-5HT (left) and 6DG8 (right). (**B**) Root-mean-square fluctuation (RMSF) of M2 for each chain (A-E). (**C**) Local curvature angle along M2 helices during the MD trajectories. (**D**) MD simulated pore radius along the receptor pore axis with C5 symmetric $5HT_{3A}R$-Salipro-Apo for comparison.

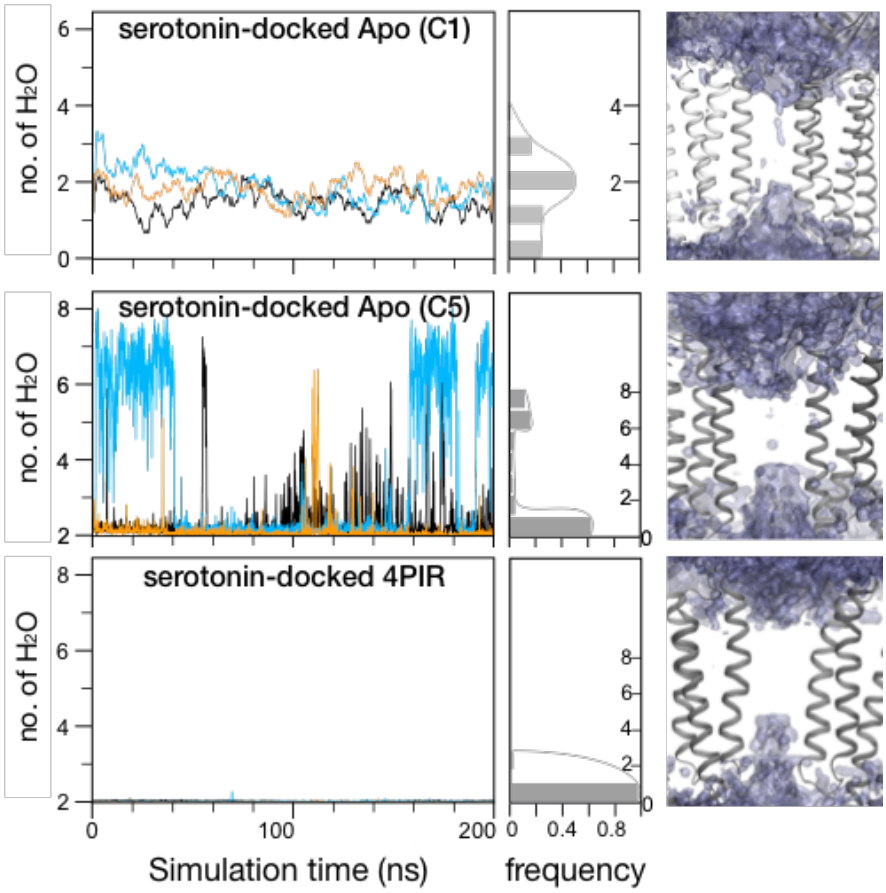

Figure 3.12 Pore wetting - Averaged water density within 4 Å of L260 at TMD during MD simulations of two $5HT_{3A}R$-Salipro-Apo forms, C1 and C5, (in a BPL-mimicking lipid environment) and 4PIR (in POPC) with five serotonin molecules docked into the ligand binding pockets (LBPs). Left panels – number of water molecules, solid lines in different colours indicate results of three simulations and the histograms show the averaged distribution of the numbers of observed water molecules. Right panels – water molecule densities shown in purple, two subunits of each model shown in grey.

3.3 $5HT_{3A}R$-Salipro, from Apo to open

In this section, we will describe in detail about the transition of the $5HT_{3A}R$-Salipro from Apo state to its serotonin-bound opened state in details. Further details of lipid-allosteric modulation on receptor activation are described in Section 3.4.

3.3.1 Starting from ligand binding at LBPs

The serotonin molecules bound at LBPs showed similar poses as observed in the $5HT_{3A}R$-Detergent-5HT form (PDB-6DG8), with the amino group stabilized through cation-π interactions with the conserved W156 (loop B), and Y207 (loop C) on the principal side of the LPB (**Figure 3.13**). The binding of serotonin led to inward displacement of loop C (as "capping") compared to the $5HT_{3A}R$-Salipro-Apo-C5 state, as previously reported for other pLGICs (daCosta and Baenziger, 2013). The displacement at loop C is stabilized by an electrostatic interaction (~ 5 Å) between D202 (loop C) on the principal side of LBP and R65 (β2) on the complementary side of LBP (**Figure 3.13** B). The $5HT_{3A}R$-Salipro-5HT conformation is asymmetric, however, no significant differences were observed between the ECDs of the five subunits of the $5HT_{3A}R$-Salipro-5HT form. The RMSDs at ECD domain are around 0.7-0.8 Å (**Table 3.4**) at the resolution obtained (~ 3 Å).

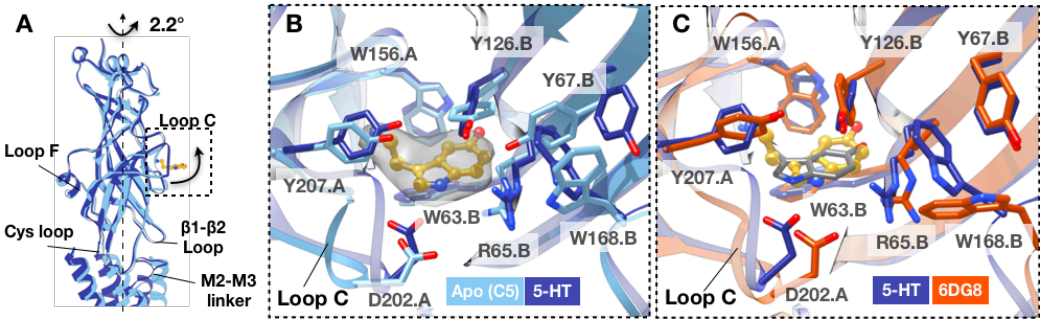

Figure 3.13 Serotonin-induced conformational changes of $5HT_{3A}R$-Salipro. (**A**) Superposition of the ECD of the Apo and $5HT_3R$-Salipro-5HT structures. Arrows indicate direction of displacements. (**B**) Close-up of the LBP showing serotonin (yellow) and the corresponding density (transparent grey, contoured at σ 8.0). Residues on the primary and complementary subunits are labelled ".A" and ".B" respectively. (**C**) LBPs of the serotonin-bound $5HT_{3A}R$-Salipro and $5HT_{3A}R$-detergent (6DG8) structures. Serotonin molecule of 6DG8 is displayed in grey.

Table 3.4 Asymmetry of the $5HT_{3A}R$-Salipro-5HT model. Root mean square deviation (RMSD) between the individual chains is given **A,** at ECD only, and **B,** over the entire chain.

A, ECD ONLY

RMSD (Å)	A	B	C	D	E
A		0.83	0.73	0.71	0.70
B	0.83		0.72	0.78	0.68
C	0.73	0.72		0.70	0.69
D	0.71	0.78	0.70		0.68
E	0.70	0.68	0.69	0.68	

B, WHOLE CHAIN

RMSD (Å)	A	B	C	D	E
A		3.49	1.94	3.09	2.84
B	3.49		3.95	1.92	2.04
C	1.94	3.95		3.44	3.22
D	3.09	1.92	3.44		1.94
E	2.84	2.04	3.22	1.94	

Furthermore, on the complementary side of the LPBs, W168 (post-β8, complementary side of LBP) and Y67 (β2) are stabilized in different rotamer positions through a cation-π interaction between R65 and W168, and a π-π stacking between W168 and Y67, which were not observed in the $5HT_{3A}R$-Detergent-5HT form where loop C capping was much loose (**Figure 3.13** C).

The binding energy of serotonin bound to the $5HT_{3A}R$-Salipro-5HT and $5HT_{3A}R$-Detergent-5HT (PDB-6DG8) forms were calculated. For C5 symmetric $5HT_{3A}R$-Detergent-5HT conformation, binding energy is identical among all five LBPs, it is about -27.2±2.7 kcal/mol. While for the asymmetric $5HT_{3A}R$-Salipro-5HT conformation, the binding energies at every LBP are slightly different, -30.8±2.1 kcal/mol, -26.8±1.6 kcal/mol, -32.4±2.5 kcal/mol, -34.4±2.0 kcal/mol and -31.3±2.6 kcal/mol for LBPs at subunits AB, BC, CD, DE, and EA, respectively, giving an averaged binding energy about -31.1±2.2 kca/mol. It tells that serotonin binding is more favorable for the $5HT_{3A}R$-Salipro-5HT conformation, that agrees

with the observation that serotonin binds tighter in the $5HT_{3A}$R-Salipro-5HT than that of $5HT_{3A}$R-Detergent-5HT (PDB-6DG8) (**Figure 3.13** C). The differences observed at LBPs could be one of the reason that $5HT_{3A}$R-Salipro-5HT presents a more opened conformation allowing free sodium ion conducting.

3.3.2 The interface between extracellular domain (ECD) and transmembrane domain (TMD)

Serotonin binding at the LBP induces a 2.2° counter-clockwise rotation of the entire ECD around its own z-axis as viewed from the extracellular side for each subunit (**Figure 3.13** A). The rotation further propagates and repositions the loops at the ECD-TMD interface (**Figure 3.14**): the β1-β2 linker (via β2), the Cys-loop (via loop B, β6 and β7), loop F (via loop C capping transmitted through β9, and via the rotamer switch of W168 on the complementary side), and pre-M1 (via loop C capping transmitted through β10). As a result, the M2-M3 linker of the principal subunit is repositioned, showing a displacement of 2.5-2.9 Å (measured at the Cα atom of L273) relative to the $5HT_{3A}$R-Salipro-Apo form, relaying the conformational changes of the ECD to the TMD.

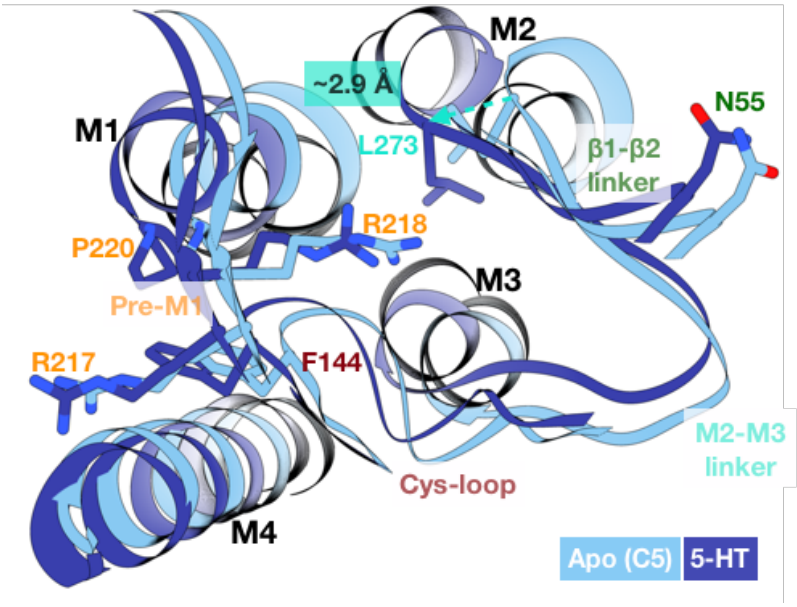

Figure 3.14 ECD-TMD interface rearrangements upon ligand binding. Numbering of highlighted residues is colored according their respective structural elements: brown, orange, cyan, and dark-green for the Cys-loop, pre-M1, the M2-M3 linker, and the β1-β2 linker, respectively.

3.3.3 Opening of the pore

The asymmetry of $5HT_{3A}R$-Salipro-5HT was most pronounced at the TMD, with different conformations observed each subunit. At the TMD in the serotonin-bound state, every of the subunits adopted a clockwise-rotated (relative to the pore axis) and outward-translated geometry compared to the $5HT_{3A}R$-Salipro-Apo-C5 form, resulting in a larger pore diameter.

Taking a cross section at L260 (one of the most constrain site along M2), two modes of rearrangements could be identified (**Figure 3.15**): (1) a major rotation and minor shift (chain A and C); and (2) minor rotation, but major shift (chain B, D, and E). The RMSD between subunits within each of the two groups is about 2 Å, while between groups it is about 3-4 Å (**Table 3.4** B).

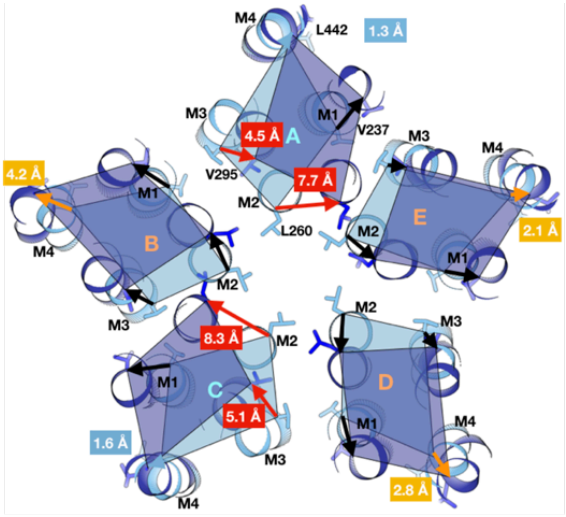

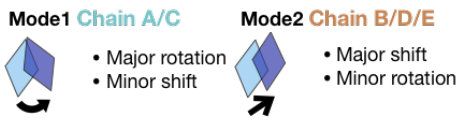

Distance	M1	M2	M3	M4	Rotation
Chain	V237	L260	V295	L442	to Apo
A	4.7 Å	7.7 Å	4.5 Å	1.3 Å	19.7°
B	5.0 Å	5.1 Å	3.9 Å	4.2 Å	12.3°
C	5.1 Å	8.3 Å	5.1 Å	1.6 Å	21.1°
D	4.8 Å	4.7 Å	2.7 Å	2.8 Å	10.5°
E	4.2 Å	4.7 Å	3.1 Å	2.1 Å	10.6°

Figure 3.15 Superposition of Apo (C5) (light blue) and open $5HT_{3A}R$-Salipro states (dark blue) at the TMD showing a cross section at position L260 (9') of M2. The tables give displacement measured at the Cα atoms of residues on each helix in the same cross section. Two modes of rearrangements are observed: (1) major rotation/minor shift for chains A/C, and (2) minor rotation/major shift for chains B/D/E.

Mode 1 resulted in the largest displacements (7.7-8.3 Å at L260 (M2), and 4.5-5.1 Å at V295 (M3)) relative to $5HT_{3A}R$-Salipro-Apo-C5, yielding a conformation as “more-open” among the subunits. While mode 2 presented to have smaller displacements (4.7-5.1 Å at L260 (M2), and 2.7-3.9 Å at V295 (M3)) relative to Apo, they are still larger than observed for $5HT_{3A}R$-Detergent-5HT (PDB-6DG8), yielding a “less-open” conformation. At a lower cross section at the 2’ constriction point (S253) the same pattern was observed (**Figure 3.16**).

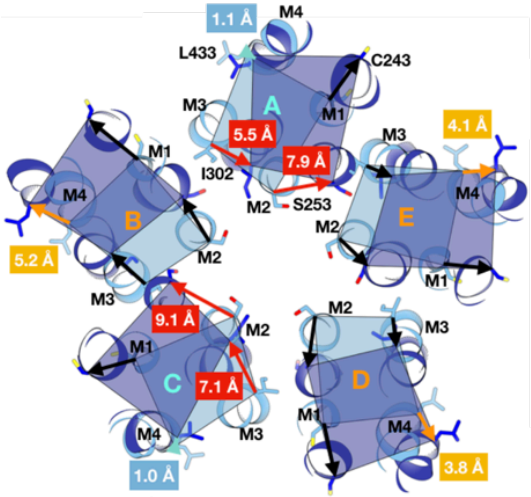

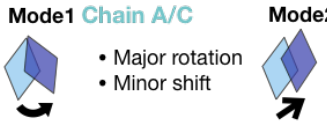

Distance	M1	M2	M3	M4
Chain	C243	S253	I302	L433
A	4.6 Å	7.9 Å	5.5 Å	1.1 Å
B	6.7 Å	6.9 Å	5.0Å	5.2 Å
C	4.7 Å	9.1 Å	7.1 Å	1.0 Å
D	5.7 Å	7.2 Å	3.8 Å	3.8 Å
E	4.9 Å	5.5 Å	3.6 Å	4.1 Å

Figure 3.16 Superposition of Apo (C5) (light blue) and open $5HT_{3A}R$-Salipro states (dark blue) at the TMD showing a cross section at position S253 (2’) of M2. The tables give displacement measured at the Cα atoms of residues on each helix in the same cross section. Two modes of rearrangements are observed: (1) major rotation/minor shift for chains A/C, and (2) minor rotation/major shift for chains B/D/E.

3.3.4 Flexible intracellular domain (ICD)

The ICD, composed of M4 extended MA helices and a disordered stretch is a difficult part for structural characterization, as described in the first Apo mouse serotonin receptor $5HT_3R$ X-ray structure (Hassaine et al., 2014), that the disordered stretch was normally cut off. Also, the published cryo-EM studies of serotonin receptor in detergent presented either a much lower resolution at ICD than the nominal resolution (Basak et al., 2018a; Basak et al., 2018b), or found large number of particles fixed in ice having their ICD broken completely

(Polovinkin et al., 2018). It is due to ICD is natively highly flexible as compared to the ECD which is mostly composed of well packed beta-sheets.

The ICD of the $5HT_{3A}R$-Salipro-Apo and $5HT_{3A}R$-Salipro-5HT forms are less well resolved compared to their ECD and TMD, with local resolution estimated in the range of 5.5-6.5 Å (**Figure 3.3** D). Particularly for the $5HT_{3A}R$-Salipro-5HT form, its ECD gets further stabilized because of serotonin binding, and ICD turns to be more flexible as response to channel opening and ion conductance. The opening of the pore in the TMD and the expansion at bottom of TM helices, combining the "kink" between extended M4 and MX helices, leaving the receptor a large lateral portal on the ion pathway (**Figure 3.17**).

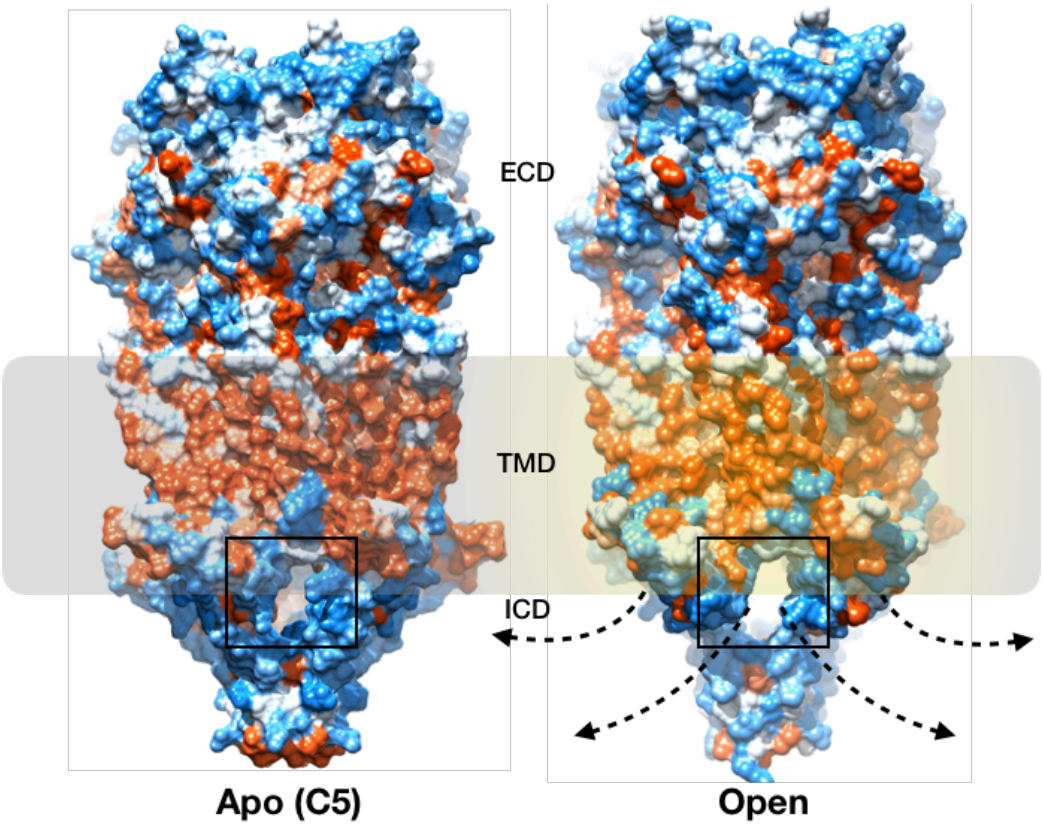

Figure 3.17 The lateral portal on the ion pathway upon channel activation. The squares at ICD indicate the lateral portal before and after channel activation.

3.4 Lipid-modulation of $5HT_{3A}R$

In all our three $5HT_{3A}R$-Salipro EM density maps (two Apo forms and one open form), the saposin-lipid belt surrounding the receptor was observed mostly in disordered manner. However, several more ordered EM densities were resolved seating near the receptor at two locations: adjacent to post-M4 helices (in all three maps, in orange) (**Figure 3.18**), and between the inter-subunit pockets (only in the $5HT_{3A}R$-Salipro-5HT map, in yellow). The detailed descriptions for their interaction with the protein are in the following two Sections 3.4.1 and 3.4.2.

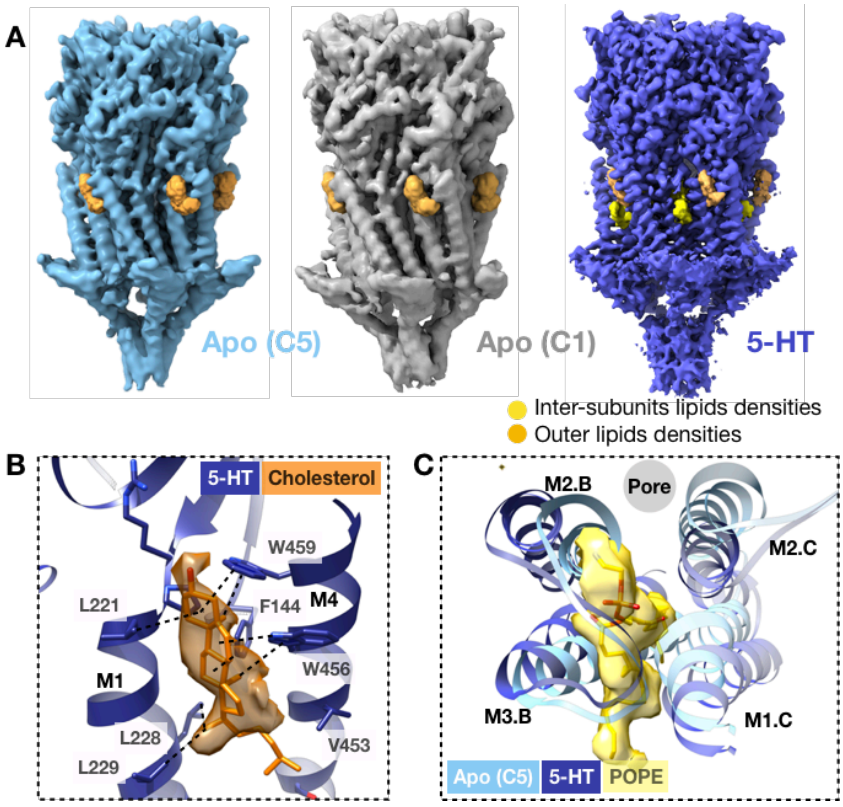

Figure 3.18 Lipid modulation of $5HT_{3A}R$. (**A**) Additional densities corresponding to outer lipids (orange) and inter-subunit lipids (yellow). (**B**) Tentative modelling for cholesterol with densities shown in transparent orange (contoured at σ 2.0). Putative lipid/protein interactions are indicated with dashed lines. (**C**) Tentative modelling for POPE in the density shown in transparent yellow (contoured at σ 2.0) at TMD inter-subunit interface of the $5HT_{3A}R$-Salipro-5HT model viewed from the ECD, overlaid with the $5HT_3R$-Salipro-Apo-C5 model.

3.4.1 Cholesterol at post-M4 helices

Indeed, M4 helices are well-documented sterol binding site in nAChR (Baier et al., 2011; Barrantes and Fantini, 2016; daCosta and Baenziger, 2009). Thus, based on the shape and size of the resolved EM density on the adjacent of M4 helices, they are suggestive of cholesterol (**Figure 3.18** B).

Cholesterol occupied similar positions in both the Apo- and $5HT_{3A}$R-Salipro-open conformations, nested in a hydrophobic pocket with contributions of W459 and W456 (post-M4), P220 (pre-M1), L221, L228 and L229 (M1), and F144 (Cys loop, **Figure 3.19** A, B). In the $5HT_{3A}$R-Detergent-Apo form the distance between post-M4 and the TM bundle is markedly larger than for the receptor in Salipro, precluding the stabilisation of (1) pre-M1 through a cation-π interaction between R217 and W459 observed in the presence of cholesterol, and (2) the Cys-loop through the interactions between F144 and the hydrophobic pocket. A similar picture is seen for the serotonin-bound state in detergent compared to Salipro (**Figure 3.19** C, D).

Overall, this looser packing in the detergent-based conformations affects the positioning of the Cys-loop, pre-M1, and consequently the M2-M3 linker at the TMD-ECD interface; in all $5HT_{3A}$R-Salipro conformations (including the C1 asymmetric Apo form, **Figure 3.7** E), a network of interactions involving a cluster of highly conserved residues (Jaiteh et al., 2016) encompassing R218 (pre-M1), W187 (β9), F142, and D145 (Cys-loop) is found adjacent to the highly conserved proline residue (P274) in the M2-M3 linker (**Figure 3.19** B,D), which plays a crucial role in receptor gating (Cordes et al., 2002). P274 is cradled between this cluster and the β1-β2 loop, whose position is stabilised by a salt-bridge between R218 and the likewise conserved E53 (β1-β2 loop). Notably, in the detergent forms (Apo, PDB-6BE1 and serotonin-bound, PDB-6DG8), residue R218 adopts a different conformation, possibly due to the lack of cholesterol stabilising the position of pre-M1. Consequently, the packing of the conserved cluster of residues is much looser and the salt bridge between R218 and E53 is absent, resulting in a different conformation of the M2-M3 linker compared to the Salipro-reconstituted receptor.

Thus, our structures suggest that the presence of cholesterol allosterically modulates the functioning of the channel through the stabilisation of M4, pre-M1, and the Cys-loop in a tightly packed, “M2-M3-coupled” conformation, offering a

structural basis for the “uncoupled” state that is refractory to activation by ligand reported for nAChR in the absence of cholesterol (daCosta and Baenziger, 2009). Notably, $5HT_{3A}R$ has been shown to reside in cholesterol-rich membrane domains (Eisensamer et al., 2005) and cholesterol depletion also leads to diminished serotonin-induced currents in cells expressing $5HT_{3A}R$ (Nothdurfter et al., 2010).

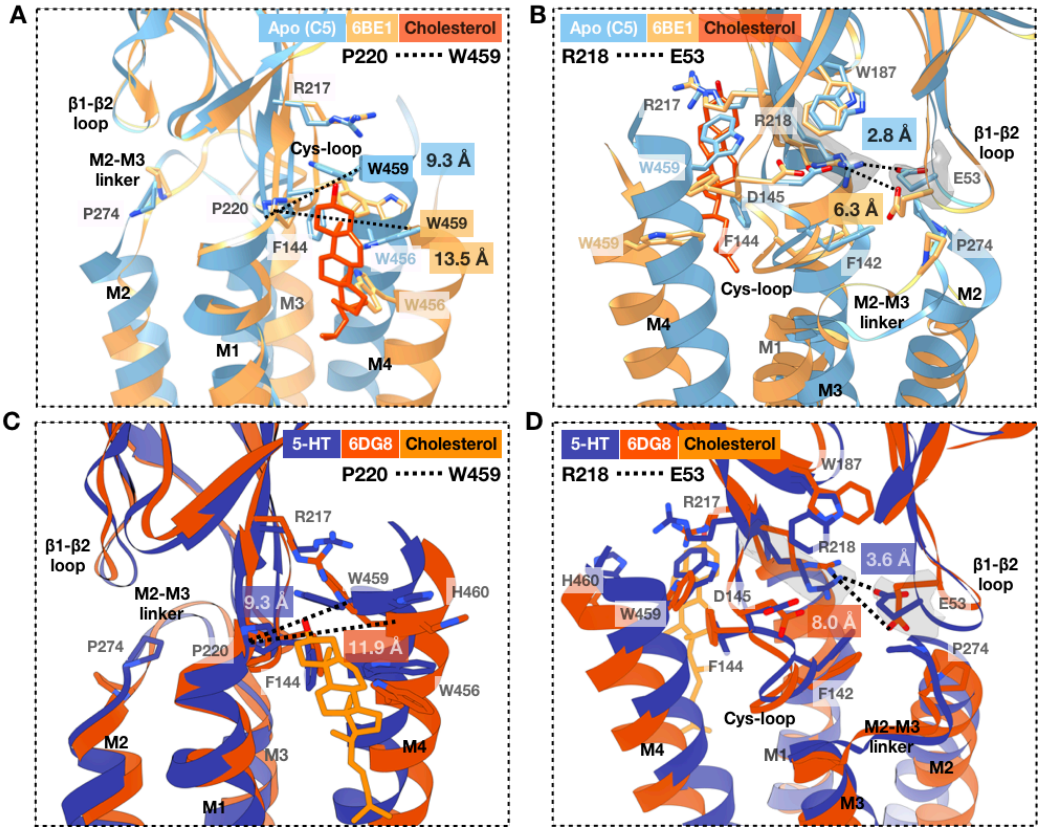

Figure 3.19 Lipid modulation of Cholesterol on $5HT_{3A}R$-Salipro-Apo-C5 and $5HT_{3A}R$-Salipro-5HT conformations, shown in their superposition with Detergent-Apo (6BE1) and Detergent-5HT (6DG8), respectively, for comparison. (**A** and **C**) at the cholesterol binding pocket viewed from the membrane or (**B** and **D**) at the Cys-loop, β1-β2 loop, M2-M3 linker junction viewed from the neighbouring subunit. Part of the Cys-loop (C135-D138) is hidden for clarity. Distances are labelled in the same colour scheme as the structures. Density sharpened using RELION with auto-determined B-factor, shown in transparent grey for residues R218 and E53, at σ 6.0.

3.4.2 Phospholipids at inter-subunit pockets

The EM densities observed at the inter-subunit pockets in the presence of 5-HT were tentatively assigned as partially ordered phospholipids. Fitting of PC, PS, and PE lipid species (**Figure 3.20**), which were all identified as significant components of $5HT_{3A}R$-Salipro (**Table 3.5**), suggests that the density is most consistent with a lipid species with a small headgroup like PE or PS. Unsaturated PE (and to a lesser extend PA) lipids were previously shown to support receptor-gating in nAChR (Criado et al., 1984), suggesting that indeed a small headgroup capable of forming intramolecular hydrogen bounds might be favourable. Tentative modelling of PE suggests the fatty acids of the interfacial lipid species chains contact several hydrophobic TMD residues, including P230 (M1), F265 and I286 (M2), and that the phosphate moiety and headgroup make additional contacts with the M2-M3 linker (**Figure 3.20**).

These lipid-like densities at inter-subunits were absent in both of the $5HT_{3A}R$-Salipro-Apo (C1 and C5) EM density maps, where the cavities between subunits were on average smaller (177 $Å^3$, 200±200 $Å^3$, and 700±400 $Å^3$ for the Apo-C5, Apo-C1, and serotonin-bound $5HT_{3A}R$-Salipro conformations, respectively, **Table 3.6**).

Another smaller, weaker additional density was observed in the largest inter-subunit cavity in the C1 asymmetric $5HT_{3A}R$-Salipro-Apo EM map, which could potentially correspond to a fatty acid chain (**Figure 3.20** E). These findings suggest that the lipid can only (fully) enter upon conformational changes in the TMD in response to gating, stabilising the open-pore conformation. Indeed, the inter-subunit TMD cavity is a well-documented site for allosteric modulation of pGLICs (Taly et al., 2014), and inter-subunit lipid binding was shown to lead to expansion of the pore and potentiation of agonist binding in GluCl (Althoff et al., 2014).

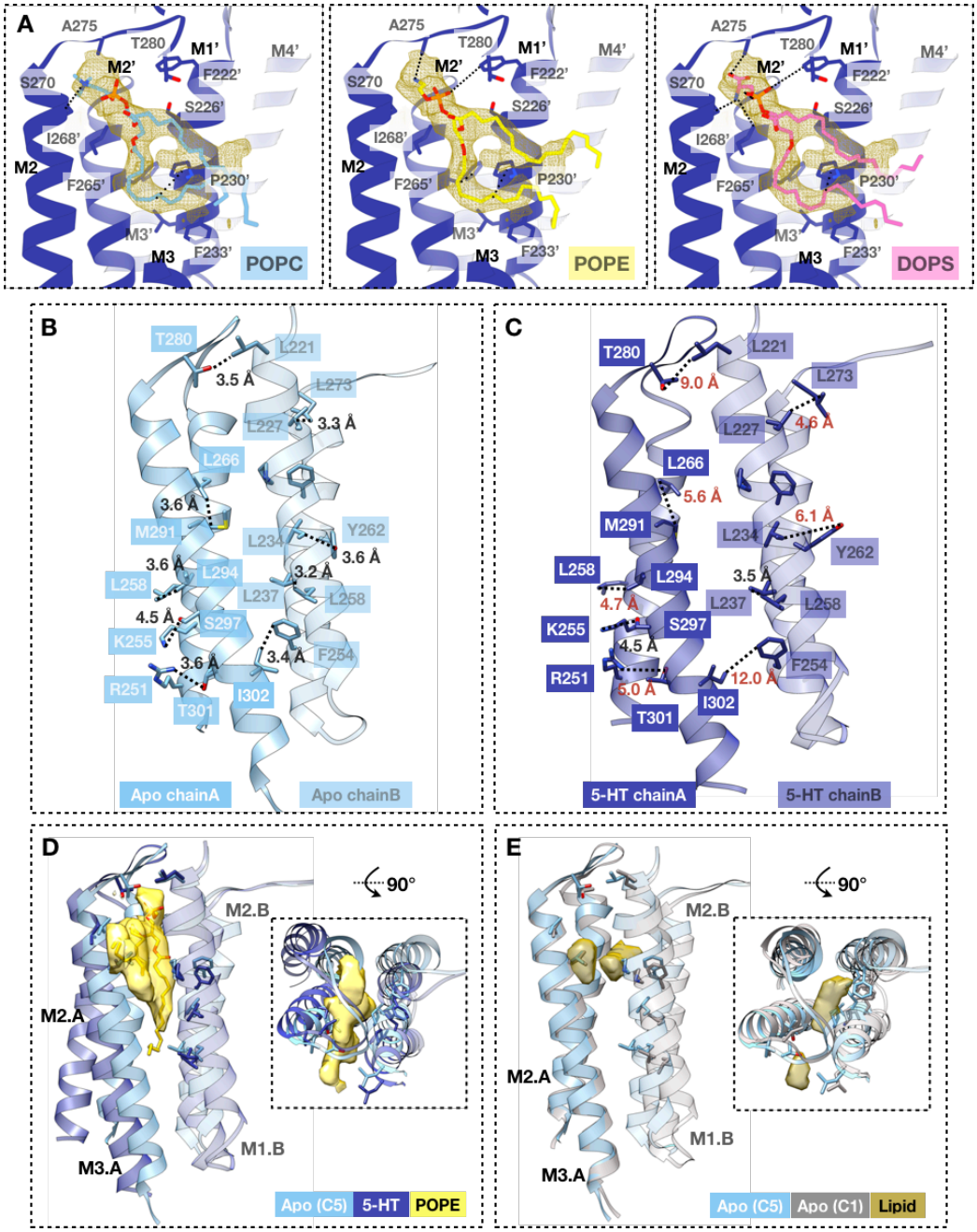

Figure 3.20 Lipid modulation at inter-subunits. (**A**) Tentative modelling for inter-subunit phospholipid-like density (transparent dark yellow, contoured at σ 2.0) of serotonin-5HT$_3$R-Salipro EM map; POPC (left), POPE (middle), DOPS (right). The M3 helix (of the left subunit) is hidden at residue P281-L293 for clarity. (**B**) The inter- and intra-subunit interactions of chain A/B at the TMD inter-subunit lipid

binding pocket of the symmetric Apo conformation (lipid density observed in the $5HT_{3A}$R-Salipro-5HT map only). (**C**) The broken inter- and intra-subunit interactions upon serotonin binding of Salipro-$5HT_{3A}$R activation are shown here in red at the TMD inter-subunit lipid binding pocket for the $5HT_{3A}$R-Salipro-5HT conformation. (**D**) Superposition of $5HT_{3A}$R-Salipro-Apo-C5 and $5HT_{3A}$R-Salipro-5HT chain A/B at TMD domain showing inter-subunit pocket enlargement upon activation, with Density corresponding to the inter-subunit lipid in transparent yellow (σ 2.0, here tentatively modelled as POPE) in the $5HT_{3A}$R-Salipro-5HT inter-subunit pocket. (**E**) Weak density (transparent dark yellow, σ 1.0) in Apo-C1 map seated in between subunits A and B. In panels (**B-E**), helices M2 and M3 are show for chain A (left chain), and helices M1 and M2 are shown for chain B (right chain), as indicated in panel (**D**) and (**E**).

Table 3.5 Lipid headgroup composition of $5HT_{3A}$R-Salipro. Lipid species extracted from $5HT_{3A}$R-Salipro and empty saposin discs as determined by lipidomics analysis grouped by their headgroup species. The lipid content is normalised to molar amount of protein present (top) and to molar amount of protein present as well as the total lipid content (bottom). Enrichment gives the factor by which the molar ratio of each lipid species differs in $5HT_{3A}$R-Salipro relative to empty saposin discs; none of the lipid species shows strong positive enrichment in the receptor-containing discs compared to the empty discs. Results represent an average of three biological replicates and the standard deviation is given. Abbreviations: PC, phosphatidylcholine; PE, phosphatidylethanolamine; PS, phosphatidylserine; PI, phosphatidylinositol; Chol, cholesterol; LPC, lyso-PC; SM, sphingomyelin; Cer, ceramide.

	Lipid/protein (mol/mol)	
	$5HT_{3A}$R-Salipro	**Empty saposin discs**
PC	14±6	0.7±0.2
PE	7±2	0.5±0.1
PS	7±2	0.4±0.1
PI	4±3	0.16±0.10
Chol	19±8	1.0±0.4
LPC	0.06±0.02	0.028±0.009
SM	1.2±0.3	0.06±0.02
Cer	0.06±0.03	0.0023±0.0007

	Molar ratio (%)		**Enrichment**
	$5HT_{3A}$R-Salipro	**Empty saposin discs**	
PC	30±10	30±7	1.0±0.5
PE	13±5	18±4	0.8±0.3
PS	14±4	13±3	1.0±0.4
PI	8±6	6±3	1±1
Chol	40±20	30±10	1.0±0.6
LPC	0.12±0.03	1.0±0.3	0.12±0.05
SM	2.3±0.7	2.0±0.6	1.2±0.5
Cer	0.11±0.05	0.08±0.03	1.3±0.7

Table 3.6 TMD inter-subunit cavity. Volume of the TMD inter-subunit cavities for the $5HT_{3A}R$-Salipro-Apo forms (C5 and C1) and $5HT_{3A}R$-Salipro-5HT form (5-HT) as calculated by CASTp (Tian et al., 2018) analysis using a 1.4 Å probe sphere. For the asymmetric conformations, the size of each of the five pockets between the indicated chains is given.

Conformation	Subunits	Volume ($Å^3$)
Apo C5	-	177
Apo C1	A/B	428
	B/C	67
	C/D	352
	D/E	117
	E/A	40
5-HT	A/B	1001
	B/C	347
	C/D	1198
	D/E	702
	E/A	310

3.5 Comparison between the C1 asymmetric Apo- and open states

To better understanding the role of the C1 asymmetric $5HT_{3A}$R-Salipro-Apo form, it is better comparing it directly to the asymmetric $5HT_{3A}$R-Salipro-5HT open form (**Figure 3.21** A).

As the opening of the C5-symmetric $5HT_{3A}$R-Salipro-Apo (**Figure 3.21** B), similar clockwise rotations (relative to the pore axis) and translations (away from the pore axis) of the individual subunits are required upon channel opening. Chain D of the C1-asymmetric $5HT_{3A}$R-Salipro-Apo conformation, which shows the largest displacement compared to the $5HT_{3A}$R-Salipro-5HT open conformation, also shows the largest displacement to the C5-symmetric $5HT_{3A}$R-Salipro-Apo conformation.

From Apo to open, the summed displacements of the twenty TM helices at the 9' position (L260, one of the most constrain site) are found very similar (85 Å and 85.9 Å for the C1-asymmetric $5HT_{3A}$R-Salipro-Apo and C5-symmetric $5HT_{3A}$R-Salipro-Apo conformations, respectively). And another common feature is that the M2 helices for both $5HT_{3A}$R-Salipro-Apo forms response the most to the channel opening (31.6 Å and 30.8 Å), then M1 helices are ranking the second most (26.2 Å and 23.8 Å).

Based on this static comparison, the position of this C1-asymmetric Apo state in the activation trajectory $5HT_{3A}$R-Salipro relative to the C5-symmetric Apo state and the open state is unclear. Thus, we performed MD simulations, done by the collaboration with Dr. Shuguang Yuan and Dr. Rongfeng Zou, on all our three $5HT_{3A}$R-Salipro structures. The results suggested that the C1-asymmetric $5HT_{3A}$R-Salipro-Apo state represents an intermediate conformation between the C5-symmetric $5HT_{3A}$R-Salipro-Apo and the serotonin-bound state.

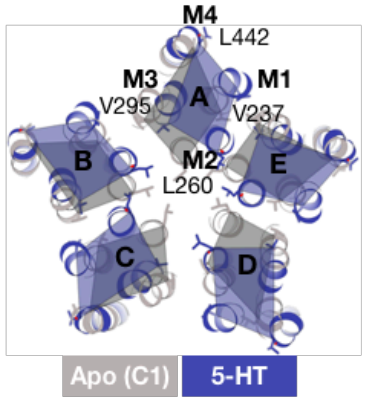

Apo-C1	M1	M2	M3	M4	Rotation to Open
Chain	V237	L260	V295	L442	
A-A	5.2 Å	7.0 Å	4.5 Å	2.0 Å	14.0°
B-B	4.2 Å	4.2 Å	2.5 Å	1.8 Å	7.7°
C-C	4.3 Å	6.9 Å	3.8 Å	1.1 Å	17.9°
D-D	8.3 Å	8.1 Å	3.3 Å	4.0 Å	22.2°
E-E	4.2 Å	5.4 Å	2.8 Å	1.4 Å	15.1°
Sum	26.2 Å	31.6 Å	16.9 Å	10.3 Å	/
		85 Å			

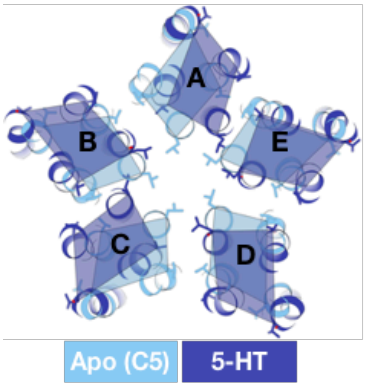

Apo-C5	M1	M2	M3	M4	Rotation to Open
Chain	V237	L260	V295	L442	
A	4.7 Å	7.7 Å	4.5 Å	1.3 Å	19.7°
B	5.0 Å	5.1 Å	3.9 Å	4.2 Å	12.3°
C	5.1 Å	8.3 Å	5.1 Å	1.6 Å	21.1°
D	4.8 Å	4.7 Å	2.7 Å	2.8 Å	10.5°
E	4.2 Å	4.7 Å	3.1 Å	2.1 Å	10.6°
Sum	23.8 Å	30.8 Å	19.3 Å	12.0 Å	/
		85.9 Å			

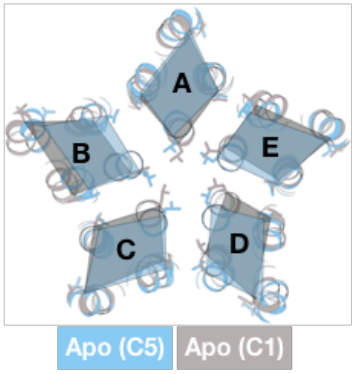

Apo-C1	M1	M2	M3	M4	Rotation to Apo-C5
Chain	V237	L260	V295	L442	
A-A	0.7 Å	1.9 Å	1.0 Å	1.0 Å	1.0°
B-B	2.7 Å	2.8 Å	3.4 Å	3.2 Å	5.9°
C-C	1.1 Å	1.8 Å	1.4 Å	0.6 Å	2.8°
D-D	3.5 Å	3.8 Å	1.5 Å	1.6 Å	0.3°
E-E	0.5 Å	1.9 Å	2.2 Å	0.7 Å	1.5°
Sum	8.5 Å	12.2 Å	9.5 Å	7.1 Å	/
		37.3 Å			

Figure 3.21 Cross section of the TMD at L260, 9' position of M2 for C5-symmetric $5HT_{3A}R$-Salipro-Apo (light blue, Apo (C5)), C1-asymmetric $5HT_{3A}R$-Salipro-Apo (grey, Apo (C1)), and $5HT_{3A}R$-Salipro-5HT (dark blue, 5-HT open). The table gives displacement measured at the Cα atoms of residues on each helix in the same cross section. Superposition that minimises the summed RMSD is shown.

Firstly, its M2 helices were more flexible than those of the C5-symmetric Apo state but less flexible than the serotonin-bound state, and adopted a slight “A” shaped bending at the intracellular end as observed for the serotonin-bound receptor, albeit less strongly (**Figure 3.22** A, B), comparing to C5-symmetric Apo which M2 helices adapted a “H” shaped bending. Secondly, the Apo-C1 state showed a slightly more hydrated channel than the Apo-C5 state (**Figure 3.11**). Thirdly, as previously shown, to investigate the capacity for channel opening of both $5HT_{3A}$R-Salipro-Apo forms, five serotonin molecules were placed in the LBPs of each model, and 3x200 ns all-atom MD simulations were performed. Analogous simulations were performed for the crystallised detergent-solubilised Apo structure (PDB-4PIR) (Hassaine et al., 2014). Slightly more hydration was seen for the serotonin-docked $5HT_{3A}$R-Salipro-Apo-C1 form (**Figure 3.12**).

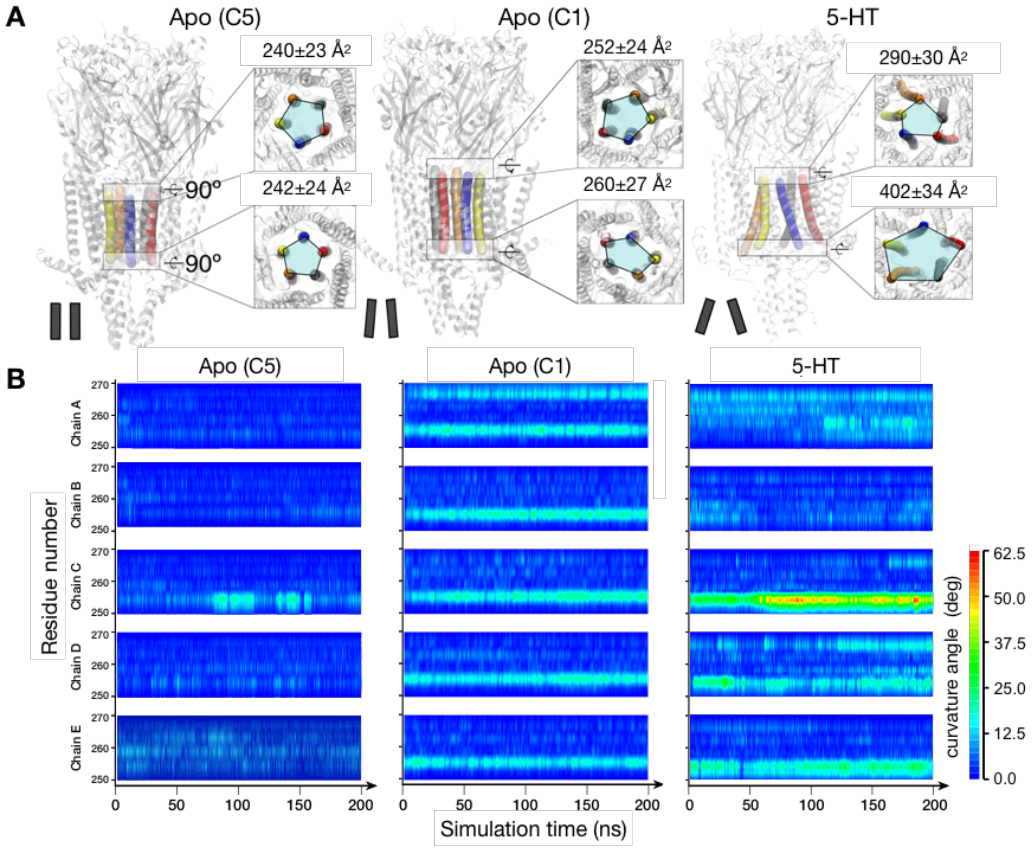

Figure 3.22 MD simulations suggest Apo (C1) having its M2 helices more flexible than Apo (C5) with evidences on (**A**) transmembrane cross section area at I268 (upper panels) and V252 (lower panels), and (**B**) M2 helices curvature.

Applying cryo-SPA structural characterisation, we address the lack of mechanistic understanding on both channel gating and lipid modulation, by presenting structures of the receptor reconstituted in saposin-based lipid bilayer in the presence and absence of agonist.

Using complementary non-constrained molecular dynamics (MD) simulations, we are able to show that our new lipid-embedded receptor structure in the serotonin-bound form represents an open channel form allowing free diffusion of sodium ions across the membrane. In contrast, we did not observe pore wetting or ion conductance in simulations for the previously published serotonin-bound detergent-solubilised structures under similarly unbiased simulation conditions.

Furthermore, our structures solved in presence of lipids show a number of substantial differences compared to the previously reported detergent-solubilized structures and provide a framework to explain receptor gating. In the lipid bilayer, the outer transmembrane helices show a displacement of more than 10 Å compared to their position in detergent. Based on detailed analysis of the structural differences between our new structures, which included several partially resolved lipid molecules, and previously reported detergent-solubilized structures, we are able to propose a mechanism by which the membrane environment modulates the structure and function of 5-HT_{3A}R, which will be discussed in Chapter 4. Importantly, due to the highly conserved residues involved in the proposed mechanism of lipid modulation, our findings can be generalised to other pLGICs.

3.6 Cryo-ET and STA application on native $5HT_{3A}R$-microvesicles

To address the lipid modulation on the allosteric transition of $5HT_{3A}R$, cryo-ET combined with sub-tomogram averaging (STA) is another approach. On one hand, the resolution of STA is in molecular level which would potentially help to identify lipid modulation on receptor conformations. On the other hand, comparing to cryo-SPA analysis, the tomograms are collected on the protein inserted membrane vesicles. The membrane environment could be provided by reconstituting purified protein back into liposomes, or by directly collecting from protein inserted native membranes. In the former case, membrane environment could be designed aiming of understanding allosteric effect of particular phospholipids and steroids, and in the latter case, it is powerful for providing information close to native, while it could be more challenging as processing requires further steps such as classification due to a high sample heterogeneity.

In our study, we used the natively derived vesicles with receptors embedded, which is without the needs of doing receptor purification and reconstitution.

3.6.1 Conventional cryo-ET and STA application for native $5HT_{3A}R$-microvesicles

We applied the conventional cryo-ET and STA of the serotonin receptor in native micro-vesicles ($5HT_{3A}R$-MVs) as a proof of principle.

In the slice of the reconstructed tomogram (**Figure 3.23** A), the native micro-vesicles could be seen with various size and shape. The tiny shaded black densities are protein inserted, mostly expected to be our serotonin receptor and in a mixture with some of other protein complexes unknown, as lacking of purifying. The membrane surfaces were defined manually and vectors were generated perpendicular to the surface of the membrane with fixed step in pixel for particle picking in Dynamo (Castano-Diez et al., 2012). About 15,000 particles were picked from 16 tomograms (pixel size at 4.4 Å/pixel). As the non-uniform distribution of particle insertion, the sub-boxing volume contained many empty vesicles. The STA class average displayed (**Figure 3.23** B) in comparing with SPA structure, was reconstructed with the best 20 percent of the picked particles. And the overall architecture agreed well with the SPA structure of $5HT_{3A}R$-Salipro in the ligand-free Apo conformation.

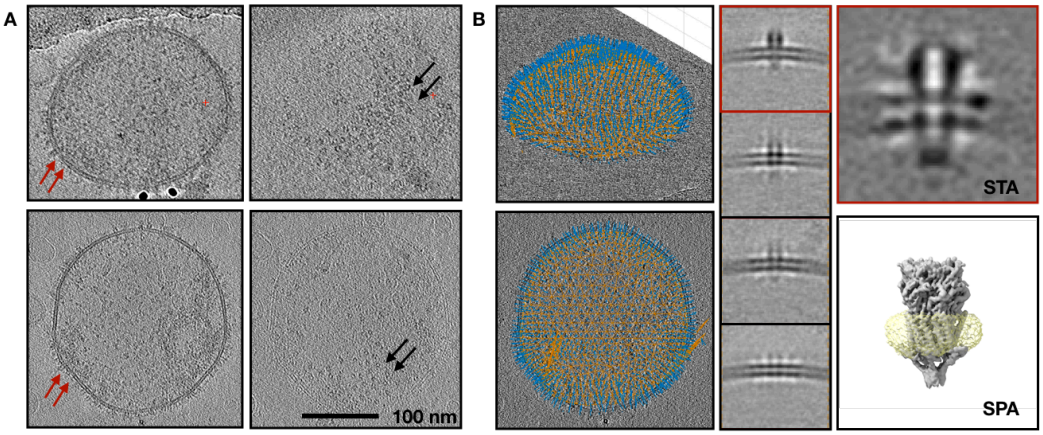

Figure 3.23 Conventional cryo-ET and STA of native $5HT_{3A}R$-microvesicles. (**A**) tomogram slices of two $5HT_{3A}R$-MVs at different height, red and black arrows indicating side and top views of protein inserted, accordingly. (**B**) Sub-boxing of protein on manually drew surfaces (blue) of micro-vesicles in Dynamo (Castano-Diez et al., 2012) (left, vector in orange represents particle orientations). Multi-references alignment of particle sub-boxes (middle). The STA class average representing the membrane inserted receptor (right-top), in comparing to the SPA architecture of 5HT3AR in reconstituted Saposin-lipid disc (right-bottom, grey as receptor, yellow as Saposin-lipid disc). Red squares indicate the enlarged same class.

The low resolution (~4 nm) is mainly resulted from the limited number of particles. However, in general, cryo-ET and STA have intrinsic bottlenecks as the way it is performing now (Section 3.6.2), but also, highly affected by the heterogeneity of the EM specimen:

a. Size and shape of the vesicle varies over the ice, with also non-uniform distributed protein insertion;

b. Native vesicles including different types of proteins. Continue classification on the STA results wasn't success in the separation of $5HT_{3A}R$ from the others.

c. Lager dataset with more particles are required to get better resolution. The previous published cryo-ET and STA of $5HT_{3A}R$ reconstituted in lipid vesicles revealed a 12Å resolution structure from 31,000 extracted particles (Kudryashev et al., 2016).

3.6.2 Bottlenecks of conventional cryo-ET and STA

Conventional STA, typically still limited at ~3-4 nm resolution, due to quite a few limitations, makes achieving better resolution challenging. These limitations have been well documented and discussed:

a. Poor signal-to-noise ratio per 2D projection, due to the distribution of the limited total electron dose (typically 60-120 $e^-/Å^2$ over 40-60 2D projections), reducing the precision of defocus determination.

b. Beam-induced specimen non-uniform movements (Brilot et al., 2012), up to several nanometers during a typical tomogram recording, estimated on a cryo-SPA work (Li et al., 2013). Rather than recording a rigid object, tomogram records a continuous changing object.

c. Gold fiducial alignment (Fernandez et al., 2019) for local movement correction usually requires manually input, which is very time-costly and still not a-hundred-percent precise, as the gold fiducials behavior under beam irradiation is not perfectly the same as that of the specimen, which contributes to the sub-optimal aligning of tilt stacks. Better resolution is possible to achieved by improvement on refined orientation accuracy with geometric constrain (Himes and Zhang, 2018).

d. Increased effective specimen thickness in severity during tilting, introducing additional CTF correction errors. A 250 nm error limits the maximum achievable resolution to approximately 10 Å of a 300 kV microscope (Kudryashev, 2018).

e. Moreover, a significant amount of dataset in good quality is the fundamental of better resolution. Collecting at higher magnification is lower throughput, takes too much machine-time (a couple of days) to collect enough dataset, but more than that time is currently not easily-accessible for the majority of users in most of the EM facilities. Combining dataset from different sessions may have effect on data quality and the beam condition/settings may change after time. While, Imaging at lower magnification provides better throughput, however is in payment of limited data quality (Leigh et al., 2019) and suffering from low magnification distortions (Grant & Grigorieff, 2015). Pushing its resolution better than 10 angstroms and resolving secondary structural elements of STA is still of great interest, as the underling architecture with specific functional-related structural

information of the protein complex are in their native context (Kovtun et al., 2018; Wan et al., 2017).

3.7 A proposed hybrid SPA-STA workflow aiming at higher resolution for cryo-ET and STA

3.7.1 Hybrid SPA-STA workflow for higher resolution of cryo-ET and STA resolved structures

To overcome all the bottlenecks as mentioned and other potential limitations in one goal for better resolution of cryo-ET and STA is quite ambitious and challenging, we proposed a solution, with benefits from the current available advanced single particle analysis (Section 1.5.1) with advantages of conventional STA workflow (Section 1.5.2), aiming on solving most of the bottlenecks and achieving higher resolution in sub-nanometer level. We refer it the combined solution as hybrid-SPA-STA workflow in the text.

The hybrid SPA-STA workflow (**Figure 3.24**) uses modified dose-symmetric scheme (Hagen et al., 2017):

a. 2D projection collected at zero-degree tilt is applied with a total electron dose around 15-30 $e^-/Å^2$, much higher than untilted projection in the conventional tilt series. The rest available electron doses are equally distributed among all the following 2D projections of the tilt series (**Table 3.7**). The optical setting stays the same, with only long exposure time (a few more seconds of exposure time) taken.

b. Before tilt-stack aligning, the untilted 2D projection of the hybrid workflow needs to be normalized with all the rest of the projections into the same mean value and standard deviation.

c. On the incorporated tilt-stack, tilt stack aligning, tomogram reconstruction, sub-volumes boxing and subtomogram averaging are performed as the conventional workflow. At this step, every sub-volume with its apparent coordinates should have its stable refined orientations (rotation and shift) available, according to the STA resulted 3D reconstruction. They are standard output as table created by Dynamo.

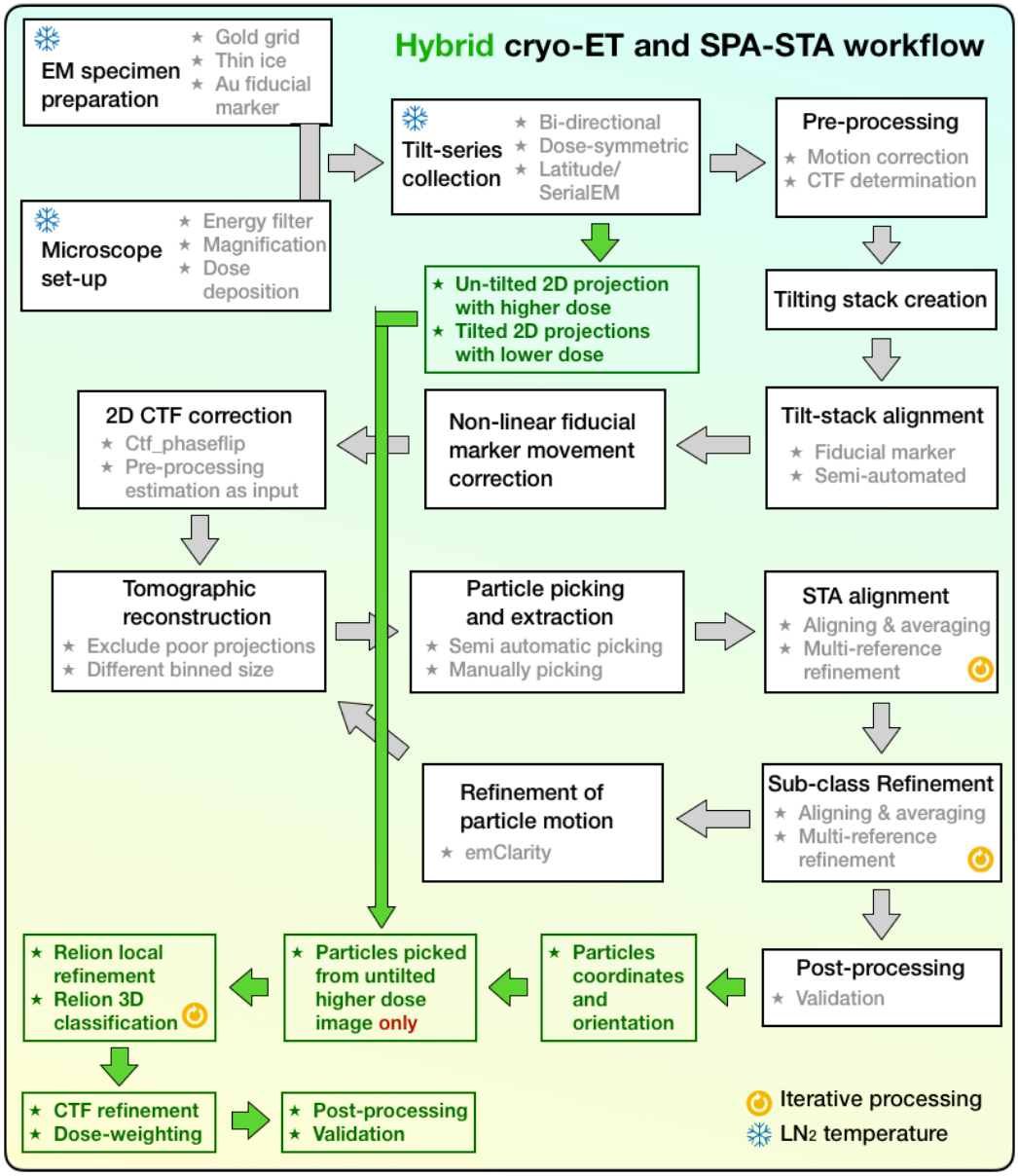

Figure 3.24 Hybrid SPA-STA workflow. The text and arrows in green indicate the steps involved in combination and conducting of SPA with conventional cryo-ET combined STA. Iterative processing steps are indicated in yellow symbol.

Table 3.7 Electron dose re-distribution over the tilt series for hybrid workflow.

Electron dose per 2D projection ($e^-/Å^2$)		
2D projection	***Conventional***	***Hybrid***
0 (untilted)	2	**20**
1-40 (tilted)	2	1.55
Total dose	82	82

d. With the coordinates and orientations of the particles derived from STA, creating particle stacks and performing the 3D reconstruction only from the untilted "high dose" 2D projection using RELION (Scheres, 2012). Further local refinement of the positions and orientations of particles against the resulting structure are performed using standard SPA workflow.

e. Moreover, 3D classification, CTF refinement and particle polishing are optional with standard SPA workflow, which potentially help dealing with flexibility and heterogeneity of specimen, and could further improve the resolution. Since the last two step involving refinement on 2D projections instead of 3D volumes, the machine-time spend on calculation is much shorter.

3.7.2 Hybrid SPA-STA workflow: proof of principle on Tobacco Mosaic Virus (TMV)

The hybrid SPA-STA workflow was tested on cryo electron tomograms of tobacco mosaic virus (TMV) recorded at 64,000 x magnifications of electron microscope at super-resolution mode with calibrated pixel size at 1.1 Å. As a proof of concept, with application of the hybrid STA-SPA workflow at this magnification, it should be capable enough to achieve sub-nanometer resolution, and provide more particles per tomogram. As **Figure 3.25** shown, CTF estimation of the untilted projection in the hybrid tomogram presents is more accurate with the facilitating

by the better visible Thon rings. While on the other hand, it means the dose of the other tilted projections would have even less electrons compared to the conventional tomograms, whether or not it would affect the reconstruction of the tomogram we would have to test.

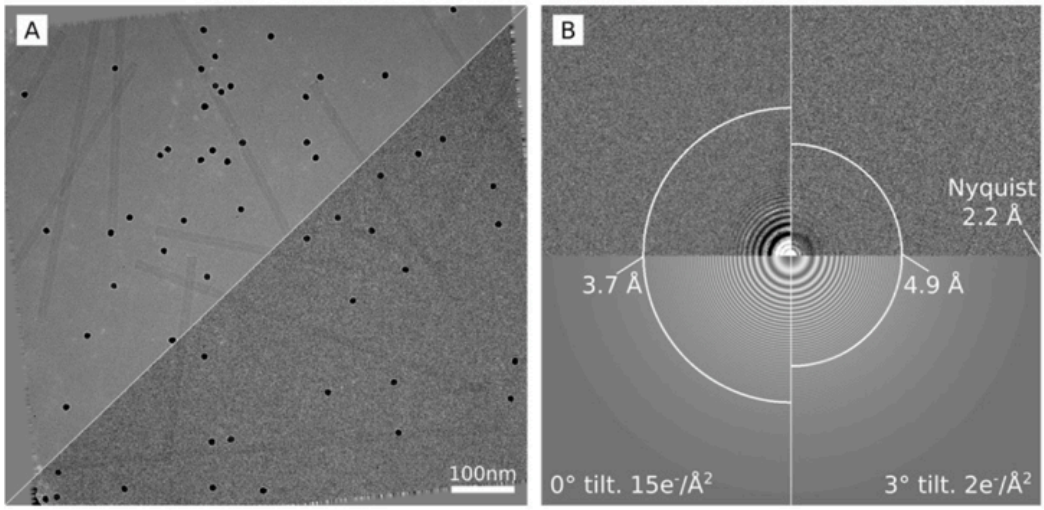

Figure 3.25 Hybrid tomography at untilted projection presents better visible Thon rings facilitating CTF determination. (**A**) Aligned 0° untilted projection and 3° tilted projection of a hybrid tomogram. (**B**) CTF determination for projections of (A). Higher dose applied to the untilted projection, presenting more accurate CTF estimation.

Thus, to access any difference/drawbacks may exist resulting from the unevenly distributed dose across the hybrid tomogram 2D projections, both workflows were taken to collect the conventional and hybrid tomograms with a same total electron dose (~95 $e^-/Å^2$). Sub-tomogram averaging was performed using identical parameter settings with applied the same helical symmetry parameters, with numbers of asymmetric units extracted from conventional and hybrid tomograms as 4,570 and 4,190, respectively. The STA reconstructions are at the resolutions of 9.8 Å and 10.0 Å for conventional and hybrid tomograms, respectively (**Figure 3.26**). The similarity in resolution for the conventional and hybrid tomograms suggests that there are no observed drawbacks to collect tomograms using the hybrid workflow and process with conventional STA.

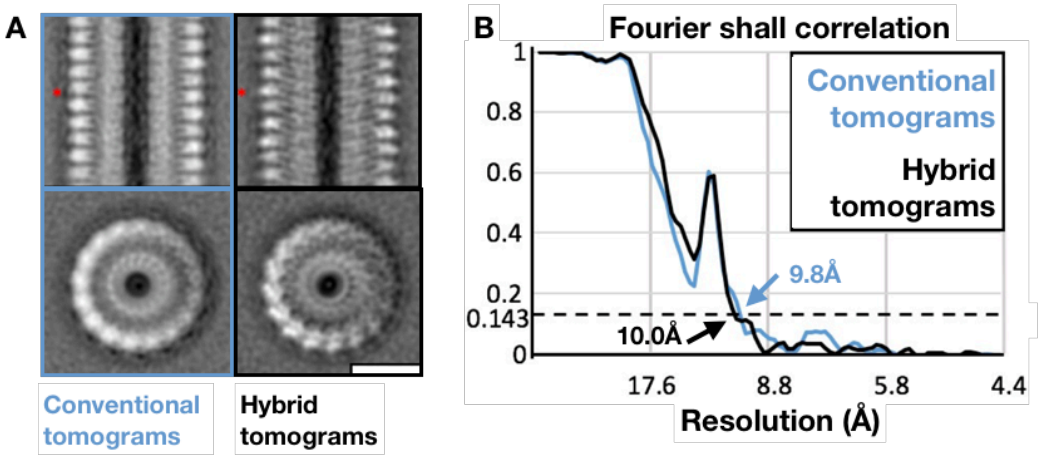

Figure 3.26 Conventional STA for normal tomograms and hybrid tomograms. (**A**) STA structures for conventional tomograms and hybrid tomograms. Scale bar: 100 Å. (Red dot indicates “halos”-like features which is typical a cryo-EM case (Sindelar and Grigorieff, 2011)). (**B**) FSC plot of the two reconstructions in (A).

Notably, 3D volume of the conventional STA showing some “halos”-like features around the TMV EM density (**Figure 3.26** A, marked with red dot). These “halos” are considered to result from an inaccurate summation of images of isolated particles surrounded by featureless background, which is typical a cryo-EM case, and could be optimized during reconstruction from 2D projections with the use of Wiener filter (Sindelar and Grigorieff, 2011).

Next another 4 hybrid tomograms were collected using a Titan Krios G2 equipped with a Gatan K2 detector by Lea Diethirch with collaboration. Conventional STA as mentioned, on 20,021 asymmetric sub-volumes, generated a 3D volume at 7.2 Å resolution. Taking the orientations and stable alignments from conventional STA output, a reconstruction was calculated by RELION only with the particle stacks cropped from the untilted images. The output 3D volume had a resolution at 7.5 Å. Local refinement was then applied following SPA workflow using RELION, the local refined final structure after postprocessing reported a resolution at 5.2Å (**Figure 3.27**), showing clearly alpha-helical secondary structure (**Figure 3.27** A, right). This resolution corresponds to ~85% of the Nyquist frequency. Hybrid reconstruction on unbinned particle stacks (1.1 Å/pixel) followed with local refinement didn’t produced better reconstruction, means that the bin2 particle stacks (2.2 Å/pixel) was able to achieve the same resolution with

these number of particles, compared to unbinned particle stacks. In this case, magnification is not a limiting factor to achieve higher resolution.

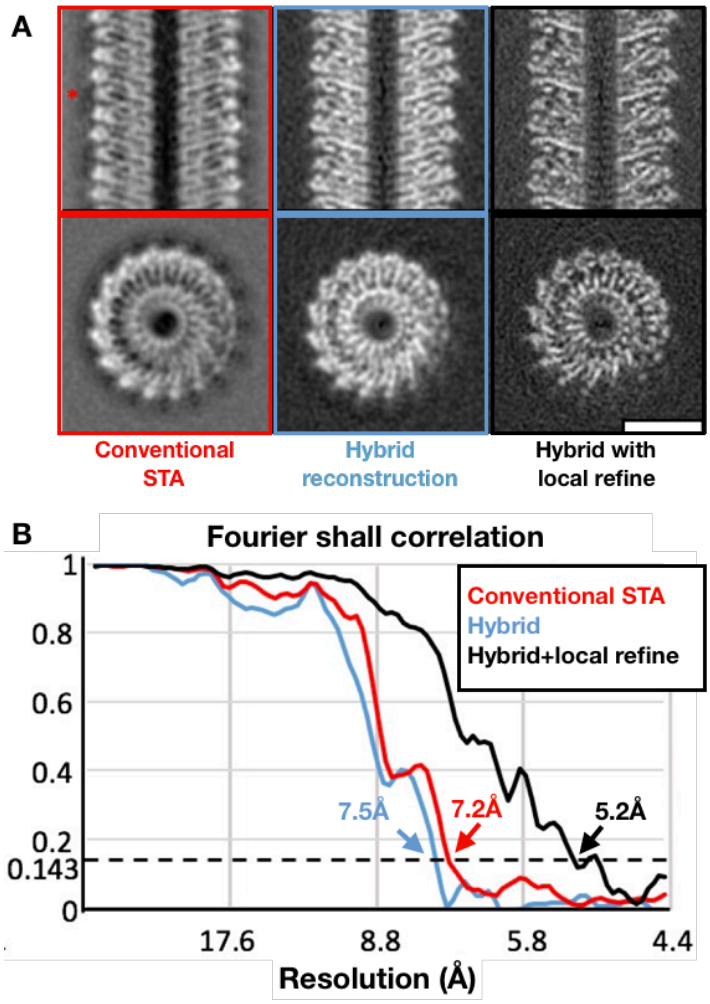

Figure 3.27 TMV hybrid tomograms processed with conventional workflow and hybrid SPA-STA workflow. (**A**) conventional STA map of hybrid tomograms using Dynamo (left, conventional); and using hybrid workflow: map reconstructed only using particles cropped from untilted higher dose projections (middle, hybrid), and hybrid map after local refinement in RELION (right). Scale bar: 100 Å. (Red dot indicates “halos”-like features which is typical a cryo-EM case (Sindelar and Grigorieff, 2011)). (**B**) FSC plots of the three maps in (A).

Applying the hybrid tomographic SPA-STA workflow on TMV sample, the final achieved resolution is much higher than the conventional STA, 5.2 Å and 9.8 Å, respectively.

The collecting of the hybrid tomographic tilt-stacks, well-implemented in SerialEM script (Appendix I), is rather straight-forward to manipulate, did not require any extra work or make the data collection complicate. It is a very general approach that suitable for all types of cryo-ET studies.

Furthermore, the hybrid SPA-STA method takes 2D images as input for additional local refinement and/or 3D classifications, which is computationally cheaper and faster. Besides, these refinement and classification steps use the well-developed SPA packages, which is very flexible and robust.

3 Results

Chapter 4 Discussions

In this Chapter, we discussed first in Section 4.1 and 4.2 on our observation from cryo-SPA resolved 3 different structures in the absence and presence of its native agonist serotonin, and their MD simulations of the serotonin receptor in lipid bilayers, (related to the results from Section 3.1 to 3.5). With our results, we could now reconstruct the activation sequence and suggest a mechanistic model for receptor activation (Section 4.2).

Following that, in Section 4.3 (related to the results from Section 3.6 to 3.7), we will discuss about the hybrid SPA-STA tomographic workflow as a general approach, could benefit other tomographic research in principle, as demonstrated with TMV.

4.1 Asymmetric Apo form of homopentameric $5HT_{3A}R$, an intermediate state towards activation

Firstly, the resolving of the two Apo conformations of the homopentameric $5HT_{3A}R$ suggests, the serotonin receptor appears to display a conformational equilibrium between symmetric and asymmetric forms (without the presence of ligand), in accordance with the classical Wyman-Monod-Changeux (WMC) model of allostery. In our dataset, we have 39% of the particle set contributes to the asymmetric Apo form. According to the WMC model, the major population of symmetric structures might have a lower affinity for serotonin than the minor population of asymmetric structures, means serotonin binding on asymmetric Apo form could then ultimately be favoured resulting in a major asymmetric open structure. It remains an interesting matter for future studies whether the asymmetric and symmetric form indeed show different affinities for serotonin.

The MD simulations observed the C1 asymmetric Apo state showed a slightly more hydrated channel than the C5 symmetric Apo state (**Figure 3.10**), also with docking of serotonin molecules (**Figure 3.12**), suggesting it may represent an intermediate, more readily activated state.

Based on potential energy calculations from the MD simulations (in the absence of added ligands), the C5 symmetric Apo conformation (-9,710±20 Kj/mol)

represents a more stable state than the C1 asymmetric conformation (-6,380±20 Kj/mol), in line with the higher proportion of particles in our cryo-EM data set adopting this conformation. The asymmetric serotonin-bound conformation (-6,930±20 Kj/mol), was slightly more stable than the C1 asymmetric apo conformation, although it has to be noted that the atom numbers in each simulated system were different (as the system contains water, ions, lipids, protein complex and ligands) which might result in some artefacts in the potential energy calculations, but the differences are quite large to distinguish the C1 asymmetric Apo from the other ones. Furthermore, we did not see any interfacial lipids adopting conformation similar to those observed in our EM maps, most likely due to the simulation time (200 ns) being too limited to allow any significant lipid diffusion. Thus, potentially stabilising effects of interfacial lipids are most likely not accounted for here.

4.2 Lipid allosteric modulation on ligand-gating of $5HT_{3A}R$

4.2.1 Lipid order

Lipid order parameter (-SCD) presented in **Figure 4.1** was calculated for phospholipids during the MD simulations of $5HT_{3A}R$-Salipro conformations for the different carbon atom positions along the fatty acid chain. Indicated by the calculation, annular lipids were more ordered in simulations of the Apo forms than of the serotonin-bound form of $5HT_{3A}R$-Salipro. This could be because the allosteric transition behavior like bending/tilting of the M2 helices in the $5HT_{3A}R$-Salipro-5HT form are much more significant than that of the Apo forms (**Figure 3.22**) during receptor activation. And in consequence, the transition at TMD induces an additional overall tilting of lipid hydrocarbon chains reducing the lipid chain order parameters. Conversely, as cholesterol is known to increase lipid order (Yeagle, 1985), such lipid membrane properties might influence tilting of TM helices in pLGICs thereby modulating channel gating.

While, looking only at the lipid order parameter between the two Apo forms, it is hard to address the reason why annular lipid surrounding C5 asymmetric $5HT_{3A}R$-Salipro-Apo is least stable than that of the C1 symmetric $5HT_{3A}R$-Salipro-Apo. It could be affected by the limited simulation time or the lipid partitioning in the simulations, which needs to be further considered.

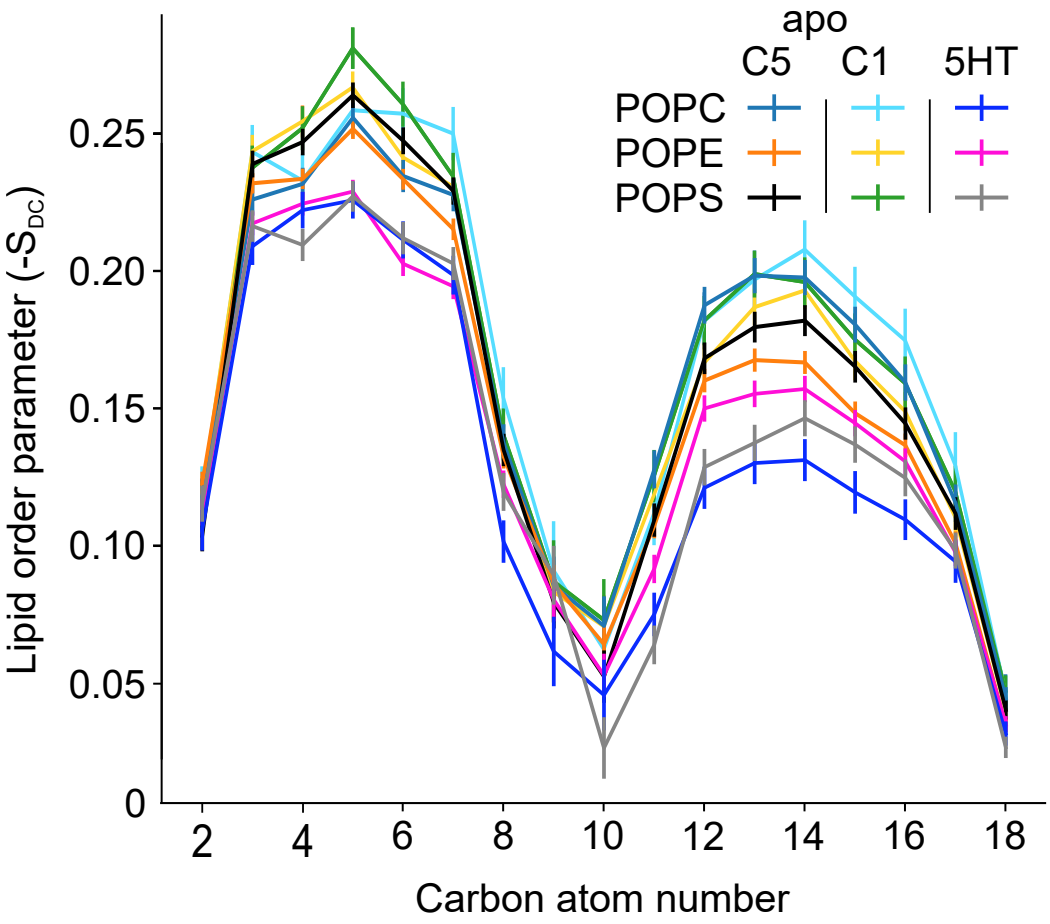

Figure 4.1 The lipid order parameter ($-S_{CD}$), was calculated for phospholipids in simulations of C5 $5HT_{3A}$R-Salipro-Apo (teal, orange, black), C1 $5HT_{3A}$R-Salipro-Apo (cyan, yellow, green), and Salipro-5HT (blue, magenta, grey, for POPC, POPE and POPS, respectively) for the different C atom position along the fatty acid chain. The order parameter indicates that the annular lipids surrounding the Apo receptors (C5 and C1) are more ordered than those surrounding the serotonin-bound receptor.

4.2.2 Plasticity of the open state

The open $5HT_{3A}$R-Salipro conformation is asymmetric as described in Chapter 3, mostly in the TMD and ICD (**Table 3.4**). Considering the highly similar conformation of the ECDs of the different subunits, there is no clear chemical determinant for the asymmetry observed in the TMD of the fully ligand-bound $5HT_{3A}$R-Salipro open form. Single channel recordings of an α7-nAChR/$5HT_3$R chimera have shown that binding of two ligands at non-consecutive sites results in brief stable channel currents, and that three ligands bound at non-consecutive sites produce maximal mean open times (Rayes et al., 2009). Thus, we speculate that asymmetric opening may result from sequential ligand binding yielding sequential conformational changes stabilised by the introduction of inter-subunit lipids during the transition of each subunit from a resting to an activated conformation.

If indeed sequential ligand binding underlies the asymmetric opening of the channel, one might expect a large degree of conformational plasticity. To investigate any residual heterogeneity in the $5HT_{3A}$R-Salipro-5HT particle set, we performed symmetry expansion of the pentamer and 3D classification of the monomers (**Figure 4.2** A). The resulting monomer classes were compared to the different subunits of the $5HT_{3A}$R-Salipro-5HT model, and regrouped accordingly yielding two groups: “more” (M), and “less” (L) open, corresponding to modes 1 and 2 (**Figure 3.15**), respectively. Using this assignment, the corresponding pentamers were grouped based their composition of subunits in different states (M or L, **Figure 4.2** B). The largest group of particles (24%) fell into class “LMLML” corresponding to a pentamer containing two non-consecutive “more” open subunits, in agreement with the resolved consensus $5HT_{3A}$R-Salipro-5HT map. All other possible combinations were observed. Interestingly, classes containing non-consecutive “M”-subunits were more commonly found than classes containing the same number of “M”-subunits in a consecutive arrangement, paralleling the observation that non-consecutive ligand binding promotes receptor activation (Rayes et al., 2009). Thus, we propose that a conformational spectrum of asymmetric open states exists, while the resolved conformation represents the energetically most favourable form under our experimental conditions.

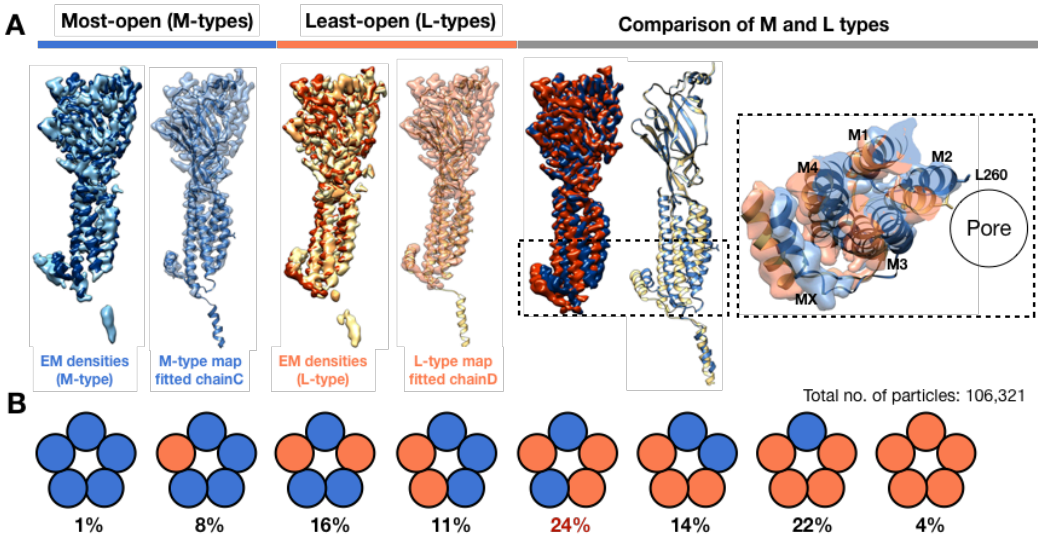

Figure 4.2 Conformational plasticity of serotonin bound $5HT_{3A}R$-Salipro state. (**A**) Classes resulting from symmetry expanded monomer-focused 3D classification were assigned as M- or L-type by finding the best fitting chains of the $5HT_{3A}R$-Salipro-5HT model: chain A/C fitted into EM densities of M-type classes (left, chain C is shown), chain B/D/E fitted into EM densities of L-type classes (middle, chain D is shown). Superposition of M and L-types and insert viewed from the ECD (right). (**B**) Schematic showing the population of the eight different combinations of $5HT_{3A}R$-Salipro-5HT arrangements; blue and orange circles represent M- and L-type subunits, respectively. The largest class agrees with the consensus serotonin-bound conformation.

4.2.3 A model of lipid allosteric-modulation on channel activation

In the ligand-free resting state, the serotonin receptor displays a conformational equilibrium between symmetric and asymmetric forms, with the asymmetric form potentially representing an intermediate state (**Figure 4.3**). Notably, several closed intermediate states have been postulated to describe single channel activation of acetylcholine and serotonin receptors (Auerbach, 2015; Bouzat and Sine, 2018). Furthermore, a recent in silico study of $5HT_3R$ reported asymmetric closed conformations which were attributed to sub-stoichiometric ligand occupation (Guros et al., 2020). The existence of asymmetric structural forms has also been detected for other pLGICs (Mowrey et al., 2013; Ruan et al., 2018; Zhu et al., 2018). For example, an asymmetric closed conformation has been solved by cryo-EM for the detergent-solubilised human tri-heteromeric α1β2γ2 $GABA_A$ receptor ($GABA_AR$) in the presence of its native agonist GABA and the antagonist flumazenil (PDB-6D6U) (Zhu et al., 2018). Interestingly, the authors also observed a 60/40 distribution between the resolved symmetric and asymmetric conformation. However, the asymmetric state resolved for $GABA_AR$ deviates significantly more from C5 symmetry than the C1 $5HT_{3A}R$-Salipro-Apo form; the γ2-subunit was observed to collapse into the pore, blocking the entire permeation pathway. Furthermore, the authors were cautious to interpret the structures in terms or their physiological relevance, in part due to the presence of detergent. Likewise, the observation of both a symmetric and an asymmetric $5HT_3R$-Salipro-Apo conformation is highly interesting, and broadens our understanding of the resting state of lipid-stabilised homopentameric $5HT_3R$.

Our MD simulations made by our collaborators suggest that there may be differences in the energy barrier to transition from either starting point to the activated state, as it has been postulated that unbalanced forces promote state transitions (Maksay, 2013). Activation of the unrelated pentameric prokaryotic magnesium transport protein CorA has also been shown to be asymmetric (Matthies et al., 2016). Thus, loss of symmetry may be a more general feature of ion channel activation. Nevertheless, the functional role of the two Apo forms for the transition to the asymmetric open channel structure remains to be solved in further detail aided by the high-resolution insights provided by our models.

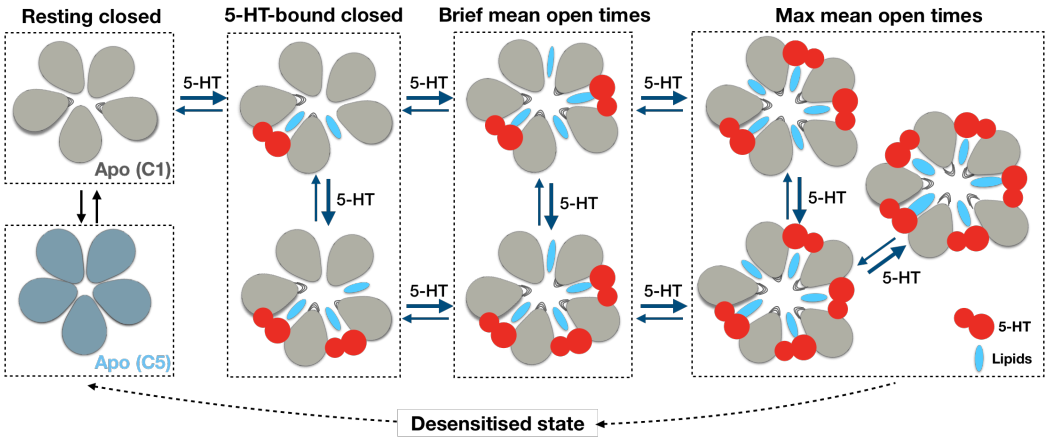

Figure 4.3 Hypothetic model for allosterically lipid-modulated asymmetric activation of $5HT_{3A}R$ upon serotonin binding. Various degrees of mean channel open times have been observed in response to different number consecutive/non-consecutive of ligands bound in single channel recordings (Rayes et al., 2009). In the ligand-free resting state, the serotonin receptor displays a conformational equilibrium between symmetric and asymmetric forms. We speculate that the asymmetric apo form represents an intermediate state, and that asymmetric opening may result from sequential ligand binding (5-HT shown in red) via this state yielding sequential conformational changes stabilised by the introduction of inter-subunit lipids (shown in light blue) during the transition of each subunit from a resting to an activated conformation. Considering that the channel already shows maximal mean open times upon binding three non-consecutive ligands, we postulate that five inter-subunit lipids are present to support the maximally open pore as observed in our saturated-bound open state structure. Thus, we hypothesise that one ligand binding event results in the introduction of two inter-subunit lipids as depicted (adjacent the principal and the complementary ligand-binding subunits). Pointy subunits indicate various conformations deviating from the C5-symmetric subunit arrangement; the principal serotonin-bound subunit is shown in blue.

4.3 Advanced hybrid-STA and its potential application on allosteric conformational study of pLGICs

The hybrid SPA-STA workflow for subtomogram averaging has demonstrated its ability of producing higher resolution structures than the conventional STA, with the benefits combined from advanced methods/tools developed for STA and SPA. At an intermediate magnifications of electron microscopes, sub-nanometer resolution STA could be achieved.

With the redistribution of the dose per projection, the CTF detection is more accurate. In the TMV dataset, approximate 15% of the total electron dose was contributed for the untilted 2D projection, while the fraction could be increased, depending on whether the ice is thick or the specimen is tiny. CTF estimation could be further refined as the conventional STA provides the tomographic geometry of the specimen embedded in ice and the orientations of the particles cropped. The STA alignment output could be readily imported into SPA workflow. They are quite reliable as the input of a local refinement. Time and computational costs are saved without global search and average of significant amount of particles in SPA.

Furthermore, the local refinement is an important step in hybrid SPA-STA workflow. It works with particle stacks cropped only from the higher dose untilted 2D projections, enables performing Wiener filtering improving the quality of density within the particle area, and makes the alignment more accurate without bothering on the polishing of tilting-stack alignment. For the structures poorly resolved due to a sub-optimal aligned tilt-stack (most likely either gold-fiducial tracking is not enough accurate or tomograms are collected without deposition of gold fiducials at all), hybrid SPA-STA would be useful. Besides, the hybrid tomography workflow for data acquisition can be readily combined with rapid tilt-series acquisition (Chreifi et al., 2019; Eisenstein et al., 2019) with its advantages on high throughput, so as to reduce the cost of microscope time spending on data collection.

In the preliminary test of TMV, there is no need to perform further classification on the particle stacks after local refinement in SPA workflow, because the sample showing little flexibility and heterogeneity. But one could imagine that this combined approaches would benefit significantly for the $5HT_3R$ in native micro-vesicles, of which the sample has great heterogeneity because of it contains other proteins.

The recent method TYGRESS (Song et al., 2019), presented by Song and colleagues shares the same idea of recording a higher-dose untilted image and refining the results of STA with SPA tools, however the implementations are sufficiently different:

a. TYGRESS does not take use of the untilted higher dose 2D projection for tomogram reconstruction or subtomogram averaging. In our implementation we introduce a normalization procedure which enables all the collected data to be used for particle alignment.

b. After conventional STA is finished, TYGRESS internally initiates a SPA project to refine the projections and get the high resolution map. In contrast, our method exports the output from conventional STA into a SPA project that can be further processed inside or outside of our pipeline potentially giving the user more flexibility.

c. The two methods are both implemented in Matlab, following different approaches. In TYGRESS, a PEET (Nicastro et al., 2006) project is refined using Frealign (Grigorieff, 2016) inside Matlab, using a set of configuration files and a GUI to execute the final refinement step. Our approach uses a minimal set of Matlab functions and classes to export a Dynamo project into a *star file using a short Matlab script. This script can be transparently adapted to any project with minimal modifications.

In general, recording hybrid tomograms and processing the data according to the SPA-STA workflow is beneficial for structural analysis of the majority of molecular complexes aiming at significant better resolution.

4 Discussions

Chapter 5 Conclusion

The research of this project on the structures of homopentameric serotonin receptor ($5HT_{3A}R$) in lipid-bilayers using cryo-SPA, with and without the presence of its native neurotransmitter, revealed three structures: one asymmetric serotonin-bound conformation and two ligand-free resting Apo conformations.

The MD simulations on the serotonin-bound conformation have observed free sodium ion permeation across the explicit lipid-bilayers along the pore, demonstrating our resolved serotonin-bound conformation is a fully opened conformation, which has not been published before. It helped our understanding on the gating mechanism of the serotonin receptor. The presence of cholesterol and lipids are considered having important modulations on channel gating, which explains why the previously published detergent-solubilized serotonin receptor could not response effectively to channel-opening upon ligand binding. The important cholesterol modulation facilitates the “coupling” of the TMD domain to the ECD through the ECD-TMD interface directly at post-M4 helices and indirectly through a clustering of conserved residues of the Cys-loop receptor family. That makes our finding an important step forward for the study on the gating mechanism other of other Cys-loop receptors. Besides, the phospholipids moiety present in between the subunits of the open conformation, is considered stabilized the open state. The interaction of the phospholipids at inter-subunit pockets contributes also to the loss of symmetry for the open state conformation.

Furthermore, the observation of an asymmetric ligand-free resting conformation is very interesting, which broaden our understanding of the homopentameric serotonin receptor in its Apo state. We speculate that the asymmetric Apo form and the symmetric Apo form stay equilibrium in absence of ligand, that both could bind serotonin but with different affinities: the asymmetric Apo state is more energetic-favorable. The asymmetric Apo state is considered like to be an intermediate state between the symmetric Apo state and the asymmetric open state. With MD simulations, more water wetting was observed on the serotonin docked asymmetric Apo form, which could be one evidence to support our speculation.

Together with the plasticity we observed for the serotonin-bound open conformation, and our knowledge of the previous electrophysiological studies, we

proposed a sequential binding model with lipid-allosteric modulation for the gating of serotonin receptor.

The study of lipid modulation on the serotonin receptor in native membrane would also be benefited from our developed hybrid SPA-STA workflow. Its ability to resolve higher resolution structures than the conventional STA was first proved on the tobacco mosaic virus (TMV) sample, which generated a 5.2Å structure.

With the application of the hybrid SPA-STA workflow, it is possible to push the hybrid STA resolution of the serotonin receptor in native state down to sub-nanometer level, at which allowing us to see the native lipid modulation on the receptor conformation.

Also in general, the hybrid SPA-STA workflow itself, could benefit other tomographic studies, which definitely beyond our pLGICs topics.

Chapter 6 Perspective

Throughout the main text, we had mentioned some of the future work that is important and meaningful to the full picture of pLGICs gating and relationship between conformation and dysfunction, with the help of our findings for the membrane-solubilized serotonin receptor. Here, I would like to put a list that, what I found, are the most interesting work to be continue doing in the future.

Firstly, the serotonin bound open conformation is resolved under a saturated condition. All the five LBPs in our serotonin-bound open conformation was occupied. For further study, it would be interesting to resolve the different structures with partly occupied LBPs in an unsaturated concentration of serotonin. It might be a bit challenging since the related LBPs and serotonin molecule is tiny. But the recently developed local refinement method (Zhang et al., 2019) of SPA could be useful. Optionally, from the biochemical aspect, conformational study using cryo-SPA for the mutagenesis on LPBs-disabled receptors or a chimera composed of low conductance with high conductance subunits (Rayes et al., 2009), could provide similar information potentially.

Secondly, the findings on lipid allosteric modulation on serotonin receptor gating is likely to open a new research topic for the study of specific phospholipids and steroids modulations on the conformation of pLGICs. This is likely to be done with either SPA or STA of the serotonin receptor in designed lipid in a mixture of different phospholipids (Carlson et al., 2018; Flayhan et al., 2018; Lütgebaucks et al., 2017).

Furthermore, photo-activated ligand (Rea et al., 2013) could be useful for conformational study. Without light input, the photo-activated ligand is cuddled in a caged-like chemical component, preventing the receptor from ligand binding. And when there is the binding event appreciated, ligand could be released with UV light. If this activation process happens right before plunge freezing, it might be possible to fix the first binding event of the serotonin receptor, means that the receptor has not gone through its activation life cycle, desensitization state would not be like present in the prepared cryo-EM specimen.

Besides, conformational study of the serotonin receptor binding with different antagonists and other drugs is also a good topic. Currently, there is one inhibited structure available for serotonin receptor bound with palonosetron at 2.8Å

(Zarkadas et al., 2020). This topic would help to understand the inhibitory mechanism of the serotonin receptors.

Apart from what cryo-SPA could help, cryo-ET and STA is of great power and unique to provide conformational details in native state. In a broader range of research topics beyond pLGICs, cryo-ET and STA researches on membrane proteins in native context is also of the author's great interests.

Appendix I

SerialEM script for hybrid tomography automation

```
MacroName HybridDoseSymmetricTomo
# Adopted from the script of Wim J.H.Hagen (EMBL Heidelberg 2015)
# Roll Buffers A-> H.
# Uses LowDose
# Run eucentric rough and fine
# Track plus K
# Track min L
# Record plus M
# Record min N

########## SETTINGS ##########
step              = 3      # stage tilt step in degrees
tilttimes         = 10    # multiply by 4 images + 1 image
Tiltbacklash    = -3     # negative tilts will be backlashed, must be negative value!

Driftcrit         = 3      # Angstrom/second
Driftinterval  = 10    # wait time between drift measurements in seconds
Drifttimes      = 5      # maximum number of drift measurements before skipping
########## END SETTINGS ##########

ResetClock
echo =====> batchrun HybridDoseSymmetricTomo
```

```
tiltangle = 0
CallFunction HybridDoseSymmetricTomo::TiltZero
# prevent runaway focus
AbsoluteFocusLimits -10 10
FocusChangeLimits -2 2

Loop $tilttimes
        # tilt plus1
tiltangle = $tiltangle + $step
CallFunction HybridDoseSymmetricTomo::TiltPlus
        # tilt min1
tiltangle = -1 * $tiltangle
CallFunction HybridDoseSymmetricTomo::TiltMinus
        # tilt min2
tiltangle = $tiltangle - $step
CallFunction HybridDoseSymmetricTomo::TiltMinus
        # tilt plus2
tiltangle = -1 * $tiltangle
CallFunction HybridDoseSymmetricTomo::TiltPlus
EndLoop

TiltTo 0
ResetImageShift
SetDefocus 0
echo ====================================

function TiltZero
# store stage position
```

```
ReportStageXYZ
StageX = $ReportedValue1
StageY = $ReportedValue2

# drift and tracking
T
Copy A K
Copy A L
Delay $driftinterval
Loop $drifttimes index
        T
        AlignTo K
                ReportAlignShift
        dx = $reportedValue3
        dy = $reportedValue4
        dist = sqrt $dx * $dx + $dy * $dy
        rate = $dist / $driftinterval * 10
        echo Rate = $rate A/sec
        If $rate < $driftcrit
                echo Drift is low enough after shot $index
                break
        Elseif $index < $drifttimes
                Delay $driftinterval
        Else
                echo Drift never got below $driftcrit: Skipping …
                break
        Endif
EndLoop
```

```
# autofocus
G
G
G

# store defocus
ReportDefocus
focusplus = $RepVal1
focusmin = $RepVal1

# acquire the “high-dose” tilt image here
Set Exposure R 15
R
S
RestoreCameraSet
Copy A M
Copy A N

# store image shifts
ReportImageShift
ISxplus = $RepVal1
ISyplus = $RepVal2
ISxminus = $RepVal1
ISyminus = $RepVal2

## tracking after just to be sure
#T
```

```
#Copy A K
#Copy A L
endfunction

function TiltPlus
# tilt stage
TiltTo $tiltangle

# reset stage XY
MoveStageTo $StageX $StageY

# set defocus and image shift
GoToLowDoseArea R
SetDefocus $focusplus
SetImageShift $ISxplus $ISyplus

# drift and tracking
T
AlignTo K
Delay $driftinterval
Loop $drifttimes index
        T
        AlignTo K
        ReportAlignShift
        dx = $reportedValue3
        dy = $reportedValue4
        dist = sqrt $dx * $dx + $dy * $dy
        rate = $dist / $driftinterval * 10
```

```
        echo Rate = $rate A/sec
        If $rate < $driftcrit
                echo Drift is low enough after shot $index
            break
        Elseif $index < $drifttimes
                Delay $driftinterval
        Else
                echo Drift never got below $driftcrit: Skipping …
                break
        Endif
EndLoop

# autofocus. Two rounds. Remove one G for single focus round.
G
G

# store defocus
ReportDefocus
focusplus = $RepVal1

# acquire tilt image
R
S

# tracking after
AlignTo M
Copy A M
```

```
# store image shifts
ReportImageShift
ISxplus = $RepVal1
ISyplus = $RepVal2

# new track reference
T
Copy A K
endfunction

Function TiltMinus
# tilt stage with backlash
TiltTo $tiltangle
TiltBy $Tiltbacklash
TiltTo $tiltangle

# reset stage XY
MoveStageTo $StageX $StageY

# set defocus and image shift
GoToLowDoseArea R
SetDefocus $focusmin
SetImageShift $ISxminus $ISyminus

# drift and tracking
T
AlignTo L
Delay $driftinterval
```

```
Loop $drifttimes index
        T
        AlignTo L
        ReportAlignShift
        dx = $reportedValue3
        dy = $reportedValue4
        dist = sqrt $dx * $dx + $dy * $dy
        rate = $dist / $driftinterval * 10
        echo Rate = $rate A/sec
        If $rate < $driftcrit
                echo Drift is low enough after shot $index
                break
        Elseif $index < $drifttimes
                Delay $driftinterval
        Else
                echo Drift never got below $driftcrit: Skipping …
                  break
        Endif
EndLoop

# autofocus. Two rounds. Remove one G for single focus round.
G
G

# store defocus
ReportDefocus
focusmin = $RepVal1
```

```
# acquire tilt image
R
S

# tracking after
AlignTo N
Copy A N

# store image shifts
ReportImageShift
ISxminus = $RepVal1
ISyminus = $RepVal2

# new track reference
T
Copy A L
endfunction
```

Appendix I

Bibliography

Adams, P. D., Grosse-Kunstleve, R. W., Hung, L. W., Ioerger, T. R., McCoy, A. J., Moriarty, N. W., . . . Terwilliger, T. C. (2002). PHENIX: building new software for automated crystallographic structure determination. *Acta Crystallogr. D Biol. Crystallogr. , 58*(Pt 11), 1948-1954. doi:10.1107/s0907444902016657

Addona, G. H., Sandermann, H., Kloczewiak, M. A., Husain, S. S., & Miller, K. W. (1998). Where does cholesterol act during activation of the nicotinic acetylcholine receptor? *Biochimica et Biophysica Acta (BBA) - Biomembranes, 1370*(2), 299-309. doi:10.1016/S0005-2736(97)00280-0

Al-Amoudi, A., Chang, J.-J., Leforestier, A., McDowall, A., Salamin, L. M., Norlén, L. P. O., . . . Dubochet, J. (2004). Cryo-electron microscopy of vitreous sections. *The EMBO journal, 23*(18), 3583-3588. doi:10.1038/sj.emboj.7600366

Althoff, T., Hibbs, R. E., Banerjee, S., & Gouaux, E. (2014). X-ray structures of GluCl in apo states reveal a gating mechanism of Cys-loop receptors. *Nature, 512*, 333-337. doi:10.1038/nature13669

Asarnow, D., Palovcak, E., & Cheng, Y. (2019, 2019/Dec/16). asarnow/pyem:UCSF pyem v0.5. Retrieved from zenodo.org/record/3576630#.XiGKEC3MxBw

Auerbach, A. (2015). Agonist activation of a nicotinic acetylcholine receptor. *Neuropharmacology, 96*(Pt B), 150-156. doi:10.1016/j.neuropharm.2014.10.004

Baenziger, J. E., Hénault, C. M., Therien, J. P. D., & Sun, J. (2015). Nicotinic acetylcholine receptor–lipid interactions: Mechanistic insight and biological function. *Biochimica et Biophysica Acta (BBA) - Biomembranes, 1848*(9), 1806-1817. doi:https://doi.org/10.1016/j.bbamem.2015.03.010

Baier, C. J., Fantini, J., & Barrantes, F. J. (2011). Disclosure of cholesterol recognition motifs in transmembrane domains of the human nicotinic acetylcholine receptor. *Scientific Reports, 1*(1), 69-75. doi:10.1038/srep00069

Baker, L. A., Grange, M., & Grünewald, K. (2017). Electron cryo-tomography captures macromolecular complexes in native environments. *Current Opinion in Structural Biology, 46*, 149-156. doi:https://doi.org/10.1016/j.sbi.2017.08.005

Bammes, B. E., Rochat, R. H., Jakana, J., Chen, D. H., & Chiu, W. (2012). Direct electron detection yields cryo-EM reconstructions at resolutions beyond 3/4 Nyquist frequency. *Journal of Structural Biology, 177*(3), 589-601. doi:10.1016/j.jsb.2012.01.008

Barrantes, F. J., & Fantini, J. (2016). From hopanoids to cholesterol: Molecular clocks of pentameric ligand-gated ion channels. *Progress in Lipid Research, 63*, 1-13. doi:10.1016/j.plipres.2016.03.003

Basak, S., Gicheru, Y., Rao, S., Sansom, M. S. P., & Chakrapani, S. (2018). Cryo-EM reveals two distinct serotonin-bound conformations of full-length 5-HT3A receptor. *Nature, 563*(7730), 270-274. doi:10.1038/s41586-018-0660-7

Basak, S., Gicheru, Y., Samanta, A., Molugu, S. K., Huang, W., Fuente, M., . . . Chakrapani, S. (2018). Cryo-EM structure of 5-HT3A receptor in its resting conformation. *Nature Communications, 9*(1), 514-524. doi:10.1038/s41467-018-02997-4

Bell, J. M., Chen, M., Baldwin, P. R., & Ludtke, S. J. (2016). High resolution single particle refinement in EMAN2.1. *Methods (San Diego, Calif.), 100*, 25-34. doi:10.1016/j.ymeth.2016.02.018

Bharat, T. A. M., & Scheres, S. H. W. (2016). Resolving macromolecular structures from electron cryo-tomography data using subtomogram averaging in RELION. *Nature Protocols, 11*(11), 9-20. doi:10.1038/nprot.2016.124

Biyani, N., Righetto, R. D., McLeod, R., Caujolle-Bert, D., Castano-Diez, D., Goldie, K. N., & Stahlberg, H. (2017). Focus: The interface between data collection and data processing in cryo-EM. *Journal of Structural Biology, 198*(2), 124-133. doi:10.1016/j.jsb.2017.03.007

Bocquet, N., Nury, H., Baaden, M., Le Poupon, C., Changeux, J.-P., Delarue, M., & Corringer, P.-J. (2009). X-ray structure of a pentameric ligand-gated ion channel in an apparently open conformation. *Nature, 457*(7225), 111-114. doi:10.1038/nature07462

Booth, C., & Mooey, P. E. T. (2014). Applications of electron-counting direct-detection cameras in high- resolution cryo-electron microscopy.

Bouzat, C., & Sine, S. M. (2018). Nicotinic acetylcholine receptors at the single-channel level. *British Journal of Pharmacology, 175*(11), 1789-1804. doi:10.1111/bph.13770

Brejc, K., van Dijk, W. J., Klaassen, R. V., Schuurmans, M., van der Oost, J., Smit, A. B., & Sixma, T. K. (2001). Crystal structure of an ACh-binding protein reveals the ligand-binding domain of nicotinic receptors. *Nature, 411*(6835), 269-276. doi:10.1038/35077011

Brillault, L., & Landsberg, M. J. (2020). Preparation of Proteins and Macromolecular Assemblies for Cryo-electron Microscopy. In J. A. Gerrard & L. J. Domigan (Eds.), *Protein Nanotechnology: Protocols, Instrumentation, and Applications* (pp. 221-246). New York, NY: Springer US.

Brilot, A. F., Chen, J. Z., Cheng, A. C., Pan, J. H., Harrison, S. C., Potter, C. S., . . . Grigorieff, N. (2012). Beam-induced motion of vitrified specimen on holey carbon film. *Journal of Structural Biology, 177*(3), 630-637. doi:10.1016/j.jsb.2012.02.003

Brown, A. M., Hope, A. G., Lambert, J. J., & Peters, J. A. (1998). Ion permeation and conduction in a human recombinant 5-HT3 receptor subunit (h5-HT3A). *The Journal of physiology, 507 (Pt 3)*, 653-665.

Brüggeller, P., & Mayer, E. (1980). Complete vitrification in pure liquid water and dilute aqueous solutions. *Nature, 288*(5791), 569-571. doi:10.1038/288569a0

Buchan, D. W. A., & Jones, D. T. (2019). The PSIPRED Protein Analysis Workbench: 20 years on. *Nucleic Acids Research, 47*(W1), W402-W407. doi:10.1093/nar/gkz297

Budinger, T. F., & Glaeser, R. M. (1976). Measurement of focus and spherical aberration of an electron microscope objective lens. *Ultramicroscopy, 2*, 31-41. doi:https://doi.org/10.1016/S0304-3991(76)90263-1

Cao, E., Liao, M., Cheng, Y., & Julius, D. (2013). TRPV1 structures in distinct conformations reveal activation mechanisms. *Nature, 504*(7478), 113-118. doi:10.1038/nature12823

Carlson, M. L., Young, J. W., Zhao, Z., Fabre, L., Jun, D., Li, J., . . . Duong, F. (2018). The Peptidisc, a simple method for stabilizing membrane proteins in detergent-free solution. *eLife, 7*, e34085. doi:10.7554/eLife.34085

Castano-Diez, D., Kudryashev, M., Arheit, M., & Stahlberg, H. (2012). Dynamo: a flexible, user-friendly development tool for subtomogram averaging of cryo-EM data in high-performance computing environments. *J Struct Biol, 178*(2), 139-151. doi:10.1016/j.jsb.2011.12.017

Castano-Diez, D., Kudryashev, M., & Stahlberg, H. (2017). Dynamo Catalogue: Geometrical tools and data management for particle picking in subtomogram averaging of cryo-electron tomograms. *J Struct Biol, 197*(2), 135-144. doi:10.1016/j.jsb.2016.06.005

Celie, P. H. N., Kasheverov, I. E., Mordvintsev, D. Y., Hogg, R. C., van Nierop, P., van Elk, R., . . . Smit, A. B. (2005). Crystal structure of nicotinic acetylcholine receptor homolog AChBP in complex with an α-conotoxin PnIA variant. *Nature Structural & Molecular Biology, 12*(7), 582-588. doi:10.1038/nsmb951

Changeux, J.-P. (2012). Allostery and the Monod-Wyman-Changeux Model After 50 Years. *Annual Review of Biophysics, 41*(1), 103-133. doi:10.1146/annurev-biophys-050511-102222

Changeux, J.-P., & Edelstein, S. J. (2005). Allosteric Mechanisms of Signal Transduction. *Science, 308*(5727), 1424. doi:10.1126/science.1108595

Changeux, J.-P., Kasai, M., & Lee, C.-Y. (1970). Use of a Snake Venom Toxin to Characterize the Cholinergic Receptor Protein. *Proceedings of the National Academy of Sciences, 67*(3), 1241. doi:10.1073/pnas.67.3.1241

Changeux, J.-P., Thiéry, J., Tung, Y., & Kittel, C. (1967). ON THE COOPERATIVITY OF BIOLOGICAL MEMBRANES. *Proceedings of the National Academy of Sciences, 57*(2), 335. doi:10.1073/pnas.57.2.335

Changeux, J. P. (1966). Responses of acetylcholinesterase from Torpedo marmorata to salts and curarizing drugs. *Molecular Pharmacology, 2*(5), 369-392.

Chen, Q., Wells, M. M., Tillman, T. S., Kinde, M. N., Cohen, A., Xu, Y., & Tang, P. (2017). Structural Basis of Alcohol Inhibition of the Pentameric Ligand-Gated Ion Channel ELIC. *Structure, 25*(1), 180-187. doi:https://doi.org/10.1016/j.str.2016.11.007

Chen, S., McMullan, G., Faruqi, A. R., Murshudov, G. N., Short, J. M., Scheres, S. H. W., & Henderson, R. (2013). High-resolution noise substitution to measure overfitting and validate resolution in 3D structure determination by single particle electron cryomicroscopy. *Ultramicroscopy, 135*, 24-35. doi:10.1016/j.ultramic.2013.06.004

Chen, V. B., Arendall, W. B., 3rd, Headd, J. J., Keedy, D. A., Immormino, R. M., Kapral, G. J., . . . Richardson, D. C. (2010). MolProbity: all-atom structure validation for macromolecular crystallography. *Acta Crystallogr. D Biol. Crystallogr., 66*(Pt 1), 12-21. doi:10.1107/S0907444909042073

Chreifi, G., Chen, S., Metskas, L. A., Kaplan, M., & Jensen, G. J. (2019). Rapid tilt-series acquisition for electron cryotomography. *Journal of Structural Biology, 205*(2), 163-169. doi:10.1016/j.jsb.2018.12.008

Contrast transfer function (CTF) correction. (2015).

Cordes, F. S., Bright, J. N., & Sansom, M. S. (2002). Proline-induced distortions of transmembrane helices. *Journal of Molecular Biology, 323*(5), 951-960. doi:10.1016/s0022-2836(02)01006-9

Corradi, J., Gumilar, F., & Bouzat, C. (2009). Single-channel kinetic analysis for activation and desensitization of homomeric 5-HT(3)A receptors. *Biophysical Journal, 97*(5), 1335-1345. doi:10.1016/j.bpj.2009.06.018

Criado, M., Eibl, H., & Barrantes, F. (1984). Functional properties of the acetylcholine receptor incorporated in model lipid membranes. Differential effects of chain length and head group of phospholipids on receptor affinity states and receptor-mediated ion translocation. *Journal of Biological Chemistry, 259*, 9188-9198.

D'Imprima, E., Floris, D., Joppe, M., Sanchez, R., Grininger, M., & Kuehlbrandt, W. (2019). The deadly touch protein denaturation at the water-air interface and how to prevent it. *eLife, 8*, e42747. doi:10.7554/eLife.42747

daCosta, C. J. B., & Baenziger, J. E. (2009). A Lipid-dependent Uncoupled Conformation of the Acetylcholine Receptor. *Journal of Biological Chemistry, 284*(26), 17819-17825.

daCosta, Corrie J. B., & Baenziger, John E. (2013). Gating of pentameric ligand-gated ion channels: structural insights and ambiguities. *Structure, 21*(8), 1271-1283. doi:10.1016/j.str.2013.06.019

Dahl, R., & Staehelin, L. A. (1989). High-pressure freezing for the preservation of biological structure: Theory and practice. *Journal of Electron Microscopy Technique, 13*(3), 165-174. doi:10.1002/jemt.1060130305

Danev, R., Yanagisawa, H., & Kikkawa, M. (2019). Cryo-Electron Microscopy Methodology: Current Aspects and Future Directions. *Trends in Biochemical Sciences, 44*(10), 837-848. doi:https://doi.org/10.1016/j.tibs.2019.04.008

Davies, P. A., Pistis, M., Hanna, M. C., Peters, J. A., Lambert, J. J., Hales, T. G., & Kirkness, E. F. (1999). The 5-HT3B subunit is a major determinant of serotonin-receptor function. *Nature, 397*(6717), 359-363. doi:10.1038/16941

de Jesus, A. J. A., Toby W. (2013). The role of tryptophan side chains in membrane protein anchoring and hydrophobic mismatch. *Biochimica et Biophysica Acta (BBA) - Biomembranes, 1828*(2), 864-876. doi:10.1016/j.bbamem.2012.09.009

Dent, J. A. (2010). The Evolution of Pentameric Ligand-Gated Ion Channels. In S. H. Thany (Ed.), *Insect Nicotinic Acetylcholine Receptors* (pp. 11-23). New York, NY: Springer New York.

Deptuch, G., Besson, A., Rehak, P., Szelezniak, M., Wall, J., Winter, M., & Zhu, Y. (2007). Direct electron imaging in electron microscopy with monolithic active pixel sensors. *Ultramicroscopy, 107*(8), 674-684. doi:https://doi.org/10.1016/j.ultramic.2007.01.003

Drulyte, I., Johnson, R. M., Hesketh, E. L., Hurdiss, D. L., Scarff, C. A., Porav, S. A., . . . Thompson, R. F. (2018). Approaches to altering particle distributions in cryo-electron microscopy sample preparation. *Acta Crystallogr D Struct Biol, 74*(Pt 6), 560-571. doi:10.1107/S2059798318006496

Du, J., Lu, W., Wu, S., Cheng, Y., & Gouaux, E. (2015). Glycine receptor mechanism elucidated by electron cryo-microscopy. *Nature, 526*(7572), 224-229. doi:10.1038/nature14853

Eibauer, M., Hoffmann, C., Plitzko, J. M., Baumeister, W., Nickell, S., & Engelhardt, H. (2012). Unraveling the structure of membrane proteins in situ by transfer function corrected cryo-electron tomography. *J Struct Biol, 180*(3), 488-496. doi:10.1016/j.jsb.2012.09.008

Eibauer, M., Pellanda, M., Turgay, Y., Dubrovsky, A., Wild, A., & Medalia, O. (2015). Structure and gating of the nuclear pore complex. *Nature Communications, 6*(1), 7532. doi:10.1038/ncomms8532

Eisensamer, B., Uhr, M., Meyr, S., Gimpl, G., Deiml, T., Rammes, G., . . . Rupprecht, R. (2005). Antidepressants and antipsychotic drugs colocalize with 5-HT3 receptors in raft-like domains. *Journal of Neuroscience, 25*(44), 10198-10206. doi:10.1523/JNEUROSCI.2460-05.2005

Eisenstein, F., Danev, R., & Pilhofer, M. (2019). Improved applicability and robustness of fast cryo-electron tomography data acquisition. *Journal of Structural Biology*. doi:https://doi.org/10.1016/j.jsb.2019.08.006

Ellena, J. F., Blazing, M. A., & McNamee, M. G. (1983). Lipid-protein interactions in reconstituted membranes containing acetylcholine receptor. *Biochemistry, 22*(24), 5523-5535. doi:10.1021/bi00293a012

Emsley, P., Lohkamp, B., Scott, W. G., & Cowtan, K. (2010). Features and development of Coot. *Acta Crystallogr D Biol Crystallogr, 66*(Pt 4), 486-501. doi:10.1107/S0907444910007493

Espinosa Bosch, M., Ruiz Sánchez, A. J., Sánchez Rojas, F., & Bosch Ojeda, C. (2017). Review of analytical methodologies for the determination of 5-HT3 receptor antagonists. *Microchemical Journal, 132*, 341-350. doi:https://doi.org/10.1016/j.microc.2017.02.023

F. Zemlin, K. W., P. Schiske, W. Kunath and K. H. Herrmann. (1978). Coma-free alignmnet of high resolution electron microscopes with the aid of optical diffractograms. *Ultramicroscopy, 3*, 49-60.

Falcon 3EC Direct Electron Detector. (2019).

Fan, X., Wang, J., Zhang, X., Yang, Z., Zhang, J.-C., Zhao, L., . . . Wang, H.-W. (2019). Single particle cryo-EM reconstruction of 52 kDa streptavidin at 3.2 Angstrom resolution. *Nature Communications, 10*(1), 2386. doi:10.1038/s41467-019-10368-w

Fantini, J., & Barrantes, F. J. (2009). Sphingolipid/cholesterol regulation of neurotransmitter receptor conformation and function. *Biochimica et Biophysica Acta (BBA) - Biomembranes, 1788*(11), 2345-2361. doi:10.1016/j.bbamem.2009.08.016

Faruqi, A. R. (2015). Progress and development of direct detectors for Electron Cryo-Microscopy (Vol. 190, pp. 103-141.).

Fauland, A., Köfeler, H., Trötzmüller, M., Knopf, A., Hartler, J., Eberl, A., . . . Spener, F. (2011). A comprehensive method for lipid profiling by liquid chromatography-ion cyclotron resonance mass spectrometry. *Journal of Lipid Research, 52*(12), 2314-2322. doi:10.1194/jlr.D016550

Fernandez, J.-J., Li, S., & Agard, D. A. (2019). Consideration of sample motion in cryo-tomography based on alignment residual interpolation. *Journal of Structural Biology, 205*(3), 1-6. doi:https://doi.org/10.1016/j.jsb.2019.01.005

Fernandez, J. J., Luque, D., Caston, J. R., & Carrascosa, J. L. (2008). Sharpening high resolution information in single particle electron cryomicroscopy. *J Struct Biol, 164*(1), 170-175. doi:10.1016/j.jsb.2008.05.010

Flayhan, A., Mertens, H. D. T., Ural-Blimke, Y., Martinez Molledo, M., Svergun, D. I., & Löw, C. (2018). Saposin Lipid Nanoparticles: A Highly Versatile and Modular Tool

for Membrane Protein Research. *Structure, 26*(2), 345-355.e345. doi:https://doi.org/10.1016/j.str.2018.01.007

Flores, J. A., Haddad, B. G., Dolan, K. A., Myers, J. B., Yoshioka, C. C., Copperman, J., . . . Reichow, S. L. (2020). Connexin-46/50 in a dynamic lipid environment resolved by CryoEM at 1.9 Å. *bioRxiv*, 2020.2004.2014.036384. doi:10.1101/2020.04.14.036384

Frank, J. (2006). *Three-Dimensional Electron Microscopy of Macromolecular Assemblies: Visualization of Biological Molecules in Their Native State*. Oxford University: Oxford University Press.

Frauenfeld, J., Loving, R., Armache, J. P., Sonnen, A. F. P., Guettou, F., Moberg, P., . . . Nordlund, P. (2016). A saposin-lipoprotein nanoparticle system for membrane proteins. *Nature Methods, 13*(4), 345-351. doi:10.1038/Nmeth.3801

Galej, W. P., Wilkinson, M. E., Fica, S. M., Oubridge, C., Newman, A. J., & Nagai, K. (2016). Cryo-EM structure of the spliceosome immediately after branching. *Nature, 537*(7619), 197-+. doi:10.1038/nature19316

Greenwood, J. R., Calkins, D., Sullivan, A. P., & Shelley, J. C. (2010). Towards the comprehensive, rapid, and accurate prediction of the favorable tautomeric states of drug-like molecules in aqueous solution. *Journal of Computer-Aided Molecular Design, 24*(6-7), 591-604. doi:10.1007/s10822-010-9349-1

Grigorieff, N. (2016). Frealign: An Exploratory Tool for Single-Particle Cryo-EM. *Methods in Enzymology, 579*, 191-226. doi:10.1016/bs.mie.2016.04.013

Guixà-González, R., Rodriguez-Espigares, I., Ramírez-Anguita, J. M., Carrió-Gaspar, P., Martinez-Seara, H., Giorgino, T., & Selent, J. (2014). MEMBPLUGIN: studying membrane complexity in VMD. *Bioinformatics, 30*(10), 1478-1480. doi:10.1093/bioinformatics/btu037

Guros, N. B., Balijepalli, A., & Klauda, J. B. (2020). Microsecond-timescale simulations suggest 5-HT–mediated preactivation of the 5-HT3A serotonin receptor. *Proceedings of the National Academy of Sciences of the United States of America, 117*(1), 405-414. doi:10.1073/pnas.1908848117

Hagen, W. J. H., Wan, W., & Briggs, J. A. G. (2017). Implementation of a cryo-electron tomography tilt-scheme optimized for high resolution subtomogram averaging. *Journal of Structural Biology, 197*(2), 191-198. doi:10.1016/j.jsb.2016.06.007

Hama, A., & Menzaghi, F. (2001). Antagonist of nicotinic acetylcholine receptors (nAChR) enhances formalin-induced nociception in rats: tonic role of nAChRs in the control of pain following injury. *Brain Research, 888*(1), 102-106. doi:https://doi.org/10.1016/S0006-8993(00)03022-5

Harris, J. R., & Scheffler, D. (2002). Routine preparation of air-dried negatively stained and unstained specimens on holey carbon support films: a review of applications. *Micron, 33*(5), 461-480. doi:https://doi.org/10.1016/S0968-4328(01)00039-7

Hartler, J., Triebl, A., Ziegl, A., Trötzmüller, M., Rechberger, G. N., Zeleznik, O. A., . . . Thallinger, G. G. (2017). Deciphering lipid structures based on platform-independent decision rules. *Nature Methods, 14*(12), 1171-1174. doi:10.1038/nmeth.4470

Hartler, J., Trotzmuller, M., Chitraju, C., Spener, F., Kofeler, H. C., & Thallinger, G. G. (2011). Lipid Data Analyzer: unattended identification and quantitation of lipids in LC-MS data. *Bioinformatics, 27*(4), 572-577.

Harvey Sternbach, M. D. (1991). The serotonin syndrome. *American Journal of Psychiatry, 148*, 705-713.

Hassaine, G., Deluz, C., Grasso, L., Wyss, R., Tol, M. B., Hovius, R., . . . Nury, H. (2014). X-ray structure of the mouse serotonin 5-HT3 receptor. *Nature, 512*(7514), 276-281. doi:10.1038/nature13552

Hawkes, P. W. (1990). Ernst Ruska. *Physics Today, 43*(7), 84. doi:10.1063/1.2810640

Hayles, M. F., Stokes, D. J., Phifer, D., & Findlay, K. C. (2007). A technique for improved focused ion beam milling of cryo-prepared life science specimens. *Journal of Microscopy, 226*(3), 263-269. doi:10.1111/j.1365-2818.2007.01775.x

Heimowitz, A., Anden, J., & Singer, A. (2018). APPLE picker: Automatic particle picking, a low-effort cryo-EM framework. *J Struct Biol, 204*(2), 215-227. doi:10.1016/j.jsb.2018.08.012

Hibbs, R. E., & Gouaux, E. (2011). Principles of activation and permeation in an anion-selective Cys-loop receptor. *Nature, 474*(7349), 54-60. doi:10.1038/nature10139

Himes, B. A., & Zhang, P. (2018). emClarity: software for high-resolution cryo-electron tomography and subtomogram averaging. *Nature Methods, 15*(11), 955-961. doi:10.1038/s41592-018-0167-z

Hosie, A. M., Wilkins, M. E., da Silva, H. M. A., & Smart, T. G. (2006). Endogenous neurosteroids regulate GABAA receptors through two discrete transmembrane sites. *Nature, 444*(7118), 486-489. doi:10.1038/nature05324

Hovius, R., Tairi, A.-P., Blasey, H., Bernard, A., Lundström, K., & Vogel, H. (1998). Characterization of a Mouse Serotonin 5-HT3 Receptor Purified from Mammalian Cells. *Journal of Neurochemistry, 70*(2), 824-834. doi:10.1046/j.1471-4159.1998.70020824.x

Hryc, C. F., Chen, D.-H., Afonine, P. V., Jakana, J., Wang, Z., Haase-Pettingell, C., . . . Chiu, W. (2017). Accurate model annotation of a near-atomic resolution cryo-EM map. *Proceedings of the National Academy of Sciences, 114*(12), 3103. doi:10.1073/pnas.1621152114

Huang, G., Zhang, Y., Zhu, X., Zeng, C., Wang, Q., Zhou, Q., . . . Shi, Y. (2020). Structure of the Cytoplasmic Ring of the Xenopus laevisn Nuclear Pore Complex. *bioRxiv*, 2020.2003.2027.009407. doi:10.1101/2020.03.27.009407

Huang, X., Chen, H., Michelsen, K., Schneider, S., & Shaffer, P. L. (2015). Crystal structure of human glycine receptor-α3 bound to antagonist strychnine. *Nature, 526*(7572), 277-280. doi:10.1038/nature14972

Humphrey, W., Dalke, A., & Schulten, K. (1996). VMD: Visual molecular dynamics. *Journal of Molecular Graphics, 14*(1), 33-38. doi:10.1016/0263-7855(96)00018-5

Ilca, S. L., Kotecha, A., Sun, X., Poranen, M. M., Stuart, D. I., & Huiskonen, J. T. (2015). Localized reconstruction of subunits from electron cryomicroscopy images of macromolecular complexes. *Nat Commun, 6*, 8843. doi:10.1038/ncomms9843

Irobalieva, R. N., Martins, B., & Medalia, O. (2016). Cellular structural biology as revealed by cryo-electron tomography. *Journal of Cell Science, 129*(3), 469. doi:10.1242/jcs.171967

Jackson, M. B., & Yakel, J. L. (1995). The 5-HT3 receptor channel. *Annual Review of Physiology, 57*, 447-468. doi:10.1146/annurev.ph.57.030195.002311

Jain, T., Sheehan, P., Crum, J., Carragher, B., & Potter, C. S. (2012). Spotiton: a prototype for an integrated inkjet dispense and vitrification system for cryo-TEM. *Journal of Structural Biology, 179*(1), 68-75. doi:10.1016/j.jsb.2012.04.020

Jaiteh, M., Taly, A., & Hénin, J. (2016). Evolution of pentameric ligand-gated ion channels: pro-loop receptors. *PloS one, 11*(3), e0151934. doi:10.1371/journal.pone.0151934

Jakobi, A. J., Wilmanns, M., & Sachse, C. (2017). Model-based local density sharpening of cryo-EM maps. *eLife, 6*, e27131. doi:10.7554/eLife.27131

Jerabek-Willemsen, M., André, T., Wanner, R., Roth, H. M., Duhr, S., Baaske, P., & Breitsprecher, D. (2014). MicroScale Thermophoresis: Interaction analysis and beyond. *Journal of Molecular Structure, 1077*, 101-113. doi:https://doi.org/10.1016/j.molstruc.2014.03.009

Jo, S., Kim, T., Iyer, V. G., & Im, W. (2008). CHARMM-GUI: A web-based graphical user interface for CHARMM. *Journal of computational chemistry, 29*(11), 1859-1865. doi:10.1002/jcc.20945

K3 Camera. (2020).

Kalamida, D., Poulas, K., Avramopoulou, V., Fostieri, E., Lagoumintzis, G., Lazaridis, K., . . . Tzartos, S. J. (2007). Muscle and neuronal nicotinic acetylcholine receptors. *The FEBS Journal, 274*(15), 3799-3845. doi:10.1111/j.1742-4658.2007.05935.x

Kash, T. L., Jenkins, A., Kelley, J. C., Trudell, J. R., & Harrison, N. L. (2003). Coupling of agonist binding to channel gating in the GABAA receptor. *Nature, 421*(6920), 272-275. doi:10.1038/nature01280

Khoshouei, M., Pfeffer, S., Baumeister, W., Forster, F., & Danev, R. (2017). Subtomogram analysis using the Volta phase plate. *Journal of Structural Biology, 197*(2), 94-101.

Khoshouei, M., Radjainia, M., Phillips, A. J., Gerrard, J. A., Mitra, A. K., Plitzko, J. M., . . . Danev, R. (2016). Volta phase plate cryo-EM of the small protein complex Prx3. *Nat Commun, 7*, 10534. doi:10.1038/ncomms10534

Klauda, J. B., Venable, R. M., Freites, J. A., O'Connor, J. W., Tobias, D. J., Mondragon-Ramirez, C., . . . Pastor, R. W. (2010). Update of the CHARMM all-atom additive force field for lipids: validation on six lipid types. *Journal of Physical Chemistry B, 114*(23), 7830-7843. doi:10.1021/jp101759q

Klesse, G., Rao, S., Sansom, M. S. P., & Tucker, S. J. (2019). CHAP: A versatile tool for the structural and functional annotation of ion channel pores. *Journal of Molecular Biology, 431*(17), 3353-3365. doi:10.1016/j.jmb.2019.06.003

Kovtun, O., Leneva, N., Bykov, Y. S., Ariotti, N., Teasdale, R. D., Schaffer, M., . . . Collins, B. M. (2018). Structure of the membrane-assembled retromer coat determined by cryo-electron tomography. *Nature, 561*(7724), 561-564. doi:10.1038/s41586-018-0526-z

Kremer, J. R., Mastronarde, D. N., & McIntosh, J. R. (1996). Computer Visualization of Three-Dimensional Image Data Using IMOD. *Journal of Structural Biology, 116*(1), 71-76. doi:https://doi.org/10.1006/jsbi.1996.0013

Kudryashev, M. (2018). *Cellular Imaging. Biological and Medical Physics, Biomedical Engineering*: Springer, Cham.

Kudryashev, M., Castano-Diez, D., Deluz, C., Hassaine, G., Grasso, L., Graf-Meyer, A., . . . Stahlberg, H. (2016). The Structure of the Mouse Serotonin 5-HT3 Receptor in Lipid Vesicles. *Structure, 24*(1), 165-170. doi:10.1016/j.str.2015.11.004

Kuhlbrandt, W. (2014). Biochemistry. The resolution revolution. *Science, 343*(6178), 1443-1444. doi:10.1126/science.1251652

Kunpeng Li, Chen Sun, Thomas Klose, Jose Irimia-Dominguez, Frank S. Vago, Ruben Vidal, & Jiang, W. (2019). Sub-3 Å apoferritin structure determined with full range of phase shifts using a single position of volta phase plate. *Journal of Structural Biology, 206*(2), 225-232.

Lander, G. C., Stagg, S. M., Voss, N. R., Cheng, A., Fellmann, D., Pulokas, J., . . . Carragher, B. (2009). Appion: an integrated, database-driven pipeline to facilitate EM image processing. *Journal of Structural Biology, 166*(1), 95-102. doi:10.1016/j.jsb.2009.01.002

Laurie, D. J., Seeburg, P. H., & Wisden, W. (1992). The distribution of 13 GABAA receptor subunit mRNAs in the rat brain. II. Olfactory bulb and cerebellum. *The Journal of neuroscience : the official journal of the Society for Neuroscience, 12*(3), 1063-1076. doi:10.1523/JNEUROSCI.12-03-01063.1992

Laverty, D., Desai, R., Uchanski, T., Masiulis, S., Stec, W. J., Malinauskas, T., . . . Aricescu, A. R. (2019). Cryo-EM structure of the human alpha1beta3gamma2 GABAA receptor in a lipid bilayer. *Nature, 565*(7740), 516-520. doi:10.1038/s41586-018-0833-4

Leigh, E. K., Navarro, P. P., Scaramuzza, S., Chen, W., Zhang, Y., Castano-Diez, D., & Kudryashev, M. (2019). Subtomogram averaging from cryo-electron tomograms *Methods in cell biology* American Society for Cell Biology, Elsevier.

Li, X., Mooney, P., Zheng, S., Booth, C. R., Braunfeld, M. B., Gubbens, S., . . . Cheng, Y. (2013). Electron counting and beam-induced motion correction enable near-atomic-resolution single-particle cryo-EM. *Nature Methods, 10*(6), 584-590. doi:10.1038/nmeth.2472

Li, X., Mooney, P., Zheng, S., Booth, C. R., Braunfeld, M. B., Gubbens, S., . . . Cheng, Y. (2013). Electron counting and beam-induced motion correction enable near-atomic-resolution single-particle cryo-EM. *Nature Methods, 10*(6), 584-590. doi:10.1038/nmeth.2472

Li, X., Zheng, S., Agard, D. A., & Cheng, Y. (2015). Asynchronous data acquisition and on-the-fly analysis of dose fractionated cryoEM images by UCSFImage. *Journal of Structural Biology, 192*(2), 174-178. doi:10.1016/j.jsb.2015.09.003

Li, Y., Cash, J. N., Tesmer, J. J. G., & Cianfrocco, M. A. (2020). High-Throughput Cryo-EM Enabled by User-Free Preprocessing Routines. *Structure*. doi:https://doi.org/10.1016/j.str.2020.03.008

Lomize, A. L., Pogozheva, I. D., & Mosberg, H. I. (2011). Anisotropic solvent model of the lipid bilayer. 1. Parameterization of long-range electrostatics and first solvation shell effects. *Journal of Chemical Information and Modeling, 51*(4), 918-929. doi:10.1021/ci2000192

Lütgebaucks, C., Macias-Romero, C., & Roke, S. (2017). Characterization of the interface of binary mixed DOPC:DOPS liposomes in water: The impact of charge condensation. *The Journal of Chemical Physics, 146*(4), 044701. doi:10.1063/1.4974084

Magnusson, A. O., Szekrenyi, A., Joosten, H.-J., Finnigan, J., Charnock, S., & Fessner, W.-D. (2019). nanoDSF as screening tool for enzyme libraries and biotechnology development. *The FEBS Journal, 286*(1), 184-204. doi:10.1111/febs.14696

Maksay, G. (2013). Asymmetric perturbation of pLGICs: action! *Trends in Pharmacological Sciences, 34*(6), 299-300. doi:10.1016/j.tips.2013.04.003

Maricq, A. V., Peterson, A. S., Brake, A. J., Myers, R. M., & Julius, D. (1991). Primary structure and functional expression of the 5HT3 receptor, a serotonin-gated ion channel. *Science, 254*(5030), 432. doi:10.1126/science.1718042

Masiulis, S., Desai, R., Uchański, T., Serna Martin, I., Laverty, D., Karia, D., . . . Aricescu, A. R. (2019). GABAA receptor signalling mechanisms revealed by structural pharmacology. *Nature, 565*(7740), 454-459. doi:10.1038/s41586-018-0832-5

Mastronarde, D. N. (2005). Automated electron microscope tomography using robust prediction of specimen movements. *Journal of Structural Biology, 152*(1), 36-51. doi:https://doi.org/10.1016/j.jsb.2005.07.007

Matthies, D., Dalmas, O., Borgnia, M. J., Dominik, P. K., Merk, A., Rao, P., . . . Subramaniam, S. (2016). Cryo-EM structures of the magnesium channel CorA reveal symmetry break upon gating. *Cell, 164*(4), 747-756. doi:10.1016/j.cell.2015.12.055

Matyash, V., Liebisch, G., Kurzchalia, T. V., Shevchenko, A., & Schwudke, D. (2008). Lipid extraction by methyl-tert-butyl ether for high-throughput lipidomics. *Journal of Lipid Research, 49*(5), 1137-1146. doi:10.1194/jlr.D700041-JLR200

McCarthy, M. P., & Moore, M. A. (1992). Effects of lipids and detergents on the conformation of the nicotinic acetylcholine receptor from Torpedo californica. *Journal of Biological Chemistry, 267*(11), 7655-7663.

McMullan, G., Faruqi, A. R., Clare, D., & Henderson, R. (2014). Comparison of optimal performance at 300keV of three direct electron detectors for use in low dose electron microscopy. *Ultramicroscopy, 147*, 156-163. doi:https://doi.org/10.1016/j.ultramic.2014.08.002

McMullan, G., Faruqi, A. R., & Henderson, R. (2016). Chapter One - Direct Electron Detectors. In R. A. Crowther (Ed.), *Methods in Enzymology* (Vol. 579, pp. 1-17): Academic Press.

McMullan, G., Faruqi, A. R., Henderson, R., Guerrini, N., Turchetta, R., Jacobs, A., & van Hoften, G. (2009). Experimental observation of the improvement in MTF from backthinning a CMOS direct electron detector. *Ultramicroscopy, 109*(9), 1144-1147. doi:https://doi.org/10.1016/j.ultramic.2009.05.005

Meyerson, J. R., Rao, P., Kumar, J., Chittori, S., Banerjee, S., Pierson, J., . . . Subramaniam, S. (2014). Self-assembled monolayers improve protein distribution on holey carbon cryo-EM supports. *Scientific Reports, 4*. doi:ARTN 7084

10.1038/srep07084

Miledi, R., Molinoff, P., & Potter, L. T. (1971). Biological Sciences: Isolation of the Cholinergic Receptor Protein of Torpedo Electric Tissue. *Nature, 229*(5286), 554-557. doi:10.1038/229554a0

Miller, P. S., & Aricescu, A. R. (2014). Crystal structure of a human GABAA receptor. *Nature, 512*(7514), 270-275. doi:10.1038/nature13293

Miyazawa, A., Fujiyoshi, Y., & Unwin, N. (2003). Structure and gating mechanism of the acetylcholine receptor pore. *Nature, 423*(6943), 949-955. doi:10.1038/nature01748

Mowrey, D., Cheng, M. H., Liu, L. T., Willenbring, D., Lu, X., Wymore, T., . . . Tang, P. (2013). Asymmetric ligand binding facilitates conformational transitions in

pentameric ligand-gated ion channels. *Journal of the American Chemical Society, 135*(6), 2172-2180. doi:10.1021/ja307275v

Navarro, P. P., Stahlberg, H., & Castano-Diez, D. (2018). Protocols for Subtomogram Averaging of Membrane Proteins in the Dynamo Software Package. *Front Mol Biosci, 5*, 82. doi:10.3389/fmolb.2018.00082

Neese, F. (2012). The ORCA program system. *WIREs Computational Molecular Science 2*, 73-78. doi:10.1002/wcms.81

Nemecz, A., Prevost, M. S., Menny, A., & Corringer, P. J. (2016). Emerging Molecular Mechanisms of Signal Transduction in Pentameric Ligand-Gated Ion Channels. *Neuron, 90*(3), 452-470. doi:10.1016/j.neuron.2016.03.032

Nicastro, D., Schwartz, C., Pierson, J., Gaudette, R., Porter, M. E., & McIntosh, J. R. (2006). The Molecular Architecture of Axonemes Revealed by Cryoelectron Tomography. *Science, 313*(5789), 944. doi:10.1126/science.1128618

Noble, A. J., Wei, H., Dandey, V. P., Zhang, Z., Potter, C. S., & Carragher, B. (2018). Reducing effects of particle adsorption to the air-water interface in cryoEM. *Nature Methods, 15*, 793-795.

Nogales, E., & Scheres, S. H. W. (2015). Cryo-EM: A Unique Tool for the Visualization of Macromolecular Complexity. *Molecular Cell, 58*(4), 677-689. doi:10.1016/j.molcel.2015.02.019

Nothdurfter, C., Tanasic, S., Di Benedetto, B., Rammes, G., Wagner, E.-M., Kirmeier, T., . . . Rupprecht, R. (2010). Impact of lipid raft integrity on 5-HT3 receptor function and its modulation by antidepressants. *Neuropsychopharmacology : official publication of the American College of Neuropsychopharmacology, 35*(7), 1510-1519. doi:10.1038/npp.2010.20

Nutt, D. J., & Malizia, A. L. (2018). New insights into the role of the GABAA–benzodiazepine receptor in psychiatric disorder. *British Journal of Psychiatry, 179*(5), 390-396. doi:10.1192/bjp.179.5.390

Olsen, R. W., & Sieghart, W. (2009). GABA A receptors: subtypes provide diversity of function and pharmacology. *Neuropharmacology, 56*(1), 141-148. doi:10.1016/j.neuropharm.2008.07.045

Orlova, E. V., & Saibil, H. R. (2011). Structural analysis of macromolecular assemblies by electron microscopy. *Chemical reviews, 111*(12), 7710-7748. doi:10.1021/cr100353t

Ortells, M. O., & Lunt, G. G. (1995). Evolutionary history of the ligand-gated ion-channel superfamily of receptors. *Trends in Neurosciences, 18*(3), 121-127. doi:https://doi.org/10.1016/0166-2236(95)93887-4

Palovcak, E., Wang, F., Zheng, S. Q., Yu, Z., Li, S., Betegon, M., . . . Cheng, Y. (2018). A simple and robust procedure for preparing graphene-oxide cryo-EM grids. *J Struct Biol, 204*(1), 80-84. doi:10.1016/j.jsb.2018.07.007

Paradiso, K., Zhang, J., & Steinbach, J. H. (2001). The C Terminus of the Human Nicotinic α4β2 Receptor Forms a Binding Site Required for Potentiation by an Estrogenic Steroid. *The Journal of Neuroscience, 21*(17), 6561. doi:10.1523/JNEUROSCI.21-17-06561.2001

Penczek, P. A., Zhu, J., Schröder, R., & Frank, J. (1997). THREE DIMENSIONAL RECONSTRUCTION WITH CONTRAST TRANSFER COMPENSATION FROM DEFOCUS SERIES *Single-Particle Cryo-Electron Microscopy* (Vol. Volume 10, pp. 232-239): World Scientific.

Peters, J. A., Kelley, S. P., Dunlop, J. I., Kirkness, E. F., Hales, T. G., & Lambert, J. J. (2004). The 5-hydroxytryptamine type 3 (5-HT3) receptor reveals a novel determinant of single-channel conductance. *Biochemical Society Transactions, 32*(Pt3), 547-552. doi:10.1042/BST0320547

Pettersen, E. F., Goddard, T. D., Huang, C. C., Couch, G. S., Greenblatt, D. M., Meng, E. C., & Ferrin, T. E. (2004). UCSF Chimera—A visualization system for exploratory research and analysis. *Journal of Computational Chemistry, 25*(13), 1605-1612. doi:10.1002/jcc.20084

Planck, M. (1949). The Meaning and Limits of Exact Science. *Science, 110*(2857), 319. doi:10.1126/science.110.2857.319

Polovinkin, L., Hassaine, G., Perot, J., Neumann, E., Jensen, A. A., Lefebvre, S. N., . . . Nury, H. (2018). Conformational transitions of the serotonin 5-HT3 receptor. *Nature, 563*(7730), 275-279. doi:10.1038/s41586-018-0672-3

Pronk, S., Pall, S., Schulz, R., Larsson, P., Bjelkmar, P., Apostolov, R., . . . Lindahl, E. (2013). GROMACS 4.5: a high-throughput and highly parallel open source molecular simulation toolkit. *Bioinformatics, 29*(7), 845-854. doi:10.1093/bioinformatics/btt055

Punjani, A., Rubinstein, J. L., Fleet, D. J., & Brubaker, M. A. (2017). cryoSPARC: algorithms for rapid unsupervised cryo-EM structure determination. *Nature Methods, 14*(3), 290-296. doi:10.1038/Nmeth.4169

Ramírez-Aportela, E., Vilas, J. L., Glukhova, A., Melero, R., Conesa, P., Martínez, M., . . . Sorzano, C. O. S. (2019). Automatic local resolution-based sharpening of cryo-EM maps. *Bioinformatics, 36*(3), 765-772. doi:10.1093/bioinformatics/btz671

Ramlaul, K., Palmer, C. M., & Aylett, C. H. S. (2020). Mitigating Local Over-fitting During Single Particle Reconstruction with SIDESPLITTER. *bioRxiv*, 2019.2012.2012.874081. doi:10.1101/2019.12.12.874081

Rayes, D., De Rosa, M. J., Sine, S. M., & Bouzat, C. (2009). Number and Locations of Agonist Binding Sites Required to Activate Homomeric Cys-Loop Receptors. *Journal of Neuroscience Research, 29*(18), 6022-6032. doi:10.1523/JNEUROSCI.0627-09.2009

Rea, A. C., Vandenberg, L. N., Ball, R. E., Snouffer, A. A., Hudson, A. G., Zhu, Y., . . . Dore, T. M. (2013). Light-Activated Serotonin for Exploring Its Action in Biological

Systems. *Chemistry & Biology, 20*(12), 1536-1546. doi:10.1016/j.chembiol.2013.11.005

Rigort, A., & Plitzko, J. M. (2015). Cryo-focused-ion-beam applications in structural biology. *Archives of Biochemistry and Biophysics, 581*, 122-130. doi:https://doi.org/10.1016/j.abb.2015.02.009

Rohou, A., & Grigorieff, N. (2015). CTFFIND4: Fast and accurate defocus estimation from electron micrographs. *Journal of Structural Biology, 192*(2), 216-221. doi:10.1016/j.jsb.2015.08.008

Ruan, Y., Kao, K., Lefebvre, S., Marchesi, A., Corringer, P.-J., Hite, R. K., & Scheuring, S. (2018). Structural titration of receptor ion channel GLIC gating by HS-AFM. *Proceedings of the National Academy of Sciences of the United States of America, 115*(41), 10333-10338. doi:10.1073/pnas.1805621115

Ruska, E. (1987). The development of the electron microscope and of electron microscopy. *Bioscience Reports, 7*(8), 607-629. doi:10.1007/BF01127674

Ryan, S. E., Demers, C. N., Chew, J. P., & Baenziger, J. E. (1996). Structural effects of neutral and anionic lipids on the nicotinic acetylcholine receptor: an Infrared difference spectroscopy study. *Journal of Biological Chemistry, 271*(40), 24590-24597.

Sanchez, R., Zhang, Y., Chen, W., Dietrich, L., & Kudryashev, M. (2020). Subnanometer-resolution structure determination in situ by a hybrid subtomogram averaging - single particle cryoEM - workflow. *bioRxiv*, 2020.2004.2024.057299. doi:10.1101/2020.04.24.057299

Scheres, S. H. (2012). RELION: implementation of a Bayesian approach to cryo-EM structure determination. *Journal of Structural Biology, 180*(3), 519-530. doi:10.1016/j.jsb.2012.09.006

Scheres, S. H. W. (2012). RELION: Implementation of a Bayesian approach to cryo-EM structure determination. *Journal of Structural Biology, 180*(3), 519-530. doi:10.1016/j.jsb.2012.09.006

Scheres, S. H. W., & Chen, S. (2012). Prevention of overfitting in cryo-EM structure determination. *Nature Methods, 9*(9), 853-854. doi:10.1038/nmeth.2115

Schindler, H., & Seelig, J. (1975). Deuterium order parameters in relation to thermodynamic properties of a phospholipid bilayer. Statistical mechanical interpretation. *Biochemistry, 14*(11), 2283-2287. doi:10.1021/bi00682a001

Schmidli, C., Albiez, S., Rima, L., Righetto, R., Mohammed, I., Oliva, P., . . . Braun, T. (2019). Microfluidic protein isolation and sample preparation for high-resolution cryo-EM. *Proceedings of the National Academy of Sciences, 116*(30), 15007. doi:10.1073/pnas.1907214116

Schreiter, C., Hovius, R., Costioli, M., Pick, H., Kellenberger, S., Schild, L., & Vogel, H. (2003). Characterization of the Ligand-binding Site of the Serotonin 5-HT3

Receptor. *The Journal of Biological Chemistry, 278*, 22709-22716. doi:10.1074/jbc.M301801200

Shivakumar, D., Williams, J., Wu, Y., Damm, W., Shelley, J., & Sherman, W. (2010). Prediction of absolute solvation free energies using molecular dynamics free energy perturbation and the OPLS force field. *Journal of Chemical Theory and Computation, 6*(5), 1509-1519. doi:10.1021/ct900587b

Sigel, E., & Steinmann, M. E. (2012). Structure, function, and modulation of GABA(A) receptors. *The Journal of biological chemistry, 287*(48), 40224-40231. doi:10.1074/jbc.R112.386664

Sindelar, C. V., & Grigorieff, N. (2011). An adaptation of the Wiener filter suitable for analyzing images of isolated single particles. *Journal of Structural Biology, 176*(1), 60-74. doi:10.1016/j.jsb.2011.06.010

Smart, O. S., Neduvelil, J. G., Wang, X., Wallace, B. A., & Sansom, M. S. (1996). HOLE: a program for the analysis of the pore dimensions of ion channel structural models. *Journal of Molecular Graphics, 14*(6), 354-360, 376.

Solt, K., Ruesch, D., Forman, S. A., Davies, P. A., & Raines, D. E. (2007). Differential effects of serotonin and dopamine on human 5-HT3A receptor kinetics: Interpretation within an allosteric kinetic model. *Journal of Neuroscience, 27*(48), 13151-13160. doi:10.1523/Jneurosci.3772-07.2007

Søndergaard, C. R., Olsson, M. H. M., Rostkowski, M., & Jensen, J. H. (2011). Improved treatment of ligands and coupling effects in empirical calculation and rationalization of pKa values. *Journal of Chemical Theory and Computation, 7*(7), 2284-2295. doi:10.1021/ct200133y

Song, K., Shang, Z., Fu, X., Lou, X., Grigorieff, N., & Nicastro, D. (2019). In situ structure determination at nanometer resolution using TYGRESS. *Nature Methods*. doi:10.1038/s41592-019-0651-0

Sorzano, C. O. S., Marabini, R., Velázquez-Muriel, J., Bilbao-Castro, J. R., Scheres, S. H. W., Carazo, J. M., & Pascual-Montano, A. (2004). XMIPP: a new generation of an open-source image processing package for electron microscopy. *Journal of Structural Biology, 148*(2), 194-204. doi:https://doi.org/10.1016/j.jsb.2004.06.006

Suloway, C., Pulokas, J., Fellmann, D., Cheng, A., Guerra, F., Quispe, J., . . . Carragher, B. (2005). Automated molecular microscopy: The new Leginon system. *Journal of Structural Biology, 151*(1), 41-60. doi:https://doi.org/10.1016/j.jsb.2005.03.010

Sunshine, C., & McNamee, M. G. (1994). Lipid modulation of nicotinic acetylcholine receptor function: the role of membrane lipid composition and fluidity. *Biochimica et Biophysica Acta (BBA) - Biomembranes, 1191*(1), 59-64. doi:10.1016/0005-2736(94)90233-X

Taly, A., Hénin, J., Changeux, J.-P., & Cecchini, M. (2014). Allosteric regulation of pentameric ligand-gated ion channels: an emerging mechanistic perspective. *Channels (Austin, Tex.), 8*(4), 350-360. doi:10.4161/chan.29444

Tan, Y. Z., Baldwin, P. R., Davis, J. H., Williamson, J. R., Potter, C. S., Carragher, B., & Lyumkis, D. (2017). Addressing preferred specimen orientation in single-particle cryo-EM through tilting. *Nature Methods, 14*(8), 793-796. doi:10.1038/Nmeth.4347

Tan, Y. Z., Cheng, A., Potter, C. S., & Carragher, B. (2016). Automated data collection in single particle electron microscopy. *Microscopy (Oxford, England), 65*(1), 43-56. doi:10.1093/jmicro/dfv369

Tegunov, D., & Cramer, P. (2019). Real-time cryo-electron microscopy data preprocessing with Warp. *Nature Methods, 16*(11), 1146-1152. doi:10.1038/s41592-019-0580-y

ThermoFisherScientific. The Krios Solution for Life Sciences. Retrieved from https://www.thermofisher.com/de/en/home/industrial/electron-microscopy/electron-microscopy-instruments-workflow-solutions/krios-solution.html

Thompson, A. J., & Lummis, S. C. R. (2013). A single channel mutation alters agonist efficacy at 5-HT3A and 5-HT3AB receptors. *British Journal of Pharmacology, 170*(2), 391-402. doi:10.1111/bph.12287

Tian, W., Chen, C., Lei, X., Zhao, J., & Liang, J. (2018). CASTp 3.0: computed atlas of surface topography of proteins. *Nucleic Acids Research, 46*(W1), W363-W367. doi:10.1093/nar/gky473

Tivol, W. F., Briegel, A., & Jensen, G. J. (2008). An improved cryogen for plunge freezing. *Microscopy and microanalysis : the official journal of Microscopy Society of America, Microbeam Analysis Society, Microscopical Society of Canada, 14*(5), 375-379. doi:10.1017/S1431927608080781

Tol, M. B., Deluz, C., Hassaine, G., Graff, A., Stahlberg, H., & Vogel, H. (2013). Thermal unfolding of a mammalian pentameric ligand-gated ion channel proceeds at consecutive, distinct steps. *Journal of Biological Chemistry, 288*, 5756-5769. doi:doi: 10.1074/jbc.M112.422287

Tovar, K. R., & Westbrook, G. L. (2012). Chapter 31 - Ligand-Gated Ion Channels. In N. Sperelakis (Ed.), *Cell Physiology Source Book (Fourth Edition)* (pp. 549-562). San Diego: Academic Press.

Triebl, A., Trötzmüller, M., Hartler, J., Stojakovic, T., & Köfeler, H. C. (2017). Lipidomics by ultrahigh performance liquid chromatography-high resolution mass spectrometry and its application to complex biological samples. *J Chromatogr B Analyt Technol Biomed Life Sci, 1053*, 72-80. doi:10.1016/j.jchromb.2017.03.027

Unwin, N. (2005). Refined Structure of the Nicotinic Acetylcholine Receptor at 4Å Resolution. *Journal of Molecular Biology, 346*(4), 967-989. doi:10.1016/j.jmb.2004.12.031

Unwin, N., & Fujiyoshi, Y. (2012). Gating Movement of Acetylcholine Receptor Caught by Plunge-Freezing. *Journal of Molecular Biology, 422*(5), 617-634. doi:10.1016/j.jmb.2012.07.010

Vafabakhsh, R., Levitz, J., & Isacoff, E. Y. (2015). Conformational dynamics of a class C G-protein-coupled receptor. *Nature, 524*(7566), 497-+. doi:10.1038/nature14679

van Heel, M., Harauz, G., Orlova, E. V., Schmidt, R., & Schatz, M. (1996). A New Generation of the IMAGIC Image Processing System. *Journal of Structural Biology, 116*(1), 17-24. doi:https://doi.org/10.1006/jsbi.1996.0004

Vanommeslaeghe, K., Raman, E. P., & MacKerell, A. D. (2012). Automation of the CHARMM general force field (CGenFF) II: assignment of bonded parameters and partial atomic charges. *Journal of Chemical Information and Modeling, 52*(12), 3155-3168. doi:10.1021/ci3003649

Venkatachalan, S. P., & Czajkowski, C. (2012). Structural link between γ-aminobutyric acid type A (GABAA) receptor agonist binding site and inner β-sheet governs channel activation and allosteric drug modulation. *The Journal of biological chemistry, 287*(9), 6714-6724. doi:10.1074/jbc.M111.316836

Vilas, J. L., Gómez-Blanco, J., Conesa, P., Melero, R., Miguel de la Rosa-Trevín, J., Otón, J., . . . Sorzano, C. O. S. (2018). MonoRes: Automatic and Accurate Estimation of Local Resolution for Electron Microscopy Maps. *Structure, 26*(2), 337-344.e334. doi:https://doi.org/10.1016/j.str.2017.12.018

Vinothkumar, K. R., & Henderson, R. (2016). Single particle electron cryomicroscopy: trends, issues and future perspective. *Quarterly Reviews of Biophysics, 49*, e13. doi:10.1017/S0033583516000068

von Appen, A., Kosinski, J., Sparks, L., Ori, A., DiGuilio, A. L., Vollmer, B., . . . Beck, M. (2015). In situ structural analysis of the human nuclear pore complex. *Nature, 526*(7571), 140-+. doi:10.1038/nature15381

von Loeffelholz, O., Natchiar, S. K., Djabeur, N., Myasnikov, A. G., Kratzat, H., Ménétret, J.-F., . . . Klaholz, B. P. (2017). Focused classification and refinement in high-resolution cryo-EM structural analysis of ribosome complexes. *Current Opinion in Structural Biology, 46*, 140-148. doi:https://doi.org/10.1016/j.sbi.2017.07.007

Wagner, T., Merino, F., Stabrin, M., Moriya, T., Antoni, C., Apelbaum, A., . . . Raunser, S. (2019). SPHIRE-crYOLO is a fast and accurate fully automated particle picker for cryo-EM. *Communications biology, 2*, 218-230. doi:10.1038/s42003-019-0437-z

Wan, W., Kolesnikova, L., Clarke, M., Koehler, A., Noda, T., Becker, S., & Briggs, J. A. G. (2017). Structure and assembly of the Ebola virus nucleocapsid. *Nature, 551*(7680), 394-397. doi:10.1038/nature24490

Wang, F., Liu, Y., Yu, Z., Li, S., Cheng, Y., & Agard, D. (2019). *General and robust covalently linked graphene oxide affinity grids for high-resolution cryo-EM*.

Williams, D. B., & Carter, C. B. (2009a). Elastic Scattering. In D. B. Williams & C. B. Carter (Eds.), *Transmission Electron Microscopy: A Textbook for Materials Science* (pp. 39-51). Boston, MA: Springer US.

Williams, D. B., & Carter, C. B. (2009b). How to 'See' Electrons. In D. B. Williams & C. B. Carter (Eds.), *Transmission Electron Microscopy: A Textbook for Materials Science* (pp. 115-126). Boston, MA: Springer US.

Williams, D. B., & Carter, C. B. (2009c). Lenses, Apertures, and Resolution. In D. B. Williams & C. B. Carter (Eds.), *Transmission Electron Microscopy: A Textbook for Materials Science* (pp. 91-114). Boston, MA: Springer US.

Williams, D. B., & Carter, C. B. (2009d). The Transmission Electron Microscope. In D. B. Williams & C. B. Carter (Eds.), *Transmission Electron Microscopy: A Textbook for Materials Science* (pp. 3-22). Boston, MA: Springer US.

Williams, D. B., & Carter, C. B. (2009e). X-ray Spectrometry. In D. B. Williams & C. B. Carter (Eds.), *Transmission Electron Microscopy: A Textbook for Materials Science* (pp. 581-603). Boston, MA: Springer US.

Wirth, A., Holst, K., & Ponimaskin, E. (2017). How serotonin receptors regulate morphogenic signalling in neurons. *Prog Neurobiol., 151*, 35-56. doi:10.1016/j.pneurobio.2016.03.007

Wu, C., Huang, X., Cheng, J., Zhu, D., & Zhang, X. (2019). High-quality, high-throughput cryo-electron microscopy data collection via beam tilt and astigmatism-free beam-image shift. *Journal of Structural Biology, 208*(3), 107396. doi:https://doi.org/10.1016/j.jsb.2019.09.013

Wu, Z. S., Cheng, H., Jiang, Y., Melcher, K., & Xu, H. E. (2015). Ion channels gated by acetylcholine and serotonin: structures, biology, and drug discovery. *Acta Pharmacol Sin, 36*(8), 895-907. doi:10.1038/aps.2015.66

Xiong, Q. R., Morphew, M. K., Schwartz, C. L., Hoenger, A. H., & Mastronarde, D. N. (2009). CTF determination and correction for low dose tomographic tilt series. *Journal of Structural Biology, 168*(3), 378-387. doi:10.1016/j.jsb.2009.08.016

Yan, D., Schulte, M. K., Bloom, K. E., & White, M. M. (1999). Structural features of the ligand-binding domain of the serotonin 5HT3 receptor. *Journal of Biological Chemistry, 274*, 5537-5541. doi:10.1074/jbc.274.9.5537

Yeagle, P. L. (1985). Cholesterol and the cell membrane. *Biochimica et Biophysica Acta (BBA) - Biomembranes, 822*(3), 267-287. doi:10.1016/0304-4157(85)90011-5

Zarkadas, E., Zhang, H., Cai, W., Effantin, G., Perot, J., Neyton, J., . . . Nury, H. (2020). The binding of palonosetron and other antiemetic drugs to the serotonin 5-HT3 receptor. *bioRxiv*, 2020.2002.2014.947937. doi:10.1101/2020.02.14.947937

Zhang, C., Cantara, W., Jeon, Y., Musier-Forsyth, K., Grigorieff, N., & Lyumkis, D. (2019). Analysis of discrete local variability and structural covariance in macromolecular assemblies using Cryo-EM and focused classification. *Ultramicroscopy, 203*, 170-180. doi:10.1016/j.ultramic.2018.11.016

Zhang, K. (2016). Gctf: Real-time CTF determination and correction. *Journal of Structural Biology, 193*(1), 1-12. doi:10.1016/j.jsb.2015.11.003

Zhang, K. (2017). Gautomatch.

Zhang, X., Yan, C., Zhan, X., Li, L., Lei, J., & Shi, Y. (2018). Structure of the human activated spliceosome in three conformational states. *Cell Research, 28*(3), 307-322. doi:10.1038/cr.2018.14

Zhao, J., Brubaker, M. A., Benlekbir, S., & Rubinstein, J. L. (2015). Description and comparison of algorithms for correcting anisotropic magnification in cryo-EM images. *J Struct Biol, 192*(2), 209-215. doi:10.1016/j.jsb.2015.06.014

Zheng, S. Q., Palovcak, E., Armache, J. P., Verba, K. A., Cheng, Y., & Agard, D. A. (2017). MotionCor2: anisotropic correction of beam-induced motion for improved cryo-electron microscopy. *Nature Methods, 14*(4), 331-332. doi:10.1038/nmeth.4193

Zhu, S., Noviello, C. M., Teng, J., Walsh, R. M., Kim, J. J., & Hibbs, R. E. (2018). Structure of a human synaptic GABAA receptor. *Nature, 559*(7712), 67-72. doi:10.1038/s41586-018-0255-3

Zivanov, J., Nakane, T., Forsberg, B. O., Kimanius, D., Hagen, W. J. H., Lindahl, E., & Scheres, S. H. W. (2018). New tools for automated high-resolution cryo-EM structure determination in RELION-3. *eLife, 7*, e42166. doi:10.7554/eLife.42166

Zivanov, J., Nakane, T., & Scheres, S. H. W. (2019). A Bayesian approach to beam-induced motion correction in cryo-EM single-particle analysis. *IUCrJ, 6*(Pt 1), 5-17. doi:10.1107/S205225251801463X

Declaration of scientific collaborations

Except where stated otherwise by reference or acknowledgment, the work presented was generated by myself under the supervision of my advisors during my doctoral studies. All contributions from colleagues are explicitly referenced in the thesis. The material listed below was obtained in the context of collaborative search.

Figure 3.1 Cell culture was done by Luise Eckhardt-Strelau at Max-Planck-Institute of Biophysics. Protein purification and optimization, NanoDSF and MST measurements were performed by Dr. Patricia M. Dijkman at Max-Planck-Institute of Biophysics, current address at Institute of Neuropathology, University Medical Center Göttingen, Göttingen, Germany; Cluster of Excellence "Multiscale Bioimaging: from Molecular Machines to Networks of Excitable Cells" (MBExC), University of Göttingen, Göttingen, Germany.

Figure 3.10, 3.11, 3.12, 3.22 MD simulations and related binding energy calculations, lipid order calculations, potential energy calculations were performed by Dr. Shuguang Yuan and Dr. Rongfeng Zou at Research Center for Computer-Aided Drug Discovery, Shenzhen Institutes of Advanced Technology, Chinese Academy of Sciences, Shenzhen, China.

Table 3.5 Lipidomics were performed by Dr. Martina Zandl-Lang at Department of Pediatrics and Adolescent Medicine, Division of General Pediatrics, Medical University of Graz, Graz, Austria; and Dr. Harald Köfele at Core Facility Mass Spectrometry, ZMF, Medical University of Graz, Graz, Austria. Results were analyzed and summarized by Dr. Patricia M. Dijkman.

Figure 3.27 One hybrid TMV dataset was collected by Lea Dietrich at Max-Planck-Institute of Biophysics.

Whenever a figure, table or text is identical to a previous publication, it is stated explicitly in the thesis that copyright permission and/or co-author agreement has been obtained.

Acknowledgements

In this chapter, I finally have this great opportunity to express my gratitude to everyone that gave me so many supports when I had difficulties during my PhD study and stay in Germany. They are my supervisors, mentors, collaborators, group members, colleagues, my close friends, also my families.

First of all, I would like to thank Dr. Misha Kudryashev, my PhD supervisor at the Max Planck Institute of Biophysics, for offering me the great chance to work in his lab and our department, which is well-known as one of the front-edge institutes for structural biology cryo-electron microscopy researches. And I thank for his guiding on my learning, especially for tomography and sub-tomogram averaging. I am also very lucky to be his first PhD student and it was a valuable experience to become better-qualified of my knowledge with also seeing the growth of our lab. He was a good mentor and allowed open discussion for my projects which encouraged me to be more critical thinking in my further work and career.

Jun. Prof. Dr. Inga Hänelt, my PhD supervisor at the Department of Biochemistry, Goethe University. I really appreciate that she would accept me as her PhD student. Although the real time that we've been working closely in lab was not much, but thanks so much for her being there and always would be my support during my study.

I also would like to write down my great thanks to Prof. Dr. Werner Kühlbrandt for giving me critical suggestions when I felt lost in my project, and great thanks to his encouraging and important suggestions at every progress discussion for my work. It was my lucky and great honor to be able to receive his advices.

Dr. Patricia M. Dijkman, our first group member as postdoctoral researcher, my colleague and close friend. I really appreciate all her uncountable helps during my study. Thanks so much for all her inspiration and encouraging. It was really lucky that I could work with her in our lab and learnt how to be more responsible and critical when doing research. I always feel I owed her "very expensive things", that was the time she spent on helping me with very detailed instructions and discussions. Thanks for her being my "third mentor" and being my friend.

Prof. Dr. Horst Vogel, he was the "initiator" for this project. He contributed a lot on the direction of this project, gave critical suggestions on what to try and what do not. He also put significant time on discussion with us about the results in this

project and provided important advices. Here, I would like to thank his great contributions and helps. I also received great supports from one of Horst's group members, Dr. Catarina Alves. She provided the micro-vesicle specimen in this project. Thanks so much for her contribution and supports.

Dr. Shuguang Yuan and his lab, my collaborators. I would like to thank for their contribution on performing the MD simulations and all the critical discussions we had. It was really inspiring.

Ricardo Sanchez, my officemate and friend. Thanks so much for his patience when I came to him with questions which were not really difficult for him. He helped me a lot, not only for the discussions about image/data processing, but also my confusing in work. It was grateful to work with him and thanks so much for his kind helps and encouraging all the time.

I would like to express my great thank to Luise Eckhardt-Strelau, our group member, for her work on cell culturing in this project and her great helps on supporting our lab work. She was very responsible and kind.

I would also like to thank Dr. Martina Zandl-Lang and Dr. Harald Köfeler for their work on performing lipidomics in this project.

I also would like to express my great thank to Lea Dietrich for our discussions about SerialEM automation and for her assistance in testing the performance of SerialEM after installation, and collecting one of the test TMV dataset.

Apart from the direct helps I received for this project, I would also like to address many indirect supports that I gained from my colleagues, such as the access of the EM facility, IT and computing services, technical discussions and demonstrations. I apologize if I forgot to mention anyone who had spent time on helping me.

I would like to give my great thanks to Deryck Mills and our EM staffs, Dr. Susann Kaltwasser, Simone Prinz, Mark Linder, and Sonja Welsch at Max Planck Institute of Biophysics, for their expert technical assistance and daily supports. Also, many thanks to Prof. Dr. Achilleas Frangakis, and his lab staffs at BMLS cryo-electron microscopy facility for providing the access and technical assistance on the usage of microscopes.

Great thanks to Dr. Özkan Yildiz and Dr. Juan-Francisco Castillo-Hernandez for their kind computing supports.

I would like to thank Dr. Arne Möller for his critical suggestions and advice during the progress of the project. They were great helpful.

Great thanks to Dr. Dovile Januliene for the detailed technique discussions. I've learnt so much from her as well.

I would like to thank Dr. Janet Vonck for her kind introducing of the IMPRES program, from that I got supported for 2 years during my PhD. And I really appreciate for her encouragement and her detailed demonstrations on my technique questions. She was so kind and she also gave advices for my project.

I would like to express my thanks to Dr. Kendra Leigh for the daily discussions in our office during my PhD study about, not only my projects, but also more experimental and technical scientific questions, and to her critical advices and kind suggestions on writing of this thesis.

And I would also like to express my great thanks to Dr. Thomas Niezold for his kind helps with translation to German of the summary in this thesis.

I would also like to thank Nikita Balyschew for the discussion about data on-fly processing with FOCUS.

Also, I really appreciate all the kindest helps from Monika Hobrack during my entire stay and study in Germany.

For all our group members, colleagues and Alumni, whose name hasn't been mentioned above, Dr. Irina Prokhorova, Wenbo Chen, Scott Chang, Dr. Eva Cunha, Dr. Ashish Gadicherla, Ariane Sahebzade, Simon Wiessing, Wolfram Davila, Daniel Schröder, and Robert Gebauer, with whom I had the pleasure to work during my doctorate and that contributed to the success of these projects.

And I would like to thank Prof. Dr. Yifan Cheng and his group members. I was extremely lucky to had the opportunity to work in his lab as a visitor, and I was really encouraged and inspired at that time and decided to pursue my PhD degree and to develop my knowledge and skills in this field. He was a great group leader and it was my honor to learn from him and his lab.

In the very last but not least, I appreciate deeply for the supports by my parents.

向一直默默理解和陪伴我的父亲母亲，张廷林先生和赵桂玲女士，表达我内心深切的爱与感谢。

Acknowledgements

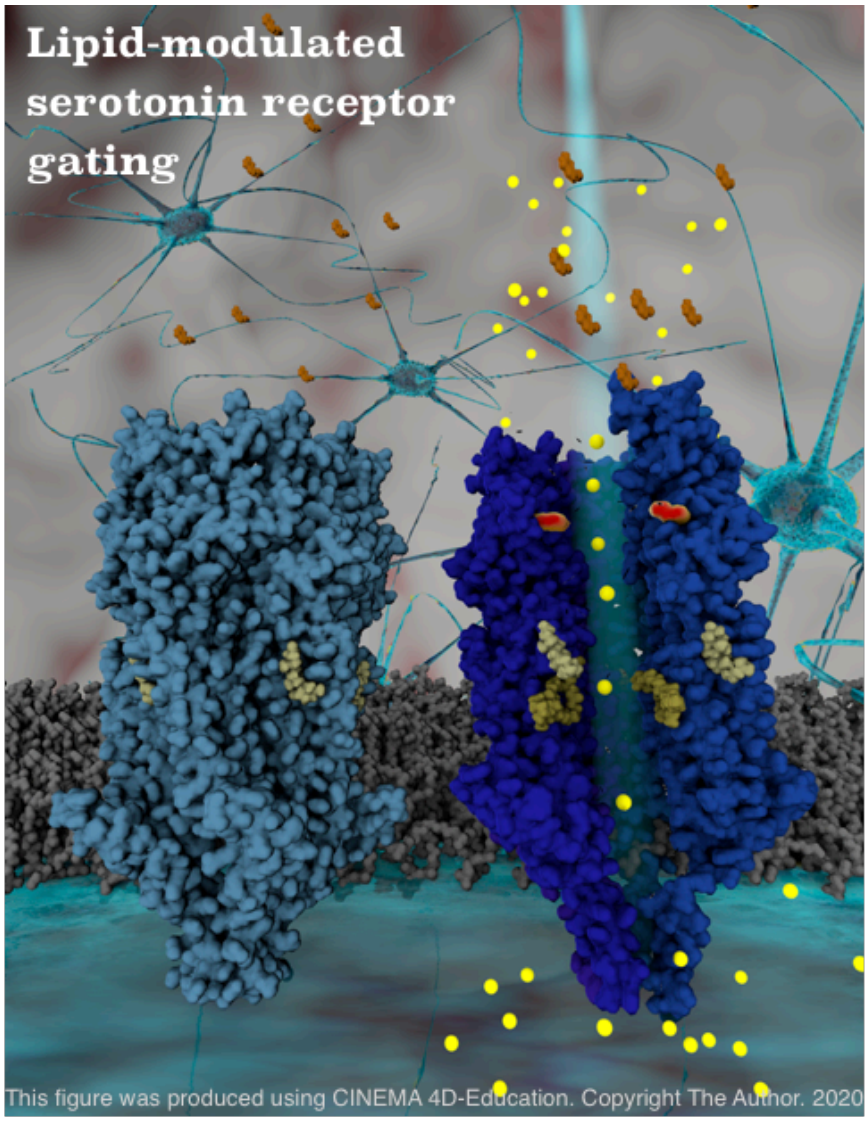
Lipid-modulated
serotonin receptor
gating
This figure was produced using CINEMA 4D-Education. Copyright The Author. 2020